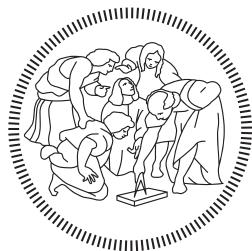


POLITECNICO DI MILANO
Facoltà di Ingegneria
Scuola di Ingegneria Industriale e dell'Informazione
Dipartimento di Elettronica, Informazione e Bioingegneria
Master of Science in Electronics Engineering



Design and Implementation of a Driver for In-Wheel Brushless Motors for Unmanned Vehicles

Supervisor:

PROF. GIAMBATTISTA GRUOSO

Co-Supervisor:

PROF. LUCA BASCETTA

Master Graduation Thesis by:

ARTURO MONTÚFAR ARREOLA
Student Id n. 840541

Academic Year 2016-2017

COLOPHON

This document was typeset using the typographical look-and-feel `classicthesis` developed by André Miede. The style was inspired by Robert Bringhurst's seminal book on typography "*The Elements of Typographic Style*". `classicthesis` is available for both L^AT_EX and LyX:

<http://code.google.com/p/classicthesis/>

The template has been adapted by Emanuele Mason, Andrea Cominola and Daniela Anghileri: *A template for master thesis at DEIB*, June 2015

Final Version as of December 2, 2017 (classicthesis).

To my family and friends:
Thanks for supporting me while I'm learning to fly
— Arturo

ACKNOWLEDGMENTS

I want to thank the following people for helping me with the development of this work:

To Professor Giambattista Gruosso, for giving me the opportunity to develop such an interesting thesis project and for his guidance through the research method for this kind of projects, which is as valuable as the knowledge I gained regarding the topic developed in this work.

To Professor Luca Bascetta, for giving me advice and material regarding the research and implementation of the motor control theory and the work already developed regarding this project.

To Professor Federico Terraneo, for his support and interest on the implementation of Miosix in this project, and to the Skyward Experimental Rocketry team, for their help with the CAN bus driver.

To Marco Bauer, for his support in the aspects related to the mechanics of the project and also for providing me with information of the work already developed.

To Professor Luigi Piegari, for his support and advice on the final tests.

To Giulio Fontana, for his support and advice regarding the manufacture of the systems developed for this work while working in the AIRLab.

To Professor Luigi Colombo for providing me documentation regarding the thermal management proposal developed in this work.

To Stefano Bianchi for helping with the fine details of the tuning of the controllers and with the development of the tests.

To Milica Jovanovic for helping me with the documentation of the software architecture and with the flowcharts.

CONTENTS

Abstract	xv
Estratto	xvii
Preface	xix
1 INTRODUCTION	1
2 PROBLEM STATEMENT	5
2.1 Technological Trade-Offs	5
2.2 Learning Curve	6
2.3 Motor Driver Development	6
2.4 Implementation of Field Oriented Control	6
3 MOTOR CONTROL THEORY	9
3.1 Electric Motor	9
3.1.1 Physical Principles	9
3.2 PMAC Motors	17
3.2.1 BLDC Motors	19
3.2.2 PMSM Motors	19
3.3 Electric Drives	20
3.3.1 Inverter	20
3.3.2 Angular Position Sensors	23
3.3.3 Current Sensors	25
3.3.4 Controller	26
3.4 PMAC Motors Driving Methods	27
3.4.1 Trapezoidal Drive	27
3.4.2 Sinusoidal Drive	32
3.5 Electric Motor Control Methods	33
3.5.1 Speed Control	34
3.5.2 Torque Control	35
3.5.3 Field Oriented Control	35
3.5.4 Speed Control with Field Oriented Control	37
4 STUDY CASE	39
4.1 Robi	39
4.2 In-Wheel Motors	40
4.3 Power Architecture	41
4.4 Electronic Architecture	41
5 PROJECT DEVELOPMENT	43
5.1 Hardware	43
5.1.1 VESC Board	43
5.1.2 Power Supply Input	44
5.1.3 Power MOSFET Three-Phase Inverter	48
5.1.4 MOSFET Driver	49
5.1.5 Microcontroller Unit	54
5.1.6 Peripherals	55
5.1.7 Angular Position Sensor	57

5.2	Embedded Software	60
5.2.1	Operating System	61
5.2.2	Pulse Width Modulated Signal Generation	62
5.2.3	Analog to Digital Converter	64
5.2.4	Algorithms Implementation	66
5.2.5	Proportional-Integral Controller	68
5.3	Test Setup	74
5.3.1	Measurement Board	74
5.3.2	User Interface	75
5.3.3	ROBI' Setup	75
6	RESULTS	79
6.1	Trapezoidal Drive – Open Loop	79
6.2	Speed Control with Trapezoidal Drive	87
6.3	Sinusoidal Drive – Open Loop	91
6.4	Field Oriented Control	93
6.5	Speed Control with Field Oriented Control	95
7	CONCLUSION	101
7.1	Changes Proposal	101
7.2	Future Work	102
	BIBLIOGRAPHY	103
A	APPENDIX A: VESC BOARD SCHEMATIC FILES	105
B	APPENDIX B: DRV8302 FUNCTION BLOCK DIAGRAM	113
C	APPENDIX C: MOTOR SIGNALS MEASUREMENT BOARD SCHEMATICS	115

LIST OF FIGURES

Figure 1.1	Jedlik's "Electromagnetic Self-Rotor"	1
Figure 1.2	Rimac Concept S	3
Figure 3.1	Partially Assembled Motor	10
Figure 3.2	Lorentz's Law Diagram	11
Figure 3.3	Visual explanation of the alignment principle	13
Figure 3.4	DC Motor Scheme	14
Figure 3.5	DC Motor Electrical Model	15
Figure 3.6	Torque-Speed Curve	16
Figure 3.7	Brushless Motor Transverse Section	17
Figure 3.8	Different pole pair configurations	18
Figure 3.9	Electric Drive Scheme	20
Figure 3.10	Simple Three-Phase Inverter	21
Figure 3.11	Three-Phase Inverter	22
Figure 3.12	High-Side and Low-Side Driving Scheme	22
Figure 3.13	MOSFET Driving Diagram	23
Figure 3.14	Hall Effect Sensor	24
Figure 3.15	Sensorless Angular Detection	25
Figure 3.16	Shunt Resistance Current Detection	26
Figure 3.17	Trapezoidal BEMF	28
Figure 3.18	Six Step Commutation Currents	30
Figure 3.19	Six Step Commutation	31
Figure 3.20	PWM Signal	32
Figure 3.21	Sinusoidal BEMF	33
Figure 3.22	Electromechanical Dynamics Coupling	34
Figure 3.23	PI Controller	34
Figure 3.24	Speed Controller with Trapezoidal Drive	34
Figure 3.25	Torque Controller with Trapezoidal Drive	35
Figure 3.26	Field Oriented Control Blocks Diagram	36
Figure 3.27	Field Oriented Control applied in Speed Control	37
Figure 4.1	ROBI' Basic Configuration	39
Figure 4.2	Encoder Transmission Configuration	41
Figure 4.3	ECUs architecture	42
Figure 5.1	VESC Front Side	44
Figure 5.2	VESC Back Side	45
Figure 5.3	DRV8302 Simplified Schematic	50
Figure 5.4	Gate Charge vs. Gate-to-Source Voltage	52
Figure 5.5	Current Shunt Amplifier Simplified Block Diagram	55
Figure 5.6	RS422 Transceiver Diagram	58
Figure 5.7	New angular position transmission system	59

Figure 5.8	Embedded Software Architecture Diagram	61
Figure 5.9	Threads Execution Flowchart	61
Figure 5.10	Edge-aligned PWM waveforms	63
Figure 5.11	Center-aligned PWM waveforms	63
Figure 5.12	Complementary output with dead-time insertion	64
Figure 5.13	Current reading in shunt resistor	65
Figure 5.14	ADC and PWM Synchronization	65
Figure 5.15	Trapezoidal drive with complementary PWM	69
Figure 5.16	Speed Calculation Flowchart	70
Figure 5.17	Trapezoidal Drive Flowchart	71
Figure 5.18	Field Oriented Control Flowchart	72
Figure 5.19	Trapezoidal drive implemented on in-wheel motor mounted on ROBI'	73
Figure 5.20	WMU connected to measurement board	76
Figure 5.21	In-wheel motor attached to Marelli DC generator	77
Figure 6.1	Angular Speed vs Duty Cycle at Different Loads	80
Figure 6.2	Trapezoidal drive voltage waveforms without load applied	81
Figure 6.3	Trapezoidal drive voltage waveforms with load = 1 Nm	82
Figure 6.4	Trapezoidal drive voltage waveforms with load = 3 Nm	83
Figure 6.5	Trapezoidal voltage waveforms drive Duty Cycle = 70% and load = 6 Nm	83
Figure 6.6	Trapezoidal drive current waveforms without load applied	84
Figure 6.7	Trapezoidal drive current waveforms with load = 1 Nm	85
Figure 6.8	Trapezoidal drive current waveforms with load = 3 Nm	86
Figure 6.9	trapc9	86
Figure 6.10	Step response to a 10 rad/s signal without load applied	87
Figure 6.11	Step response to a 40 rad/s signal without load applied	88
Figure 6.12	Step response to a 10 rad/s signal with a 3 Nm load	88
Figure 6.13	Step response to a 40 rad/s signal with a 3 Nm load	89
Figure 6.14	Step response to a 10 rad/s signal without load, compared to its driving duty cycle signal	89
Figure 6.15	Step response to a 20 rad/s signal with a 3 Nm load, compared to its driving duty cycle signal	90

Figure 6.16	Center-aligned PWM voltage waveform	91
Figure 6.17	Sinusoidal drive current waveforms without load applied	92
Figure 6.18	FOC with different loads	94
Figure 6.19	FOC speed control loop without load applied	96
Figure 6.20	FOC speed control loop with 1 Nm load	97
Figure 6.21	FOC speed control loop with 3 Nm load	98
Figure 6.22	plot8	99
Figure 6.23	plot9	99
Figure 6.24	FOC three-phase current waveform in a step response to a 10 rad/s signal with a load of 1 Nm	100
Figure A.1	Schematic Overview	106
Figure A.2	Three-Phase MOSFET Inverter	107
Figure A.3	In-Board Temperature Sensor	108
Figure A.4	CAN Bus Transceiver	109
Figure A.5	Hall Effect Sensors Signal Conditioning	110
Figure A.6	STM32F405 Hardware Setup	111
Figure A.7	DRV8302 MOSFET Driver	112
Figure B.1	DRV8302 Function Block Diagram	113
Figure C.1	Schematic Overview	116
Figure C.2	Embedded system attachment pinout	117
Figure C.3	Power management of the board	118
Figure C.4	Voltage and current signal conditioning circuits	119

LIST OF TABLES

Table 3.1	Six-Step commutating sequence	29
Table 4.1	HUB10GL in-wheel motor main characteristics	40
Table 4.2	Battery main characteristics	41
Table 5.1	VESC Board Operating Ranges	45
Table 5.2	American Wire Gauge current load ratings in function of the number of cores of the wire (The Engineering ToolBox, 2015)	47
Table 5.3	IRFS7530-7PPbF Absolute Maximum Rating	48
Table 5.4	IRFS7530-7PPbF Dynamic Electrical Characteristics	49

Table 5.5	Marelli DC current generator characteristics in function on its rotation speed	76
-----------	--	----

LISTINGS

Listing 5.1	Code snippet of the basic PI controller implemented for the project	68
-------------	---	----

ACRONYMS

OS	operating system
BEMF	Back Electromotive Force
PMAC	Permanent Magnet Alternating Current
PMSM	Permanent Magnet Synchronous Motor
BLDC	Brushless Direct Current
PCB	Printed Circuit Board
FOC	Field Oriented Control
DC	Direct Current
PP	Pole Pairs
PWM	Pulse Width Modulation
MOSFET	Metal–Oxide Semiconductor Field-Effect Transistor
IGBT	Insulated-Gate Bipolar Transistor
ADC	Analog-to-Digital Converter
PI	Proportional-Integral
SPI	Serial Peripheral Interface
SSI	Synchronous Serial Interface
ECU	Electronic Control Unit
CAN	Controller Area Network

WMU	Wheel Management Unit
BMU	Battery Management Unit
VMU	Vehicle Management Unit
AMU	Arm Management Unit
IC	Integrated Circuit
FPU	Floating Point Unit
DSP	Digital Signal Processor
IC	Integrated Circuit
ESC	Electronic Speed Controller
LDO	Low Drop-Out
TI	Texas Instruments
KCL	Kirchhoff's Current Law
UART	Universal Asynchronous Receiver-Transmitter
UI	User Interface
USB	Universal Serial Bus
I₂C	Inter-Integrated Circuits
NTC	Negative Temperature Coefficient
MSB	Most Significative Bit
ISR	Interrupt Service Routine
OS	Operating System

ABSTRACT

The purpose of this thesis is to study the architecture of a commercial brushless motor driving circuit proposed by Texas Instruments and implemented as an electronic speed board as an "open source" project available online, analysing the advantages and disadvantages of such design regarding the implementation of trapezoidal and sinusoidal motor driving and speed and current control techniques for an unmanned vehicle designed for robotic agriculture. After this, the implementation of such driving and control techniques was physically carried out and tested.

This thesis explains in details the most important parts regarding the physical implementation of a motor driving system in such a way that it can be fully replicated. Chapter 1 contains some initial information regarding the electric motor history and the motivation to realize this work. In Chapter 2, we explain more in detail the different reasons why this work was developed and the focus points that were stressed out. In Chapter 3, a simple but sufficient explanation about the theory behind the electric motor is given, explaining also the different existing technologies and their particular driving methods. In Chapter 4 we explain the study case of ROBI', a prototype mobile manipulator for agricultural applications, which uses the in-wheel motor for which the motor driver of this work was developed. In Chapter 5 we explain in deep detail all the work developed around the implementation of the motor driver, both in the software and the hardware fields. In Chapter 6 we explain the final results of the work, showing and comparing graphs and waveforms of the behaviour of the in-wheel motor driven by the system developed. Finally, on Chapter 7, we discuss the results of the work realized and propose a new system, based on the implementation of the researched architecture and the problems encountered while working on the project.

ESTRATTO

Lo scopo di questa tesi è quello di studiare l'architettura di un driver per motori brushless commerciale proposto da Texas Instruments e implementato come un circuito elettronico come un progetto "open source" disponibile online, analizzando i vantaggi e gli svantaggi di tale progetto per quanto riguarda l'implementazione di eccitazione a motore trapezoidale e sinusoidale e tecniche di controllo di velocità e corrente per un veicolo senza pilota progettato per l'agricoltura robotica. Successivamente, l'implementazione di tali tecniche di eccitazione e controllo è stata effettuata e testata fisicamente.

Questa tesi spiega in dettaglio le parti più importanti riguardanti l'implementazione fisica di un sistema di guida del motore in modo tale da poter essere completamente replicato. Il capitolo 1 contiene alcune informazioni iniziali sulla storia del motore elettrico e la motivazione per realizzare questo lavoro. Nel capitolo 2, spieghiamo più in dettaglio i diversi motivi per cui questo lavoro è stato sviluppato e gli aspetti principali che sono stati evidenziati. Nel capitolo 3 viene fornita una spiegazione semplice ma sufficiente sulla teoria alla base del motore elettrico, che spiega anche le diverse tecnologie esistenti e i loro particolari metodi di guida. Nel capitolo 4 spieghiamo il caso di studio di ROBI', un prototipo di manipolatore mobile per applicazioni agricole, che utilizza il motore a ruote motrici per il quale è stato sviluppato il driver motorio di questo lavoro. Nel capitolo 5 spieghiamo dettagliatamente tutto il lavoro sviluppato attorno all'implementazione del driver del motore, sia nel campo del software che in quello dell'hardware. Nel capitolo 6 spieghiamo i risultati finali del lavoro, mostrando e confrontando grafici e forme d'onda del comportamento del motore a ruote motrici guidato dal sistema sviluppato. Infine, nel capitolo 7, discutiamo i risultati del lavoro realizzato e proponiamo un nuovo sistema, basato sull'implementazione dell'architettura ricercata e sui problemi incontrati durante il lavoro sul progetto.

PREFACE

*Knowledge is only part of understanding.
Genuine understanding comes from hands-on experience.*

— Seymour Papert *Constructionism* 1991

Motor control is a topic that must be experienced personally to be understood. This is a characteristic of many other engineering topics: they need to be experienced by the engineer or by the student to be fully understood. All the theory behind the movement of the shaft of the electric motor, which explains all the different phenomena interacting to create mechanical motion from electrical energy, should be experienced to fully understand everything that is involved. This is the reason why the practical implementation of theoretical topics is always interesting. Practical implementation makes us realize that there are always challenges that might not be taken into account while they are being studied from books, and they represent new opportunities to drive research and development for improvement.

This text was written with the idea of becoming a guide on the development of a motor controller for further projects, including the explanation of the basic physical phenomena that acts on electric motors and the important parameters to consider for the prediction of its motion, to the implementation of the hardware and software of a driving circuit and a detailed explanation on the most important factors to bring a motor controller alive and to successfully drive a permanent magnet motor. Even if the development of the work was intended for a specific project, all the information related to the development of the motor control systems can be applied to different projects, which is why this work can be useful also as a reference for projects not related to the robotic agriculture.

— Arturo Montúfar Arreola

INTRODUCTION

Electrical science, too, by its fascination, by its promises of immense realizations, of wonderful possibilities chiefly in humanitarian respects, has attracted the attention and enlisted the energies of the artist; for where is there a field in which his God-given powers would be of a greater benefit to his fellow-men than this unexplored, almost virgin, region, where, like in a silent forest, a thousand voices respond to every call?

— Tesla On Electricity 1897

The electric motors made their first appearances in the middle of the XIX century right after the invention of the battery by the Italian physicist, chemist and inventor Alessandro Volta in 1800, the discovery of the generation of a magnetic field from an electric current by the Danish physicist and chemist Hans Christian Ørsted in 1820 and the invention of the electromagnet by the English physicist William Sturgeon in 1825 (Doppelbauer, 2012). After these foundations were laid, the development of a machine that generates mechanical power from electrical power has been improving day by day, and, along with that improvement, also its utility has been increasing.

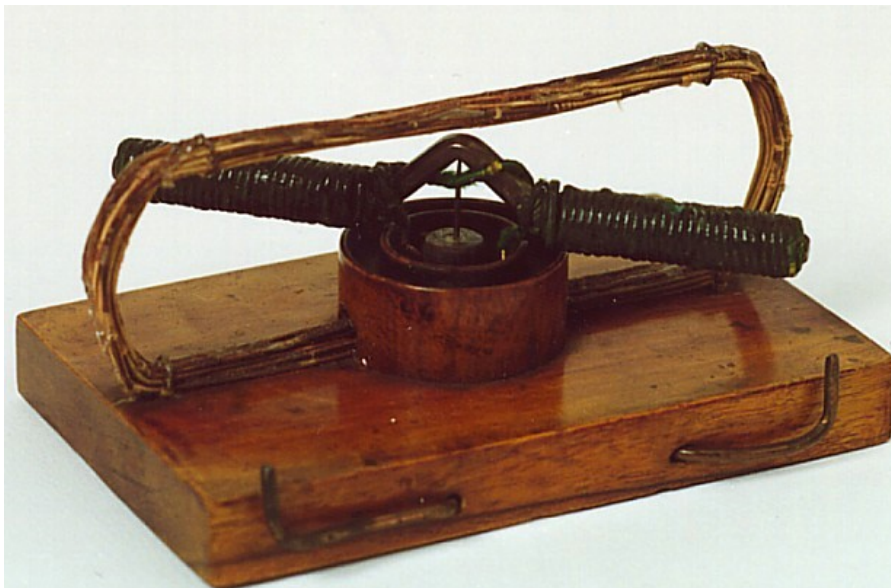


Figure 1.1: Jedlik's "Electromagnetic Self-Rotor". The historic motor created by the Hungarian physicist Ányos Jedlik still works perfectly today in the Museum of Applied Arts in Budapest.

Due to the reduction of the prices of metals and the improvement and automation of manufacture processes, electric motors became

available for a large range of applications, and not only as a research topic, up to the point that nowadays we interact with them in our daily life, sometimes without even noticing it. We have electric motors in all types of devices, from small applications like home appliances and hand-held gadgets, to large applications like robotics, cars and spaceships. As the complexity of the application increases, also the need for accuracy and efficiency does, leading to the development of more advanced electric motor technologies which lead to complex motion control techniques.

One of the most complex applications for motor control is robotics. The motion in a robotic system is part of its definition of automatic movement, therefore, a robotic system needs a predictable driving system to fulfil its purpose, which implies that most of the parameters of the motors inside the robot are known and that they can be controlled in a correct and precise way.

A challenging application regarding motors in robotics is the wheel driving, since it needs to be precise and powerful at the same time to transport the robotic system around large surfaces in an unmanned way, which means that there is no person on board and controlling the robot. For example, in robotic agriculture, which is one of the main reasons why this work was developed, a robot becomes an unmanned vehicle, which must transport itself around in farms, where the road represents harsh conditions for transportation, introducing the need for a precise drive to deal with small crops, a high torque to transport the robot in uneven grounds and a good range of speeds to displace itself in large field areas in the fastest way possible.

With aims to propose a solution for the land transportation in robotic agriculture projects, different types of motor technologies were studied a priori, finding out that in-wheel permanent-magnet brushless motors are one of the most suitable and currently used solutions to develop electric vehicles, since they don't need an external system for power transmission from the motor to the wheels, taking advantage of the high stall torque property of the electric motors and the reduction of the space and weight that having a motor inside a wheel represents (Bascetta, Baur, and Gruosso, 2017).

To correctly drive permanent-magnet brushless motors, it is necessary to apply a proper driving technique, which becomes a complex task when the goal is to achieve the desired characteristics mentioned previously: a good precision, a high torque and a large range of speed. Given such a challenge, the development of electric motor drives becomes one of the topics that draws the interest of many engineers and scientists, also due to the multidisciplinary approach needed to reach the speed, torque and efficiency required to drive the development that the inventions of tomorrow require. The approach to improve the motor drive in the electronics engineering field is directly related to the development of the driving circuit topology and to the imple-

mentation of complex control algorithms in embedded software that improve the performance of the different motor technologies available.

Since the brushless motor technology is quite recent in comparison with the rest, there is still a lot of development going on regarding its driving, with aims to reach the highest efficiency possible at the lowest cost. The objective of this work was to develop an electronic driver to control brushless motors, taking as a study case the in-wheel motors that transport a skid-steering robot designed for robotic agriculture. We studied the available electronic architectures to design a motor driver, the different approaches to drive brushless motors, like the trapezoidal and the sinusoidal drive and the peripherals needed to make these driving happen. After studying these topics, the motor driver was physically implemented and tested, and from this, a new architecture was proposed from the results and conclusions obtained from the implementation and testing of the circuit.



Figure 1.2: Rimac Automobili's electric supercar Concept S. Electric cars are becoming a trend and one of the main drivers for the development of technology related to electric motors.

This thesis explains in detail the most important information regarding the physical implementation of a motor driving system in such a way that it can be fully replicated. In Chapter 2, we explain more in detail the different reasons why this work was developed and the focus points that were stressed out. In Chapter 3, a simple but sufficient explanation about the theory behind the electric motor is given, explaining also the different existing technologies and their particular driving methods. In Chapter 4 we explain the study case of ROBI', a prototype mobile manipulator for agricultural applications, which uses the in-wheel motor for which the motor driver of this work was developed. In Chapter 5 we explain in deep detail all the work developed around the implementation of the motor driver, both

in the software and the hardware fields. In Chapter 6 we explain the final results of the work, showing and comparing graphs and waveforms of the behaviour of the in-wheel motor driven by the system developed. Finally, on Chapter 7, we discuss the results of the work realized and propose a new system, based on the implementation of the researched architecture and the problems encountered while working on the project.

2

PROBLEM STATEMENT

As motion applications complexity increases, like in the robotics field, the need for a more complex and robust driving system arises, and with it, the need to make decisions regarding the technologies to be implemented for them. For example, when a robotics project begins, with the objective to implement a solution that hasn't been implemented before, one of the main concerns is the motion system. The selection of the motor that is going to be used in a project is not an easy task, since many details must be considered, like the speed and torque required by the application, which lead to the selection of the motor technology, which might be limited by the available power source, the computing power and the economic budget of the project. These aspects have a strong dependency between each other and choosing each one of them represents a trade-off that must be studied in detail to reach an optimal result for the desired application.

2.1 TECHNOLOGICAL TRADE-OFFS

One of the main goals in the technology research and development has always been to reduce the trade-offs between the most important parameters in different engineering applications, using the most suitable technologies available, depending on the application requirements. One of the fields of engineering that has a big focus on the reduction of trade-offs is the motor drive research, since their development is crucial to drive innovation in many engineering fields.

A complicated trade-off to deal with is the cost of a motor drive, which is one of the most limiting characteristics project developments, both for research activities and for industrial and consumer applications. If a project is not expected to generate an income after its development or it's not backed up by a research institute with resources, or if the product is expected to be kept at a low price for many different reasons (like accessibility for low income communities or the possibility of large expansion), the price of a motor drive might be the weak side in a trade-off analysis and the development of the project might not be optimal, since it might require more work to reach an acceptable result.

2.2 LEARNING CURVE

The cost of a project leads to another important trade-off on engineering research and development: the learning curve. In some areas like robotics, a professional engineering project requires thousands of hours of man-work to reach a desirable result. An important amount of the time available for these projects is used in learning theory regarding the technology related to the project and how the available tools for such technology work. This time consumed in learning all the information needed regarding a project is called “learning curve”. The amount of work necessary to reach a good result makes most of the engineering projects expensive and, in many cases, a big part of that time is consumed by the learning curve, time that could be used for developing another part of the project, increasing the speed of the development and, therefore, reducing its cost.

2.3 MOTOR DRIVER DEVELOPMENT

With the aim to solve these two important trade-off factors in motor driving systems, we decided to study the possibility to reduce the cost of a motor drive by using a driver based on a cheap architecture which can be easily modified and allows to understand in a fast way how the motor driver works, making the development around it faster and easier for future projects.

To set up the design specifications for the motor driver to be studied, we based the requirements in the drive characteristics of a robot designed for robotic agriculture designed by the engineering group of the AIRLab of the Politecnico di Milano called ROBI’ (Bascetta, Baur, and Gruosso, 2017). This robot is driven by four in-wheel brushless motors that will be described in detail in Chapter 4.

2.4 IMPLEMENTATION OF FIELD ORIENTED CONTROL

Having the objective defined, we looked for an already available platform to develop a motor driver with aims to look for points to improve and define a platform that could be used for different projects involving Permanent Magnet Alternating Current (PMAC) motors, both Brushless Direct Current (BLDC) and Permanent Magnet Synchronous Motor (PMSM). With this aim, we found a board called VESC Board, developed by the Swedish engineer Benjamin Vedder, who made available all the files for its production, including the schematic circuits, the bill of materials, the Printed Circuit Board (PCB) layout files and the source code. Vedder’s circuit was very appealing since it had many ports available and it was based on a technology that is easy to

study since it's based in a design proposed by Texas Instrument for three-phase motors.

Since this motor driver was needed to be used in robotics applications, we had the necessity to modify the source code of the microcontroller to apply motor control methods that would be different to the ones available for the VESC board since the code available was designed to drive an electric skateboard. For this aim, we decided to develop our own source code, this way we would have control over everything developed by us and the expansion of the code would follow up without the need of doing reverse engineering over the code that was already available.

Since the motors of the wheels of the robot are PMSM, they have a sinusoidal configuration, and therefore, a sinusoidal waveform was needed to be applied into the motor to reach an optimal efficiency and to control the speed even in low speeds. This specification pointed us towards the implementation of the Field Oriented Control (FOC) method, which improves the torque capabilities of the motor at controlled low speeds as it will be explained in Chapter 3.

3

MOTOR CONTROL THEORY

In this chapter, we will review the theoretical principles that concern us regarding motor control. First, we will review the physical principles that rule over the electric motors and we will explain the different motor technologies and its configurations, focusing in the Permanent Magnet Alternating Current (PMAC) motors. Later, we will review the motor drives, the configuration of a driver and the different driving techniques for the PMAC motors. Finally, we will explain the most common control methods that can be applied to them.

Even if this chapter might seem too overwhelming due charge of theory contained on it, all the theory explained on it will help us develop the brushless motor driver for which this thesis is developed.

Most of the theory in this chapter was taken from the book *Tecnologie dei sistemi di controllo*, by Magnani, Ferretti, and Rocco, 2007 and from the compilation *Performance and Design of Permanent Magnet AC Motor Drives*, by Bose et al., 1989, as well as from the *Lecture notes in Power Electronics*, by Ghioni, 2016.

3.1 ELECTRIC MOTOR

An electric motor is an electric machine that transforms electrical power (product between voltage and current):

$$P_{electrical} = V \cdot I \quad (3.1)$$

into mechanical power (product between torque and angular speed):

$$P_{mechanical} = T \cdot \omega \quad (3.2)$$

by means of the electromagnetic phenomena that takes place inside the motor, which is explained by the physical principles mentioned in this chapter.

3.1.1 Physical Principles

The generation of torque in electric motors is based in the interaction of two magnetic fields, one generated by magnets or windings placed in the stator and the other one generated by magnets or windings placed in the rotor as seen in Figure 3.1.

The physical laws that rule over the torque generation in the electric motor are mainly four: The Lorentz's Law, which helps us define the

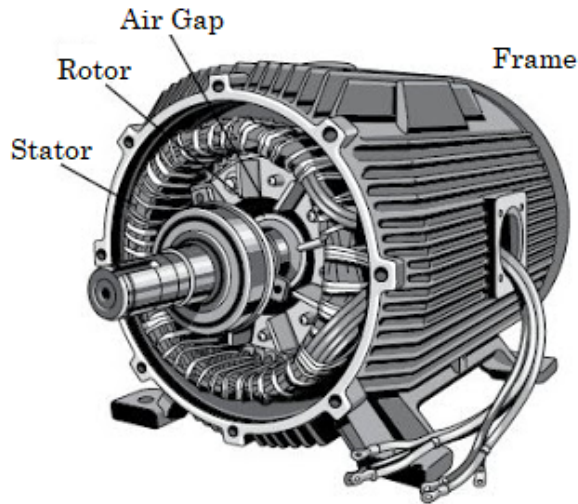


Figure 3.1: Partially Assembled Motor. An electric motor consists mainly in three parts: a rotor, which moves due to the electromagnetic interaction; a stator, the body of the motor; and a frame, which holds the rotor and the stator together. The air gap is the space between the rotor and the stator, where the electromagnetic interaction takes place (*Electrical Motors Basic Components*, 2012).

torque generated by an electric charge moving inside a magnetic field; Faraday's Law of Electromagnetic Inductance and the Lenz's Law, which explain the generation of the Back Electromotive Force (BEMF) in the motor coils depending on the speed of the rotor and the influence of the magnetic field generated due to this BEMF respectively; and the Ampere-Laplace Law, which allows us to calculate the magnetic field of a current loop and the mechanical interaction between two magnetic fields.

LORENTZ'S LAW defines a force F , which acts over an electric charge q moving with a speed v inside a magnetic field with intensity B :

$$F = qv \times B \quad (3.3)$$

as seen in Figure 3.2. By defining a current I passing through a conductor with length l we can transform Equation 3.3 into Equation 3.4:

$$F = II \times B \quad (3.4)$$

Considering the current I flowing through a conductive loop as the one in Figure 3.2 with sides lengths l and h we can see that there is a force F generated in the direction of the cross product

of the current I and the magnetic field B . The maximum force F is generated in the sides of the loop where the direction of the current I is perpendicular to the direction of the magnetic field B (ab and cd), while on the other two sides (ad and bc) the forces generated are cancelled with each other due to the direction of the current respect to the magnetic field.

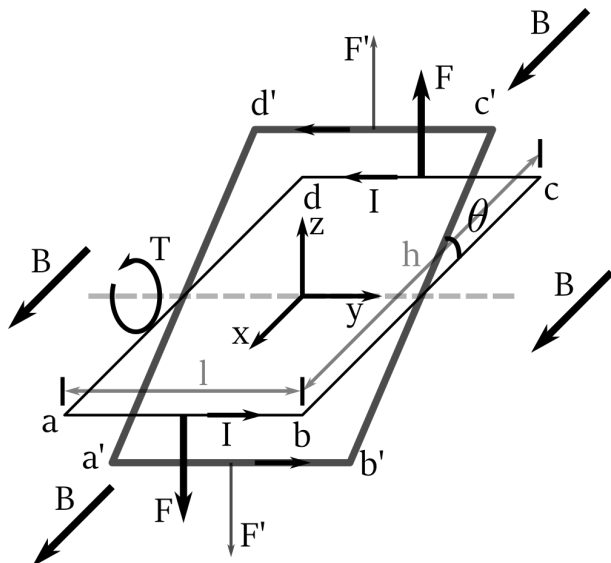


Figure 3.2: Visual explanation of the interaction of the current I and the magnetic field B generating a force F and, consequently, a torque T around the y axis (Magnani, Ferretti, and Rocco, 2007).

Since the forces F generated on the sides ab and cd have the same magnitude but different direction, they create a torque T around the y axis defined by the magnetic field, the current and by the length of the sides of the loop as:

$$T = IhlB \cos \theta \quad (3.5)$$

We can see in Figure 3.2 and in Equation 3.5 that when the angle θ between the sides ad or bc and the direction of the magnetic field B is $\pi/2$ radians, the torque T is zero and when the angle θ is zero or π radians, the torque reaches its maximum possible value.

The dependency of the torque created by the interaction of the current and the magnetic field on the angle between these two physical quantities introduces the need of changing the direction of the magnetic field or the direction of the current, hence, the polarity of the loop, to maintain the loop spinning and a non-zero torque.

FARADAY'S LAW OF ELECTROMAGNETIC INDUCTION states that

In every circuit under the effect of a magnetic field, an electromotive force is induced equal to the derivative respect to the time of the magnetic flux passing through the circuit, with negative sign (Jordan, 1968).

therefore, by indicating with E the electromotive force and with ϕ_m the magnetic flux, we have:

$$E = -\frac{d\phi_m}{dt} \quad (3.6)$$

If we consider a case like the one in Figure 3.2 we can calculate the magnetic flux passing through the loop as:

$$\phi_m = B \cdot u_N S = B \cdot u_N h l = h l B \sin \theta \quad (3.7)$$

where S is the surface of the loop and u_n is the direction normal to the plane of the loop. Therefore, we get an induced electromotive force of:

$$E = -\omega h l B \cos \theta \quad (3.8)$$

where ω is the angular speed of the loop. We can see, comparing Equation 3.8 and Equation 3.5, that the induced electromotive force depends on the angular speed in the same way than the acting torque depends on the current.

LENZ'S LAW can be explained after the explanation of the induced electromotive force. It states that the induced current in a loop has the direction that creates a magnetic field that opposes the change in magnetic flux through the area enclosed by the loop, therefore, the induced current tends to keep the magnetic flux ϕ_m from changing in the circuit.

If the rotation of the loop is generated by the circulation of a current inside a magnetic field, the induced electromotive force will try to oppose to the pass of the current, that's why it's normally referred to as Back Electromotive Force (BEMF).

AMPERE-LAPLACE LAW is the last piece to understand the transformation of electrical energy into mechanical energy. It allows us to calculate the magnetic field generated by a closed loop conducting current in a point defined by a vector p as:

$$B(p) = \frac{\mu_0}{4\pi} \oint I \frac{u_t \times u_r}{r^2} dl \quad (3.9)$$

where μ_0 is the vacuum magnetic permeability constant, I is the current circulating through the loop, u_t is the versor with direction of the current in the infinitesimal element dl and u_r and r are versor and module that define the point p respect to the infinitesimal element of the loop.

Given that the magnetic fields can be generated both by permanent magnets and by current circulation, the electromechanical conversion is obtained due to the interaction of two magnetic fields according to the alignment principle, which states that

In a region of space which hosts two magnetic fields, there is a mechanical action that tends to align both fields. (Magnani, Ferretti, and Rocco, 2007)

If we consider the loop from Figure 3.2 and Equation 3.9, we can see that there is a magnetic field generated around the loop as seen in Figure 3.3, and due to the alignment principle, we will get the strongest coupling torque when the magnetic fields are perpendicular to each other.

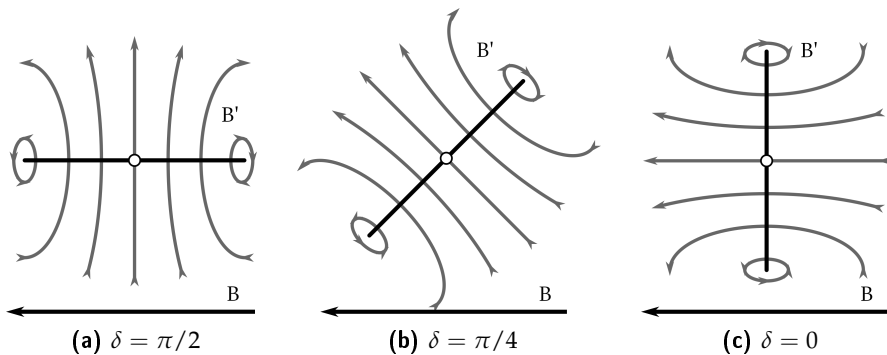


Figure 3.3: Visual explanation of the alignment principle. In this Figure we can see the side bc of the loop from Figure 3.2, which is spinning around the y axis. The alignment torque between B and B' is the largest in the configuration 3.3a and nule in the configuration 3.3c.

In the case of electrical motors, there are two different magnetic fields generated in the airgap due to the permanent magnets or to the windings placed in the stator and the rotor which can be considered in radial direction, described by two magnetic fields $B_r(\theta, t)$ and $B_s(\theta, t)$, from which interaction we get the electromechanical conversion, since we have the generation of a torque which tends to align the two fields angles where they have the largest intensity. The alignment torque will be an expression of the type:

$$T_m = k B_r B_s \sin \delta \quad (3.10)$$

where δ is the de-phasing angle between the two fields and the maximum torque will be when $\delta = \pi/2$. In conclusion, by feeding the windings in the right way, we look forward to having a constant 90° de-phase between the two magnetic fields in aims to obtain the maximum torque generation.

In the case of the Direct Current (DC) motor, the perpendicularity condition between the magnetic fields is maintained by a polarity commutating structure attached to the rotor which is connected to the windings where the current flows and generates the rotor magnetic field that tries to align itself to the magnetic field of the permanent magnets attached to the stator. This commutating system is connected to the power supply by means of metallic brushes that energise the motor until it reaches a certain angular position and the commutating lead changes to the next one, changing the polarity of the windings. Therefore, the torque obtained is independent from the position of the rotor and it's proportional to the amplitude of the power source.

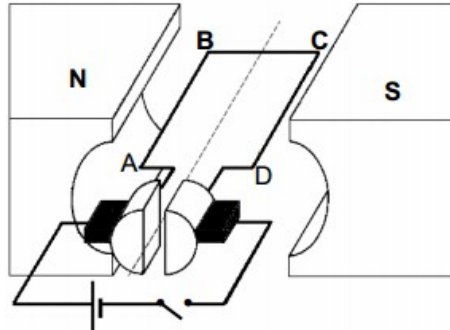


Figure 3.4: Basic schematic representation of the DC motor using the same loop represented in Figure 3.2

In brushless motors, which will be explained later in this chapter, the perpendicularity condition is maintained by feeding in the right time the windings in function of the angular position of the rotor θ .

Finally, after all the electromechanical phenomena that interacts inside the motor has been explained, we can obtain the electromechanical conversion between $P_{\text{electrical}}$ and $P_{\text{mechanical}}$.

If we clear from Equation 3.5, the torque T and the current I , grouping the rest of the variables into one constant, we can write down the following equation:

$$T = K_T I \quad (3.11)$$

where K_T is called Torque Constant and is defined by the geometry of the motor and the magnetic field in the airgap of the motor, which depend on the motor configuration and its construction technology. K_T units are Nm/A .

We can do the same with Equation 3.8, clearing the BEMF and the angular speed ω , getting the following equation:

$$BEMF = K_E \omega \quad (3.12)$$

where K_E is called Voltage Constant and it's defined also by the type of motor we are using. K_E units are $V/(rad/s)$.

If we consider the loop of Figure 3.2 as an equivalent circuit like the one in Figure 3.5, where the inductance L is generated due to the windings of the coil into the rotor, and R is the resistance of the conductive material, we can write the Kirchhoff's Voltage Law on its terminals as:

$$v(t) = RI(t) + L \frac{di(t)}{dt} + bemf(t) \quad (3.13)$$

which at steady state, when the current is constant, becomes:

$$V = RI + BEMF \quad (3.14)$$

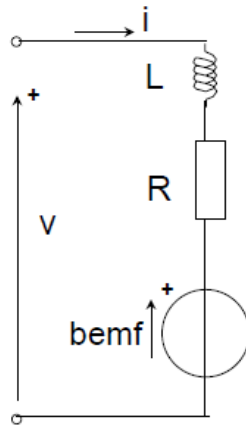


Figure 3.5: Equivalent circuit representation of a motor winding.

We can write down that the net power input into the circuit of Figure 3.5, $VI - RI^2$, is equal to the electrical power absorbed by the BEMF:

$$P_{electrical} = BEMF \cdot I = K_E \omega I \quad (3.15)$$

and we can also see that the mechanical power can be written using these new constants:

$$P_{mechanical} = T \cdot \omega = K_T I \omega \quad (3.16)$$

The two constants, K_E and K_T , synthesize the most important parameters used in the electromechanical power conversion in an electric motor. If we impose a voltage difference between the terminals of the loop of Figure 3.5, we create a current I that depends on the loop impedance. From Equation 3.11, we can see that such current will generate a proportional torque T . In the same way, from Equation 3.12, we obtain that the BEMF generated by the movement of the coil, due to the generated torque, will define a proportional angular speed ω . If we rearrange the terms from Equation 3.14 using Equations 3.11 and 3.12, we can see the interrelation between the rotating speed of the motor ω and the torque T being generated:

$$\omega = \frac{V}{K_E} - \frac{R}{K_T K_E} T \quad (3.17)$$

which defines, by imposing a voltage difference between the terminals of the loop, the torque T vs angular speed ω curve that characterizes the mechanical behaviour of an electrical motor.

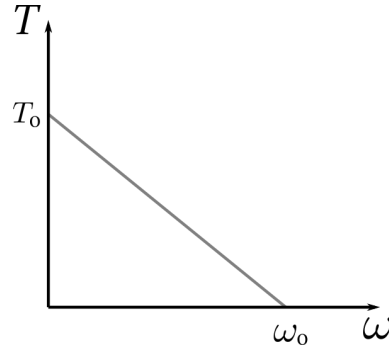


Figure 3.6: Basic representation of the Torque vs Angular Speed characteristic curve of an electric motor

If the speed of the motor ω is equal to zero, then we can rearrange the terms and see that the torque T is defined by $K_T V / R$, which is the maximum torque that the electric motor can provide by a given voltage, also named Stall Torque, T_0 . We can also define a no-load speed ω_0 , for the case when there is no load influencing over the movement of the rotor, as V / K_E .

The relationship between torque and angular speed established in Equation 3.17 will help us select the voltage that we need to regulate in order to control the dynamics of the motor.

It is important to mention that these equations also work if there is an imposed angular speed ω . If we impose an angular speed to the rotor, the motor works as a voltage generator:

$$V = K_E \omega + R \frac{T}{K_T} \quad (3.18)$$

therefore, if we connect the motor to a load, it generates a voltage proportional to the driving speed and provides a current proportional to the torque driving the rotor. This behaviour is used in the so-called regenerative braking, since we can obtain energy when we want to stop a motor which is moving due to an inertial torque.

3.2 PMAC MOTORS

The Permanent Magnet Alternating Current (PMAC) motor is a type of electrical motor that doesn't need the mechanical commutators mentioned in 3.1.1 to be driven as in the case of the DC motor, but its windings need to be energised in a specific sequence to commutate and function correctly by means of an inverter. Since it doesn't need the mechanical commutators, it also doesn't need the brushes that energise the windings, so it can be said that it's a brushless motor. As seen in Figure 3.7, there are permanent magnets attached to its rotor. The stator consists of stacked steel laminations on which the coils are wound in a three-phase configuration.

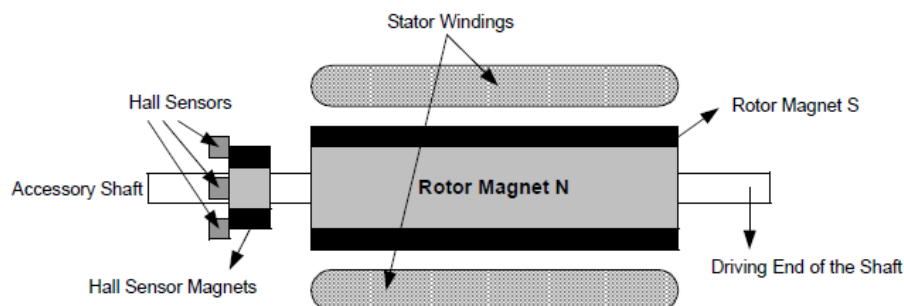


Figure 3.7: Brushless motor transverse section (Yedamale, 2003).

These three phases are feed alternatively in such a way that the magnetic field, generated by the relative currents passing through the coils, should always be orthogonal and synchronous to the magnetic field generated by the rotor's permanent magnets. The characteristics mentioned above give the name to this kind of motors.

To maintain the synchronization, it's necessary to commute, by means of an inverter, the currents in the windings of the stator, taking as a reference the angular position of the rotor, which must be obtained by a sensor.

The number of commutations needed to generate one revolution of the rotor is determined by the number of magnetic Pole Pairs (PP) of the permanent magnets attached to the rotor. One PP is defined by 2 magnets attached to the rotor, one with the north pole facing out in one side of the rotor and one with the south pole facing out in the opposite side of the rotor. Normally, the PMAC motors have many PP (four or more) in order to have a lower torque ripple since the alignment of the magnetic fields would be every $360/(PP \times \Phi_N)$ degrees

of the rotor, where Φ_N is the number of phases in the motors. For the electromechanical conversion, the angular position of the rotor is substituted by an electrical angular position, which is controlled by the commutator and is defined by:

$$\theta_{electrical} = PP \cdot \theta_{mechanical} \quad (3.19)$$

which also represents a relationship between the mechanical speed of the rotor and the electrical speed of commutation, which is defined by the commutation frequency:

$$\omega_{electrical} = f_{commutation} = PP \cdot \omega_{mechanical} \quad (3.20)$$

so, for example, if we have a motor with 6 PP and we want to drive it at 1kHz, we must commutate the polarity of the inverter at

$$f_{commutation} = PP \cdot \omega_{mechanical} = (6)(1\text{kHz}) = 6\text{kHz} \quad (3.21)$$

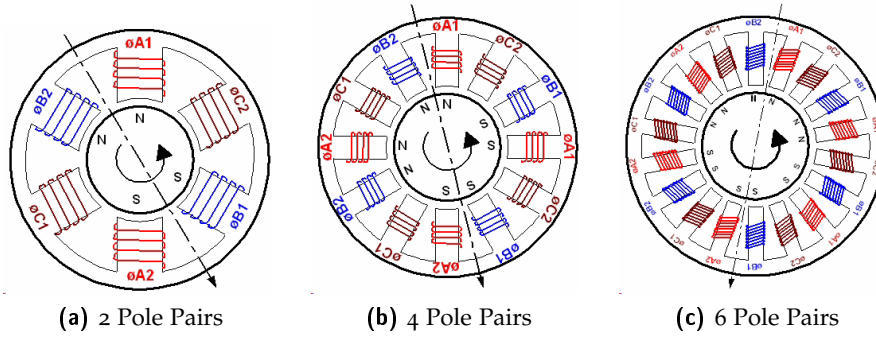


Figure 3.8: Different pole pair configurations (BASIL Networks, 2003)

The main characteristics that make the brushless motor a better option for some applications than the DC motor are the following:

- better weight-to-power ratio,
- a more linear acceleration,
- a low inertia,
- a higher reliability,
- smaller dimension,
- reduced need for maintenance,
- high rotation speed,
- ideal for working in hostile environments

but there are two disadvantages to this motor technologies:

- need of a rotation sensor,
- need of a complex logic to commutate the currents flowing through the coils

Both of these disadvantages are mainly reflected in a higher price respect to the DC motor.

It is possible to identify mainly two types of brushless motors. The first one is the Brushless Direct Current (BLDC) motor, which has a rotor position feedback that is not continuous, since the position of the rotor is given every 60 electrical degrees and its feed in blocks of 120 electrical degrees by simply alternating the voltage in the inverter, and due to these alimentation in blocks, the driving is rectangular, so the ideal BEMF is trapezoidal. The second type of brushless motors is called Permanent Magnet Synchronous Motor (PMSM), and it needs a continuous rotor position feedback to feed the motor with sinusoidal current, obtained by Pulse Width Modulation (PWM) of the DC bus, therefore the ideal BEMF is sinusoidal, which generates a lower torque ripple than the trapezoidal one, but needs a more complex control method.

3.2.1 BLDC Motors

The stator winding for each one of the three phases of the BLDC motor consists of a uniform distribution of turns over $N = PP$ sectors of a width equal to 60° . The magnets attached to the stator cover an arc of 180° , and at any instant, each magnet interacts, for 120° , with an arc of stator conductor carrying current.

Due to this "discrete" interaction every 120° , the three-phase switching between the currents of the stator should happen when the edge of the magnet attached to the rotor reaches the boundary between windings every 60° , therefore, a trapezoidal BEMF is generated in its coils.

The boundary of the rotor magnets with respect to the windings position is detected by three sensors, one every 120° , which send a signal to the driving circuit to change the polarity of the coils depending on the actual value of the three sensors and on the desired direction. The sensors to detect the angular position will be explained in 3.3 and the driving sequences will be explained in 3.4.

3.2.2 PMSM Motors

The stator of the PMAC motor is fitted with three-phase windings with $N = PP$ turns of each phase distributed sinusoidally around the periphery. If the stator windings are feed by sinusoidal currents,

there is a linear current density around the stator periphery and a sinusoidal BEMF is generated in its coils.

Since the sinusoidal feeding of the current into the coils depends continuously on the magnetic field of the rotor permanent magnets, it is necessary to use an angular position sensor attached to the rotor. The sensors to detect the angular position will be explained in 3.3 and the driving algorithm will be explained in 3.4.

3.3 ELECTRIC DRIVES

An electric drive can be defined as an electromechanical device that converts electrical energy into mechanical energy to impart motion to different machines and mechanisms for various kinds of process control (*Ghioni Introduction to Electrical Drives*).

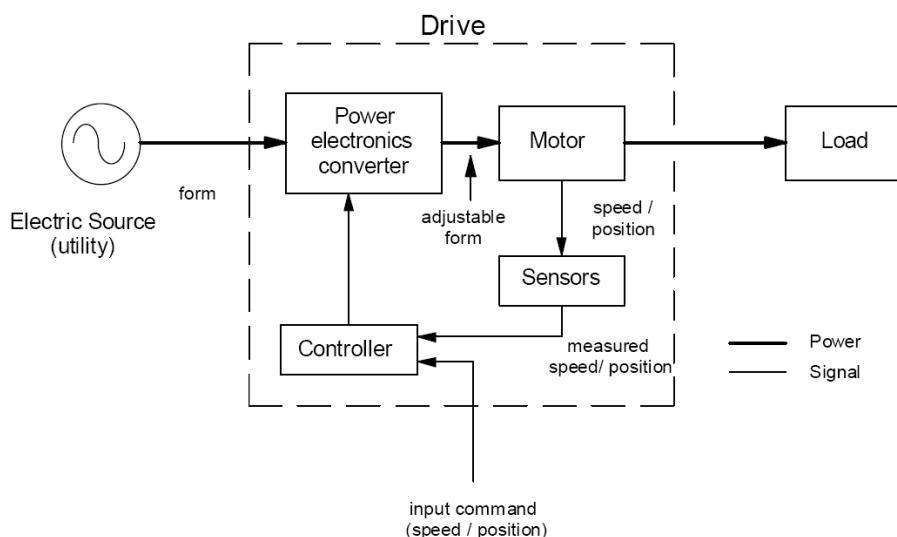


Figure 3.9: Electric Drive Scheme

The brushless motor drive, therefore, consists not only on the electric motor and the inverter, but it also includes the position, speed and current feedback systems, these being external sensors, embedded circuits or just algorithms, the vector, current, speed and position controllers and the DC power supply which can be a battery for mobile applications or a rectified power source for industrial applications.

3.3.1 Inverter

The commutation of the polarities in the windings of the PMAC motors is done by means of a three-phase inverter. The inverter used in

PMAC motors avoids the need of the mechanical commutation used in the DC motors, which creates sparks between the commutator and the brushes due to the discharge of the electromagnetic energy stored in the windings of the rotor.

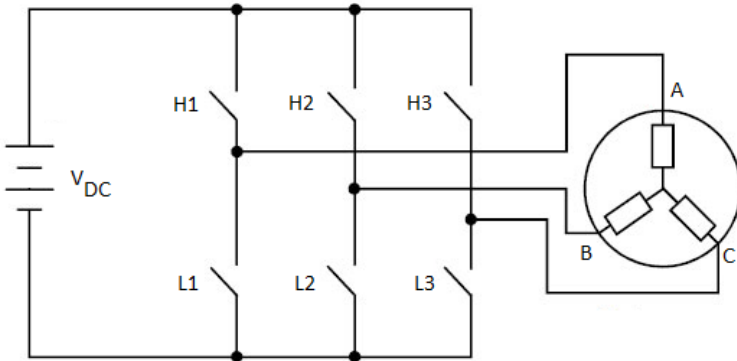


Figure 3.10: Schematic representation of a three-phase inverter

This three-phase inverter configuration consists on 3 branches with 2 switches each one. The switch connected to V_{DC} is called high-side switch, while the switch connected to 0V is called low-side switch. The middle point between the two switches in each branch is connected to each one of the phases of the motor. To feed the coils of the motor, we need to activate the switches in such a way that the current comes into one of the phases and goes out through another phase. For example, if we want to feed a current through phase U and we need it to come out through phase V to generate a magnetic field in a certain angle, we would enable switches $S1$ and $S6$, having a phase-to-phase voltage in the U and V coils equal to V_{DC} . The correct feeding sequence should be synchronous with the rotor position to generate an angular rotation of the rotor with the lowest possible torque ripple.

The switching in the three-phase inverter is made by transistors as seen in Figure 3.11. The transistors are chosen accordingly to the power requirements of the application on which the inverter is being used. If the DC voltage is lower than 1000V and the current is lower than 100A, it is recommended to use the Power Metal-Oxide Semiconductor Field-Effect Transistor (MOSFET) technology. If the power consumption of the motor is larger, different technologies should be considered, like the Insulated-Gate Bipolar Transistor (IGBT).

The use of recirculation diodes is necessary to avoid damage in the transistors due to the overvoltage generated by the current transients in the windings LdI/dt that takes place between the switches of a same branch of the inverter while switching from one state to another. For example, when a transistor is suddenly turned off, the current flowing through the coils doesn't instantly disappear, but instead it recirculates through the diodes until it vanishes.

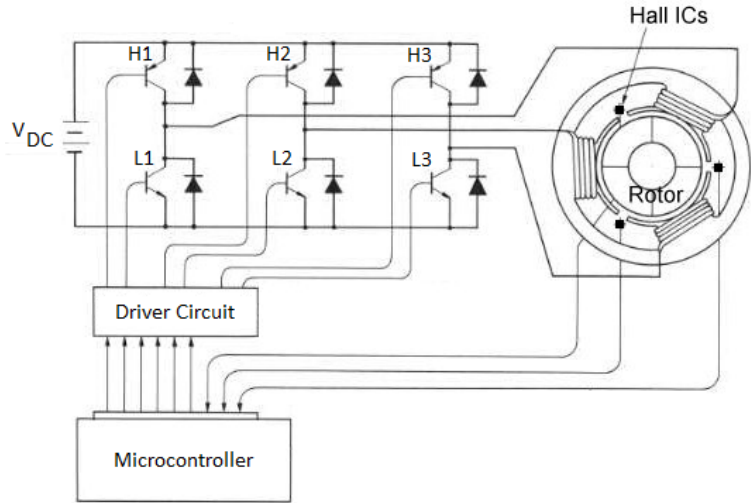


Figure 3.11: Schematic representation of a three-phase inverter built with transistors

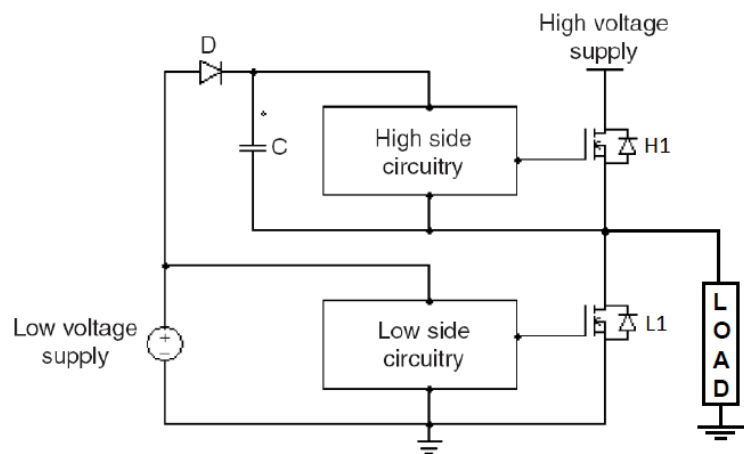


Figure 3.12: Power MOSFET devices require a dedicated circuit to provide enough voltage and current to drive their gates

Since Power MOSFETs have large parasitic capacitances, they can't be driven by typical CMOS (0 to 3V) or TTL (0 to 5V) logic signals, which typically have a low current driving capability. Instead, to drive a power MOSFET is necessary to use a more complex driving circuit to rapidly charge the capacitance of the gate and reach a value of V_{GS} large enough to switch the device. Some integrated circuits provide solutions to solve this problem. These integrated circuits can be considered as part of the inverter, because without them, the inverter won't be driven correctly.

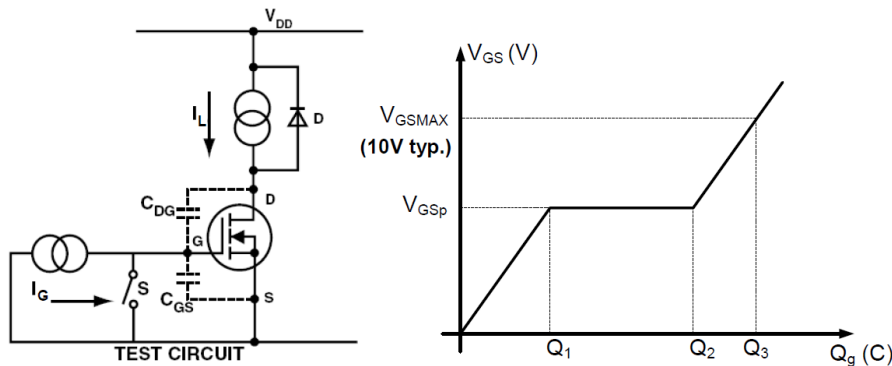


Figure 3.13: Schematic representation of the components influencing on the driving of a Power MOSFET

3.3.2 Angular Position Sensors

It is strictly necessary to obtain the angular position of the rotor in order to energise the coils of a PMAC motor in a synchronous way. The angular position detection can be made in different ways, but the solutions are mainly separated into two groups: sensored and sensorless.

The sensored angular detection is made by an external device, which creates a signal that allows us to know the angular position of the rotor. Typically two different approaches are used for the sensored angular detection. The first approach, and the simplest one, is the use of Hall effect sensors. Hall effect sensors are transducers that variate an output voltage signal in response to a magnetic field acting over them, and depending on their configuration the output can be digital (high or low signals) or analog (the output voltage variates proportionally to the detected magnetic field strength). In the case of the brushless motors, since the rotor has permanent magnets attached to it, three Hall effect sensors are mounted inside the motor frame in order to read the magnetic field of those permanent magnets and create a digital output that helps us determine the angular position of the rotor. The Hall effect sensors are mounted every 120 electrical degrees, so they can be mounted in different positions around the rotor, but they will change the output signal every 60 electrical degrees, depending

on the pole orientation of the rotor. This approach is mainly used in BLDC motors, since they are wounded in a trapezoidal distribution with aims to use only these simple sensors and an inverter.

The second approach to the sensored angular detection is the use of absolute rotary encoders. These encoders are attached to the shaft of the motor and, therefore, provide the angle of the rotor continuously. There are different technologies used for this approach. The simplest one is the resistive encoder, which is practically a potentiometer attached to the rotor's shaft, so it is prone to mechanical disturbances and noise, but is very cheap. The next approach is the optical encoder, which identifies the absolute angular position by means of attaching a disk with holes or with a pattern and optical sensors, like infrared LEDs and infrared detectors. The optical encoder is a very precise approach, but is very prone to mechanical disturbances, so it is mostly used in applications where the conditions to the system don't represent a problem to the encoder. The approach that is being used in this project to detect the absolute angular position is the magnetic encoder, which also uses Hall effect sensors for the absolute angular position determination. The difference between these two approaches is that, in this case, the Hall effect sensors of this encoder provide an analog signal proportional to the angular position of the magnetic field of an external permanent magnet, which is attached to the shaft. Another interesting technology that is being used recently is the capacitive encoder, which detects the capacitance changes, proportional to the angular position, using a high frequency reference signal. The absolute angular position detection is used mainly in the PMSM technology, since it is necessary to know the angular position of the rotor continuously to create a sinusoidal signal, to drive the sinusoidally distributed coil windings, synchronously to the magnetic field of the permanent magnets attached to the rotor.

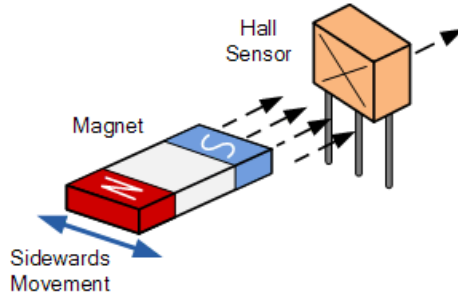


Figure 3.14: Hall Effect Sensor

One important thing that has to be considered when using absolute rotary encoders is that, even if these encoders provide the absolute angle of the rotor, they don't necessarily provide the angular position of the magnetic field of the rotor, introducing an angular slip $\Delta\theta$ which is equal to the difference between the value of the absolute rotary encoder angle and the angular position of the magnetic field.

For this reason, the three Hall effect sensors used in the first sensored approach can be found also in PMSM motors and not only in BLDC motors, since they can provide the exact position zero of the magnetic field of the permanent magnets.

The sensorless approach to obtain the angular position of the rotor consists in reading the BEMF on an undriven motor terminal during one of the drive phases. This is done by means of connecting a voltage divider to the middle point of each inverter branch, in order to read the analog voltage signal proportional to the BEMF and calculate the angular position of the rotor. This solution can be used for both BLDC and PMSM technologies. The sensorless approach reduces the size and the cost of the motor drive, and it's also useful in applications where the rotor runs immersed in fluid. Even if this method is more complex than just reading the angular position, the main disadvantage is that the motor must be rotating at a minimum rate to generate a BEMF that can be detected by the controller, therefore, this approach is not convenient in applications where a motor must run at low speeds.

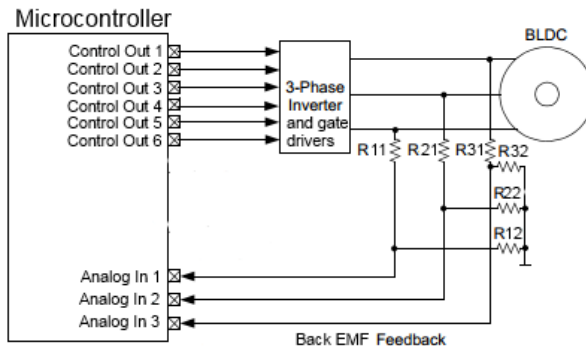


Figure 3.15: Sensorless Angular Detection Circuit

3.3.3 Current Sensors

Knowing the amount of current that is circulating through the motor windings can help us apply different control strategies to control the torque as defined in Equation 3.11. Also, reading the current can help us avoid problems of overcurrent if something goes wrong with the motor drive system.

To read the current we must install an external sensor which can be as complex as the application requires and the budget allows. The simplest approach to measure current, which is also the approach used in this project, is the use of a shunt resistor. The shunt resistor is an electrical resistor with a low (but well controlled) resistance value. This shunt resistor is placed in the path of the current flow of the motor's coils, in such a way that when the current flows through

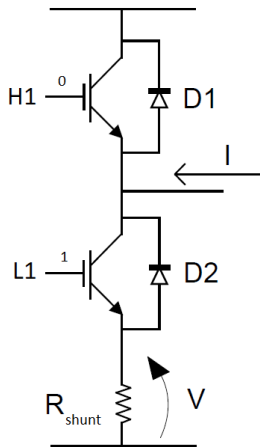


Figure 3.16: Measurement of the current flowing through a load using a shunt resistance

the resistor, we have a proportional voltage drop across it following Ohm's Law:

$$I_{\text{phase-to-phase}} = \frac{V_{\text{shunt}}}{R_{\text{shunt}}} \quad (3.22)$$

Since we need to take care of the power dissipated in the shunt resistor $P_{\text{shunt}} = I^2 R$, small resistance values R with large power dissipation capability are selected, leading to the problem that this generates a proportional voltage signal that is very small and that is prone to noise disturbances. For example, if we have a current of $100mA$ flowing through a shunt resistance of 0.001Ω , we would get a voltage drop across the shunt resistance equal to $0.1mV$, which is a very small value to be read by a typical Analog-to-Digital Converter (ADC). To solve this problem, we need to include an amplifier that allows us to read such a small voltage with a normal ADC, therefore, we can calculate the equivalent current as:

$$I_{\text{phase-to-phase}} = \frac{V_{\text{amplifier}}}{R_{\text{shunt}} G} \quad (3.23)$$

where G is the gain of the voltage amplifier.

3.3.4 Controller

The last piece on the motor drive is the controller, which executes all the logic behind the commutation of the inverter, in order to generate a synchronous driving. Previously, motor controllers were made by analog electronic circuits. Nowadays, these controllers are implemented using digital circuits that can be programmed, like microcontrollers.

The microcontroller has the task to run embedded software that contains the logic that generates a driving signal for the inverter which will depend in the desired dynamic conditions and the actual conditions of the motor, which are sensed and stored by the microcontroller.

For example, if we need to drive a motor at a desired reference speed, we need to apply a synchronous voltage signal into its coils. To generate a voltage that is synchronous to the angular position of the magnetic field, we will need to start by defining the absolute angular position of the shaft and, after this, we can apply a voltage into the coils by switching on the respective transistors of the inverter. This voltage will generate a current that will generate a torque and a magnetic field that will interact with the rotor, starting to spin it and, with this, generating a BEMF. As the rotor spins, we must keep reading its angular position, to determine the correct driving voltage needed to keep it spinning and the correct commutation of the transistors in the inverter. As the motor keeps moving, everytime faster, we need to calculate the speed at which the rotor is spinning, so as the rotor approaches the desired angular speed, we must increase or reduce the commutating frequency of the inverter, closing the speed loop. All these tasks must be made automatically by the microcontroller in a matter of microseconds.

The microcontroller handles also the interface between other devices, allowing us to modify control parameters, like the desired speed or torque, and to read different physical variables from the motor drive that are detected by the system.

3.4 PMAC MOTORS DRIVING METHODS

Due to the different configurations of the coils between BLDC and PMSM motors, there are two methods to apply a voltage into the coils, depending on the generated BEMF. To obtain the best torque using a simple driving method in BLDC motors, we can apply the Trapezoidal Driving method, which is the driving method for which BLDC motors are designed. This method can also be used in the PMSM motors, but it won't allow us to obtain the best torque available for this motor technology. To obtain a better torque in both motors, we can apply the Sinusoidal Driving method, which allows to have a better current density, mainly in the PMSM motor, but it also implies a more complex and expensive hardware architecture and the implementation of a more complex algorithm as we will see in the following.

3.4.1 Trapezoidal Drive

The trapezoidal drive is intended to create a trapezoidal BEMF, as the name indicates, by energising positively one of the windings, connect-

ing it to V_{DC} (current comming in), and negatively a second winding, connecting it to 0V (current going out), while the third winding remains floating (no current flowing through it), using the three-phase inverter explained in 3.3.1. This energising will generate a magnetic field in a certain angle that will interact with the magnetic field of the rotor, producing a torque between the rotor and the stator and, therefore, a rotation of the rotor if the load is smaller than the torque generated. The sequence of commutation that is followed to create the trapezoidal BEMF is called "six-step" commutation.

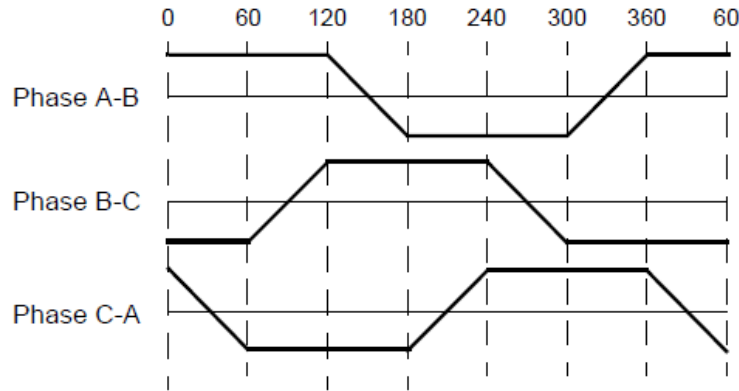


Figure 3.17: Trapezoidal BEMF

The six-step commutation is produced by following the sequence described in Table 3.1, which depends on the rotor position, which is obtained by the Hall effect sensors, and on the expected direction of rotation. This sequence generates a current circulation like the one explained in Figure 3.18, which produces a BEMF and a torque like the one shown in Figure 3.19. We can see that the torque in Figure 3.19 presents a ripple due to the non-continuous shape of the current in the coils, generated by the rectangular commutation of the six-step sequence. This current shape is defined by the electrical model of the coils of an electric motor, which follows a model similar to the one described in Figure 3.5 and Equation 3.13.

Due to the synchronous configuration of the PMAC motors, the six-step commutation frequency is defined by the rotation speed and not vice versa, unlike in induction motors. Instead, to reduce the rotation speed, we need to reduce the current flowing through the windings by reducing the voltage applied into the windings, following Equation 3.17. To achieve this with the inverter, we must follow the six-step sequence applying a PWM signal into the gates of the transistors with a frequency higher than the inverse of the time constant $\tau = L/R$ of the motor windings, which is much higher than the six-step commutating frequency. By doing this we apply an average voltage $D \cdot V_{DC}$ into the windings, where D is the duty cycle of the PWM signal.

The simplest way to do this is by applying the PWM signal to either the high-side transistor or to the low-side transistor. Due to the re-

Table 3.1: Six-Step commutating sequence

Clockwise Direction								
Step #	Hall Sensor Input			Active Gates		Phase Voltage		
	A	B	C	High Side	Low Side	A	B	C
1	1	0	0	H2	L1	0V	V_{DC}	-
2	1	0	1	H3	L1	0V	-	V_{DC}
3	0	0	1	H3	L2	-	0V	V_{DC}
4	0	1	1	H1	L2	V_{DC}	0V	-
5	0	1	0	H1	L3	V_{DC}	-	0V
6	1	1	0	H2	L3	-	V_{DC}	0V

Counter-Clockwise Direction								
Sequence #	Hall Sensor Input			Active Gates		Phase Voltage		
	A	B	C	High Side	Low Side	A	B	C
1	1	0	0	H1	L2	V_{DC}	0V	-
2	1	0	1	H1	L3	V_{DC}	-	0V
3	0	0	1	H2	L3	-	V_{DC}	0V
4	0	1	1	H2	L1	0V	V_{DC}	-
5	0	1	0	H3	L1	0V	-	V_{DC}
6	1	1	0	H3	L2	-	0V	V_{DC}

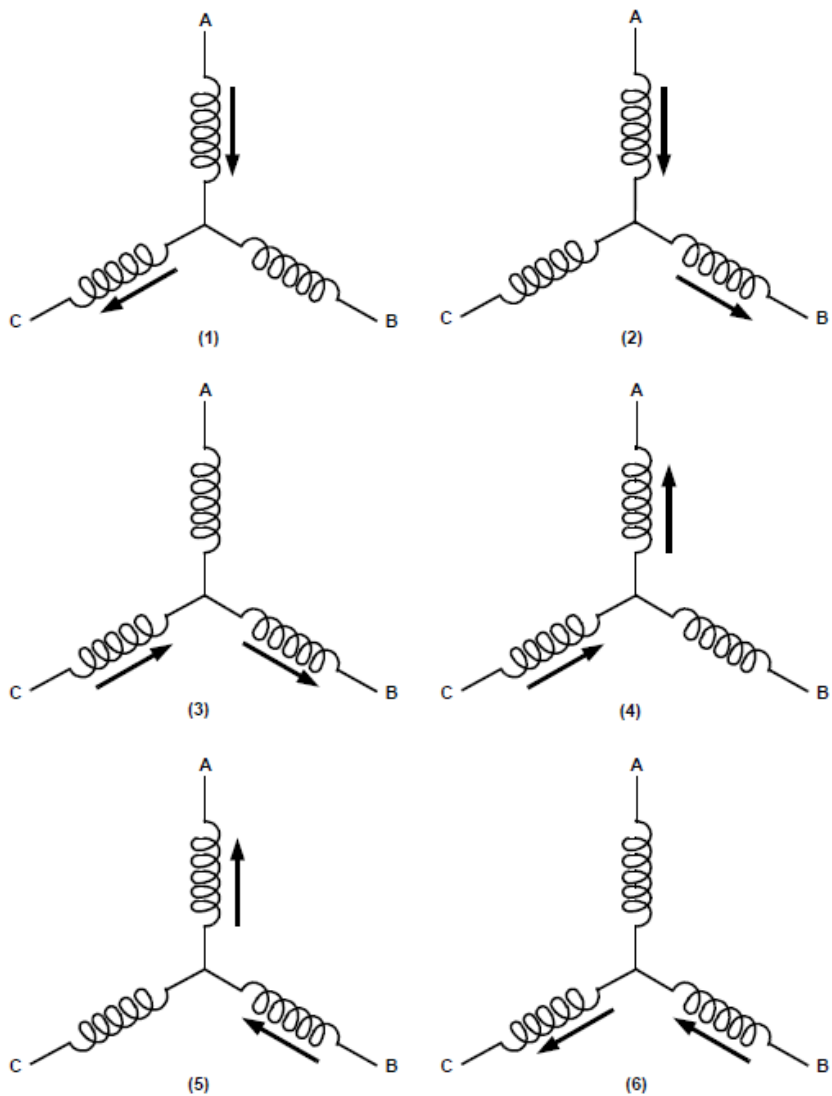


Figure 3.18: Current flowing through the coils of the PMAC motor in the 6-step commutation sequence (Yedamale, 2003)

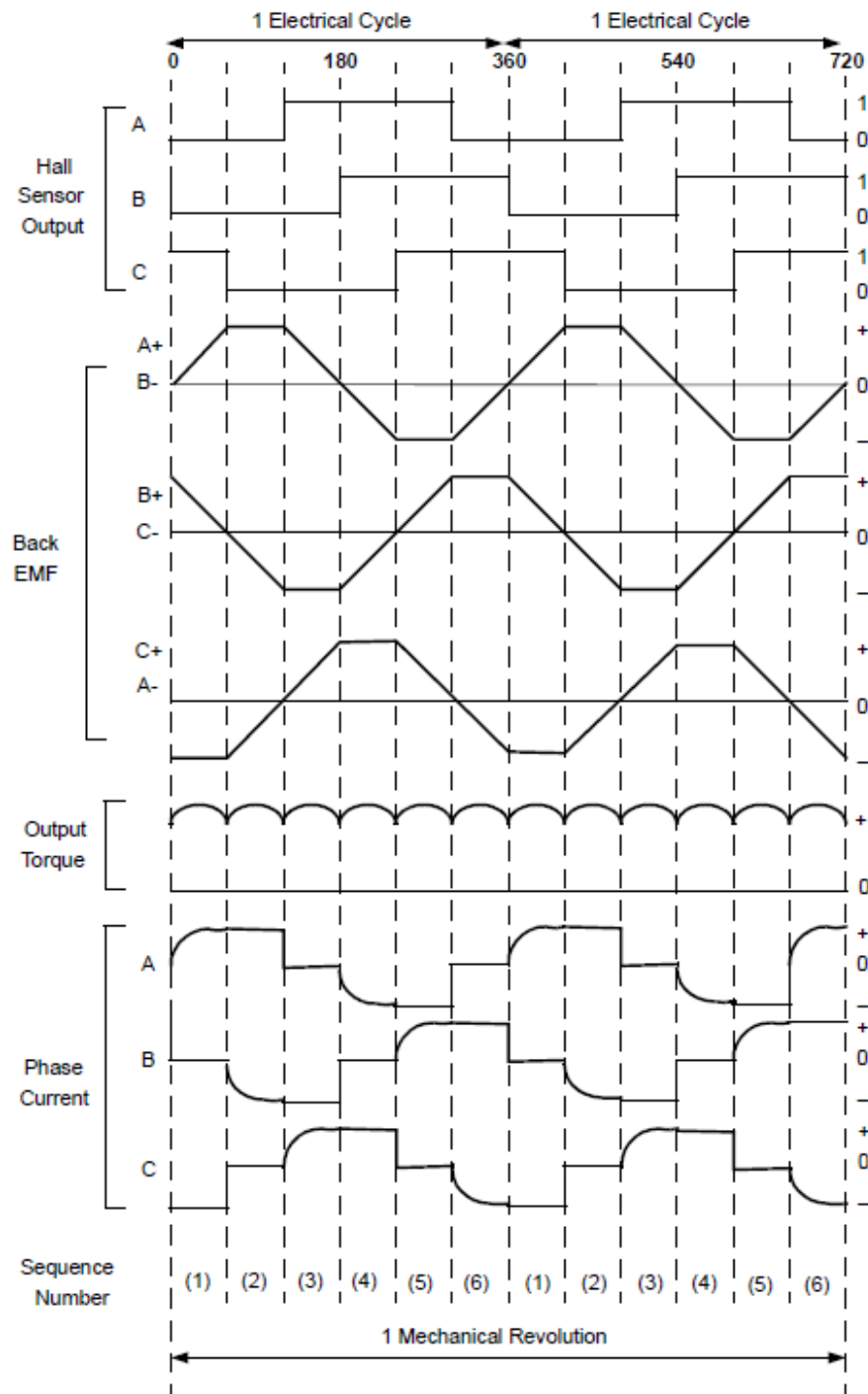


Figure 3.19: Six-Step commutation elements: Hall effect sensor signal, BEMF, current and output torque (Yedamale, 2003)

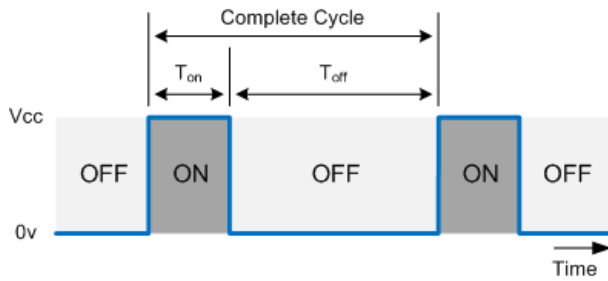


Figure 3.20: Pulse width modulation signal components

circulation diodes, the voltage in the windings energised would commutate from V_{DC} to 0V, as in a step-down voltage converter. A more complete approach to applying the six-step sequence with a lower voltage than V_{DC} to obtain a slower speed, would be to apply a complementary PWM signal to the low-side transistor on the same branch of the high-side transistor indicated on the sequence, while the low-side transistor indicated on the sequence stays enabled, as seen in Figure ???. This approach would allow us to brake the motor, enabling also the regenerative braking, since, by applying a complementary signal to the high-side transistor in the low-side transistor, we are allowing the flow of current not only from the power supply to the motor, but also from the motor to the power supply.

3.4.2 Sinusoidal Drive

The sinusoidal feeding for the PMAC motors is similar to feeding a three-phase induction motor, to which we need to provide a three-phase voltage in order to energise the windings and create a three-phase current. The difference in the power supply with the induction motor would be that the PMAC motor three-phase power supply needs to be synchronous with the rotor position. Therefore, after determining the absolute angular position of the rotor with any of the methods described in 3.3.2, we generate independent voltages for each phase using the three-phase inverter.

To generate these three independent voltage signals using the inverter, we can consider each one of the branches of the inverter as a voltage generator for each one of the phases. We can modulate a sinusoidal signal by using a PWM signal with a duty cycle D proportional to the amplitude of the sinusoidal signal, which can go from 0V up to V_{DC} :

$$D_{PWM} = \frac{v_a(\theta)}{V_{DC}} + 0.5 \quad (3.24)$$

By commutating the high-side transistor of the bridge with the PWM signal, and the low-side transistor with the complementary sig-

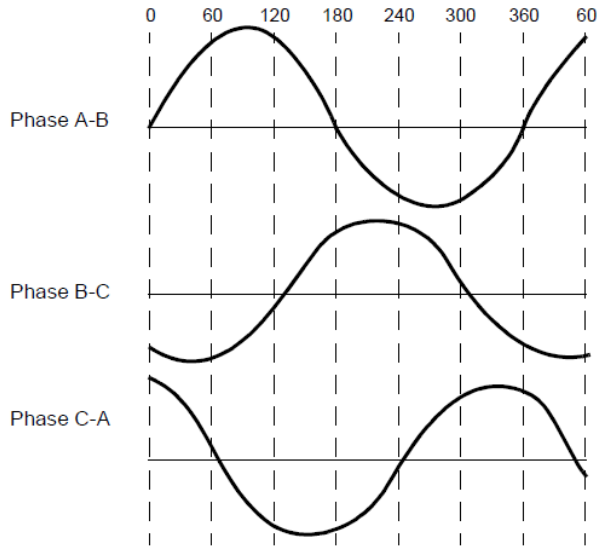


Figure 3.21: Sinusoidal BEMF

nal, in the three branches of the inverter, we generate a three-phase signal as the one seen in Figure 3.21.

It is important to recognize, from Equation 3.24, that if the voltage to be applied is larger than $V_{DC}/2$, the duty cycle D becomes larger than 1. Since a duty cycle larger than 1 doesn't make sense, the duty cycle will remain as 1 until the voltage applied becomes lower than $V_{DC}/2$, generating a trapezoidal waveform, which would have the same effect over the motor of the trapezoidal drive, losing the advantages of the sinusoidal drive.

This driving method is normally not used by itself, but it is applied in the Field Oriented Control (FOC) method, which will be explained at the end of this chapter.

3.5 ELECTRIC MOTOR CONTROL METHODS

As we have seen previously, there is a strong dependence between the rotating speed of the electric motor and the torque generated as a function of the voltage applied to its phases. This interaction can be seen in Figure 3.22. Due to this, and to the fact that there are many other external factors that might affect our system parameters, in order to obtain a desired speed or a desired torque, we can't just apply a previously calculated voltage that would give us those speed or torque values. Instead, we need to apply a control method in order to successfully reach a desired speed or a desired torque, by automatically comparing these quantities to the reference value that we want to achieve, and, in function of their difference, which is normally called "error signal" ε , change the driving signal of the inverter, using any of the previously seen driving methods.

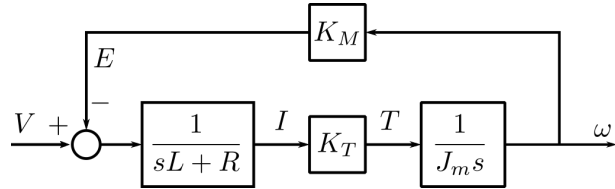


Figure 3.22: Coupling between mechanical and electrical dynamics on an electric motor

3.5.1 Speed Control

The speed control loop of an electric motor is achieved by means of applying a driving voltage into the motor coils, proportional to the error signal between a reference speed and the measured speed. This driving voltage is obtained by means of a Proportional-Integral (PI) controller. The PI controller creates a driving signal that is calculated by adding two signals. The first signal is the proportional error, which is equal to the error ε multiplied by a proportionality constant K_p . The second signal is the integral error, which is equal to the error ε multiplied by an integral constant K_i integrated over the time that the algorithm has been running (Figure 3.23).

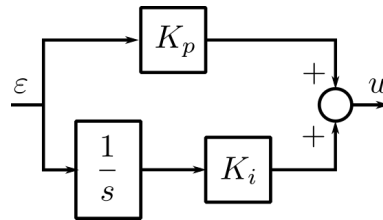


Figure 3.23: Blocks Diagram of a Proportional-Integral Controller

To apply the speed loop into the PMAC motors, we need to obtain the speed of rotation of the rotor. This can be easily done by deriving the position information provided by the Hall effect sensors embedded into the frame of the motor. After this, we calculate the error signal ε , pass it through the PI controller to generate a reference value that is applied to the inverter, which feeds the motor with the resulting voltage. As an example, we can see the speed control applied using the trapezoidal drive in Figure 3.24.

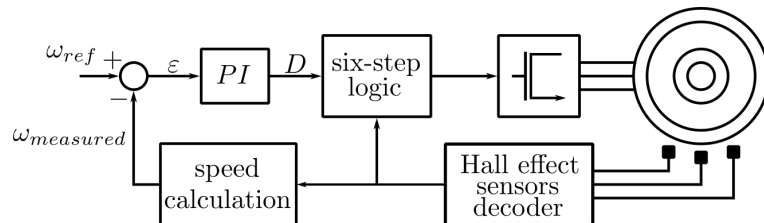


Figure 3.24: Speed Controller with Trapezoidal Drive

3.5.2 Torque Control

The torque control is based in Equation 3.11:

$$T = K_T I \quad (3.11)$$

where we can see that the torque applied by the motor is equal to the current flowing through its windings multiplied by the torque constant K_T . Therefore, we need to read the current flowing through the motor windings, using any of the methods mentioned in 3.3.3, to calculate the torque that the motor is applying by multiplying the current $I_{measured}$ it by the torque constant K_T , and comparing it with the torque T_{ref} that we want the motor to apply. As we can see in Figure 3.25, the rest of the loop is similar to the speed loop.

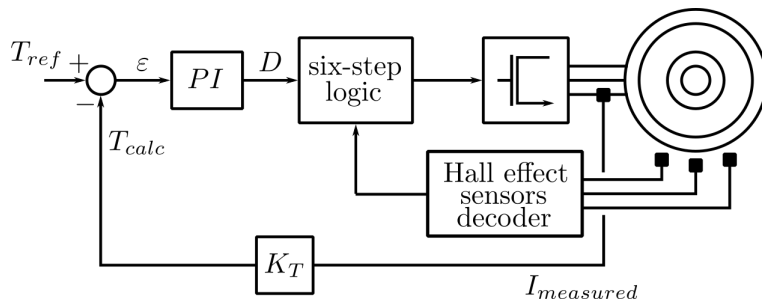


Figure 3.25: Torque Controller with Trapezoidal Drive

3.5.3 Field Oriented Control

The Field Oriented Control (FOC) or Vector Control, is technique that is applied with aims of controlling the current (and therefore the torque) of the PMAC motor in the same way that the current of a DC motor is controlled. This is done because the DC motor has the advantage that, in any case, the magnetic field of the rotor is always synchronized with the magnetic field of the permanent magnets attached to its stator due to the mechanical commutators, which makes it very easy to control. Instead, the PMAC motors must be synchronized by means of applying different driving algorithms depending on the rotor angular position, as mentioned before in this chapter.

To achieve a current control on the PMAC motors that is similar to the one on DC motors, we need to make mathematical transformations to the voltage and current values and controller variables of the system in order to control the motor using only two variables: a direct current I_d and a quadrature current I_q .

The direct current I_d is a vector that is facing always in the same direction of the north-pole of the magnetic field of the rotor, while the quadrature current vector I_q is displaced from the direct current

vector by 90° . Due to this angular displacement, we can control the current and the direction of rotation by simply changing I_q , as in a DC motor we would only need to reduce the armature current in order to reduce the torque, which is the scope of the FOC, since the maximum torque generation of any electric motor is when the magnetic fields of the rotor and the stator are displaced between each other by 90° .

The control of the direct current vector I_d allows the implementation of "flux weakening", which is a technique that aims to push the angular speed of the electric motor beyond its rated speed by reducing the strength of the magnetic field B , in order to reduce the generated BEMF, which limits the current flow in the windings. If a larger current circulates through the windings, a larger torque is developed, reaching a higher speed until the BEMF increases, preventing the current to keep increasing. By this point the electric motor is running at a higher speed but at a lower torque.

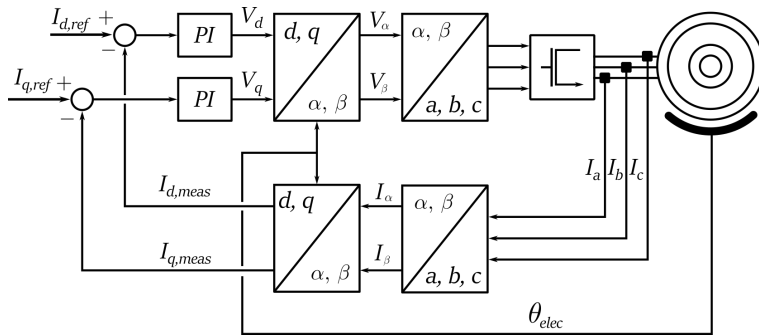


Figure 3.26: Field Oriented Control Blocks Diagram

To achieve the FOC we start by transforming the current signals that we acquire from the current sensors using the Clarke Transformation, which converts the three current phasors of the motor into two equivalent currents located on the α and β axis:

$$\begin{bmatrix} i_\alpha \\ i_\beta \end{bmatrix} = \frac{2}{3} \begin{bmatrix} 1 & -\frac{1}{2} & -\frac{1}{2} \\ 0 & \frac{\sqrt{3}}{2} & -\frac{\sqrt{3}}{2} \end{bmatrix} \begin{bmatrix} i_a \\ i_b \\ i_c \end{bmatrix}$$

After this, in order to obtain I_d and I_q , which don't change in function of the angular position of the rotor θ , we apply the Park Transformation, which converts the currents i_α and i_β into two currents that are mounted into an axis that rotates with the same angle as the rotor:

$$\begin{bmatrix} I_d \\ I_q \end{bmatrix} = \begin{bmatrix} \cos \theta & \sin \theta \\ -\sin \theta & \cos \theta \end{bmatrix} \begin{bmatrix} i_\alpha \\ i_\beta \end{bmatrix}$$

We can compare these two currents, I_q and I_d , with the reference currents $I_{q,ref}$ and $I_{d,ref}$, generating error signals ε_q and ε_d that pass

through PI controllers in order to generate two voltage values V_q and V_d , which can be transformed into sinusoidal voltages v_a , v_b and v_c .

To obtain these voltage values, we apply the Inverse Park transform to the quadrature and direct voltages V_q and V_d :

$$\begin{bmatrix} v_\alpha \\ v_\beta \end{bmatrix} = \begin{bmatrix} \cos \theta & -\sin \theta \\ \sin \theta & \cos \theta \end{bmatrix} \begin{bmatrix} V_d \\ V_q \end{bmatrix}$$

and then, the Inverse Clarke Transform:

$$\begin{bmatrix} v_a \\ v_b \\ v_c \end{bmatrix} = \frac{3}{2} \begin{bmatrix} \frac{2}{3} & 0 \\ -\frac{1}{3} & \frac{\sqrt{3}}{3} \\ -\frac{1}{3} & -\frac{\sqrt{3}}{3} \end{bmatrix} \begin{bmatrix} v_\alpha \\ v_\beta \end{bmatrix}$$

Finally, we apply these v_a , v_b and v_c values to the inverter applying the sinusoidal drive method explained in 3.4.2.

3.5.4 Speed Control with Field Oriented Control

Since by applying the FOC method to PMAC motors we can achieve a good current control, we can therefore control the torque produced by the motor with the same performance. Due to this, the best option to control the speed of a PMAC motor is to close a speed loop around the FOC loop as the one shown in Figure 3.27.

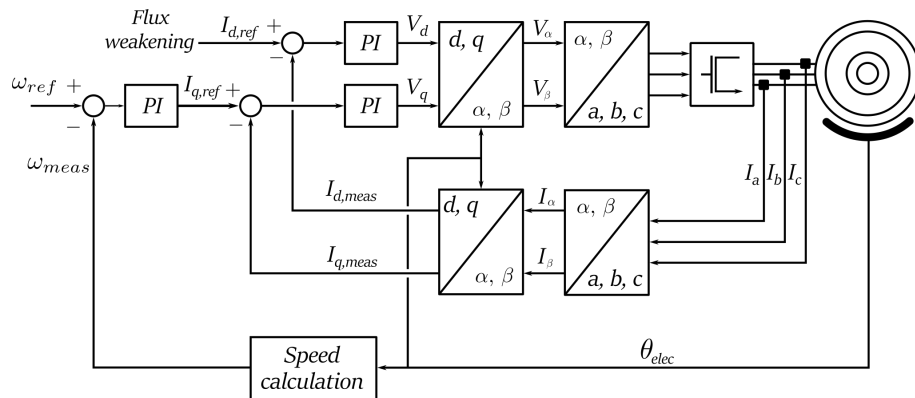


Figure 3.27: Field Oriented Control Applied in Speed Control

4

STUDY CASE

This thesis was proposed as part of a robotic agriculture project which consists in the development of a mobile manipulator for agricultural applications called ROBI'. In this chapter we will explain the main characteristics of the project, focusing in the electronic architecture and in the systems that should be controlled by the motor driver developed in this thesis. The information for this chapter was obtained from Bascetta, Baur, and Gruosso "ROBI': A Prototype Mobile Manipulator for Agricultural Applications" 2017 and from Bascetta, Baur, and Gruosso "Electrical Unmanned Vehicle Architecture for precision farming applications" 2017.

4.1 ROBI

ROBI' is a mobile manipulator for agricultural applications. The development of this project has the objective of becoming a platform for research, development and testing of different perception and control algorithms that could help in agriculture and in similar applications. The robot was designed following low-cost, low-weight, simplicity, flexibility and modularity requirements, in order to allow an easy implementation of the work developed as part of this project.



Figure 4.1: ROBI' Basic Configuration

Table 4.1: HUB10GL in-wheel motor main characteristics

Motor mass	3.5 kg
Motor and tire mass	5.7 kg
Tire diameter	254 mm
Power	500 W
Voltage	36 V
Maximum speed	1350 RPM
Phase-to-phase resistance	160 mΩ
Phase-to-phase inductance	0.76 mH
Pole Pairs	10
K_E	0.36 V/(rad/s)
K_T	0.4506 Nm/A

4.2 IN-WHEEL MOTORS

One of the most important components of ROBI' for this thesis is the in-wheel motor system used as motor drive. As mentioned in the introduction, in-wheel motors have the advantage that there is no need for an external power transmission mechanism, due to the fact that the motor is embedded into the wheel. This also reduces the space needed for the motor drive system, as well as the weight of the robot, increasing the payload capacity of the electric motor.

It is also interesting to mention that this configuration of the drive system allows the control of each one of the wheels of the robot independently, which allows the implementation of different control methods for this robot, like skid steering, which relies on the slip effect of the wheels in the terrain and requires a good control of the torque and the speed of each one of the motors.

The in-wheel motor installed in the robot is a PMSC motor and its main characteristics are mentioned in Table 4.1.

In order to take advantage of the sinusoidal distribution of the windings of this motor, an absolute angular position sensor was installed in the drive system in order to be able to apply a FOC loop. The sensor was attached to the wheel by means of a toothed pulley system in order to keep it away from the ground, as seen in Figure 4.2.

The angular position sensor is an Orbis magnetic encoder, manufactured by RLS. This is a magnetic encoder which works by reading the orientation of the magnetic field of a permanent magnet attached to a shaft, as explained in 3.3.2. The encoder has a resolution of 14 bits with a sensitivity of $\pm 0.3^\circ$ and transmits the angular position information through a modified Serial Peripheral Interface (SPI) called



Figure 4.2: Encoder transmission configuration

Table 4.2: Battery main characteristics

Manufacturer	FIAM
Model	FGC22703
Type	Sealed lead acid
Voltage	12 V
Capacity	27 Ah

Synchronous Serial Interface (SSI), which sends the 24 bits in slave write-only mode through an RS422 transceiver.

In this case, the shaft of the sensor is not the shaft of the rotor, but it's the shaft of the pulley system. This transmission system has a 4.6 size ratio due to the space constraints of the system. This motor includes three Hall effect sensors, even if it's a PMSM motor, as mentioned in 3.3.2.

4.3 POWER ARCHITECTURE

Another important aspect for the development of this work is the power supply. In the case of ROBI', the power supply consists on three 12V lead acid deep-cycle batteries connected in series to provide 36V to the different components of the robot.

4.4 ELECTRONIC ARCHITECTURE

It is important to understand the expected electronic architecture in order to consider the peripherals that the microcontroller has to include to communicate with the rest of the systems inside the robot.

The electronic architecture of ROBI' was designed to be similar to an automotive Electronic Control Unit (ECU) based system. In this

architectures, all the ECUs interact with each other through a communication bus called Controller Area Network (CAN).

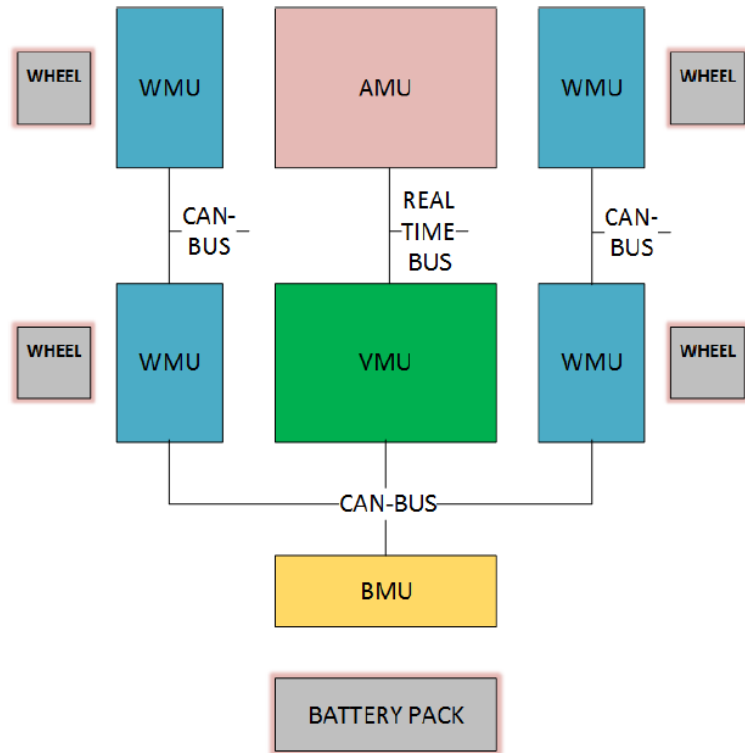


Figure 4.3: ECUs architecture: functional block diagram

As it can be seen in Figure 4.3, the ECUs network consists on four units: Wheel Management Unit (WMU), Battery Management Unit (BMU), Vehicle Management Unit (VMU) and Arm Management Unit (AMU). The one that is being developed here is the WMU, and it will be described in the following chapters.

5

PROJECT DEVELOPMENT

All the theory explained in Chapter 3 and the details of the study case presented in Chapter 4 lead us to the definition of the requirements for the implementation of the motor driver needed by the ROBI' project. This driver, defined as the WMU in Chapter 4, should be able to apply both driving techniques, trapezoidal and sinusoidal, and to execute different motor control methods for the PMSM in-wheel motors. The driving and control methods should be selected by future developers, depending on the application and on the algorithm needed for the control of the overall displacement of ROBI'.

This chapter is divided into three sections: the first section contains a description of the hardware implementation of the driver; the second section explains the implementation of the driving techniques and control methods through embedded software; the last section describes the setup mounted to test the driving capabilities of the WMU developed.

5.1 HARDWARE

The WMU's electronic circuit is based on an open architecture proposed by Texas Instruments (TI) to be implemented together with the use of their Integrated Circuit (IC) MOSFET inverter driver DRV8302. This architecture was implemented in a project developed by the Swedish engineer Benjamin Vedder called VESC, which consists in the design of an Electronic Speed Controller (ESC), its PCB layout design and the implementation of the source code used to drive a BLDC motor (Vedder, 2015). The hardware design of the VESC board was not modified for this thesis in order to identify, after the implementation and the testing of the motor control algorithms, what could be changed to obtain a better performance from the in-wheel motors mounted on ROBI'.

5.1.1 *VESC Board*

The VESC board was conceived and designed to be used as an ESC in electric skateboards with the intention to create one of the best ESCs available. Since it was planned to be used in a skateboard, it has a small form-factor and it can be used for different applications with similar power demand. The hardware can also be modified by changing specific components to drive motors with higher power demand or by modifying the PCB layout design following the schematic de-

sign. The original schematic files can be found attached in Appendix A for reference.

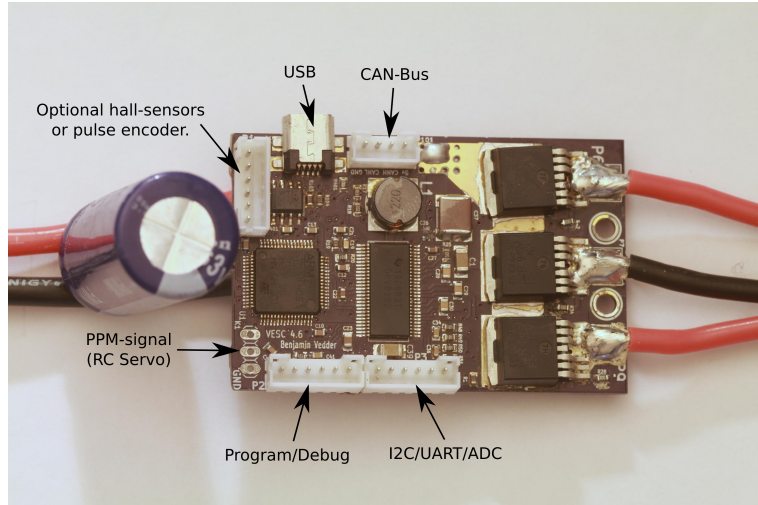


Figure 5.1: Front Side of the VESC Board. The three wires at soldered at the right edge of the board are connected to the three phases of the brushless motor (Vedder, 2015).

The PCB provided as part of the VESC project is a four-layer, $40\text{mm} \times 60\text{mm}$, FR-4 board, with pads for components on the both external layers. The use of both external layers to place components and the four layers to interconnect the circuits allows the board to keep a small form factor.

The board different functional components of the board and their considerations regarding the implementation of the WMU will be explained in this section.

5.1.2 Power Supply Input

The power is supplied into the board by means 2 wires soldered into large pads placed close to the three-phase inverter nodes V_SUPPLY and GND . V_SUPPLY and GND are the positive and negative nodes of the power supply source respectively. The power is supplied from a power regulator for static applications or from a battery for mobile applications, like in the case of ROBI'. It is also specified in the schematics that there should be a bulk capacitor connected in parallel to the power supply port.

5.1.2.1 Power Supply Range

The voltage range of the VESC board is defined by the MOSFET driver IC *DRV8302*, which specifies an operating supply voltage range from 8V to 60V, but allows a maximum voltage supply up to 65V ???. All the other components of the board, mainly capacitors and power MOSFETs, must be selected according to this voltage range.

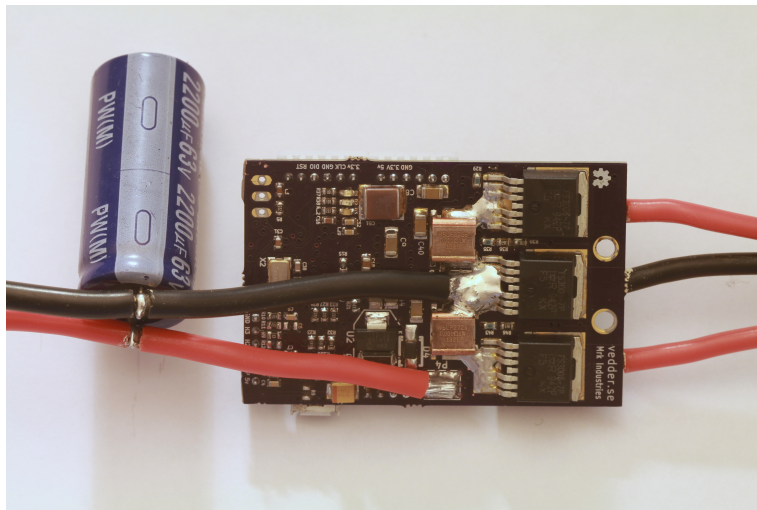


Figure 5.2: Back Side of the VESC board. The red and black wires are the power supply input V_{SUPPLY} and GND respectively.

Table 5.1: VESC Board Operating Ranges

Input voltage	8 to 60V
Maximum output current	50A
Peak output current	240A

The current range of the board is limited by the MOSFETs current limit and by the width of the traces in the PCB. These maximum values will be addressed later in the section dedicated to the MOSFET inverter used in the board.

5.1.2.2 Bulk Electrolytic Capacitor

It is important to place a bulk capacitance with an appropriate capacitance value and voltage range in parallel to the input of the power supply of a motor drive system. The main objective of a bulk capacitance is to control the voltage deviation at the input of a system when the converter is responding to an output load transient, meaning that if there is a load increase and the power supply is not able to provide the current instantaneously for the motor, the current must be provided by the bulk capacitor. The higher the capacitance at the input of the system, the lower the deviation at the load, but this comes at a cost of price and space, since the capacitance value of a capacitor is proportional to the size of its parallel plates. The value of the input bulk capacitor is determined mainly by the following factors:

1. The largest amount of current required by the motor
2. The capacitance of the power supply and its ability to source current

3. The parasitic inductance between the power supply and the motor
4. The acceptable voltage ripple
5. The type of motor

The datasheet of a motor driver should generally provide a recommended value for the bulk capacitor, but it is necessary to calculate and test the value to determine if it's appropriate. The voltage rating of a bulk capacitor must be higher than the value of the power supply to provide a margin for cases in which the motor transfers energy to the supply, which would increase its voltage and would damage a capacitor with a smaller value than the resulting voltage. We can calculate the capacitance value by using the following formula (Arrigo, 2006):

$$C = \frac{1.21 \cdot I_{tr}^2 \cdot L}{\Delta V^2} \quad (5.1)$$

Since there is no filtering inductance in the system, we can consider a stray inductance of $50nH$ in the calculation. If we consider a transient current I_{tr} equal to the rated current of the in-wheel motor, $14A$ approximately, and a voltage ripple of $100mV$, we obtain a capacitance value of $1185.8\mu F$ for the bulk capacitance. Looking for available capacitor values, we increased the value of the capacitor to $2200\mu F$ and, considering the maximum input voltage value of the motors, the common practice is to double that value, so we defined a voltage range of $75V$, which is a typical value for a commercially available capacitor.

It is important to note that since the value of this capacitance is large, also its size will be large, therefore it's important to consider its dimensions to setup a mechanically stable position for such capacitance with aims of avoiding hardware malfunction.

5.1.2.3 Power Supply Wiring

The strategy of soldering the wires directly to the pads in the PCB helps reduce the size and cost of the board since it avoids the use of large power traces in that would be needed if a regular receptacle connector was to be used.

Anyway, the practice of soldering a wire directly to a PCB is discouraged mainly in circuits that will be mounted in a system designed to be in movement (i.e. automotive or aerospace applications) because the wire used in these applications is made of delicate copper strands which can break easily with movement of the board or of the wires and cause a short circuit or a loose contact, both of which might lead to catastrophic failures , so there is a risk in this board since it

Table 5.2: American Wire Gauge current load ratings in function of the number of cores of the wire (The Engineering ToolBox, 2015)

AWG	D [mm]	Maximum Current Load Ratings [A]					
		1	2 - 3	4 - 6	7 - 24	25 - 42	> 43
16	1.3	15	10	8	7	6	5
14	1.6	24	15	12	10	9	7.5
12	2.1	34	20	16	14	12	10
10	2.6	52	30	24	21	18	15

will be mounted in systems that will be in constant movement (RS Components Ltd., 2012). Since this board was designed this way to reduce space consumption, the trade-off between safety and size was balanced into the size constraints, therefore some cautions must be taken to avoid problems, mainly because these wires carry a considerable amount of current and they pass over many components of the board as seen in Figure 5.2.

The first consideration to be made is the wire gauge and insulation type. The wire gauge is a measurement of the wire diameter, which determines the amount of electric current that a wire can safely carry, as well as its electrical resistance and weight. For this board, it is suggested to use short wires to avoid a large voltage drop and to ease the handling of such wire until it reaches the output of the enclosure that will protect the circuit.

The second consideration regarding the wire selection is the insulation material. Since the current passing through the copper also implies power consumption due to the resistance of the copper, there is heat transfer from the wire to its surroundings. To protect the copper strands from its surroundings and vice versa, wires are covered by an insulating material, which has low thermal and electrical conductivity.

Since the heat exchange calculation of the wire would require many assumptions, it's a normal practice to select the type of wire using tables that consider the temperature rise in the wire according to different currents and lengths. In the case of the PMSM motor used in ROBI', the maximum rated current would be approximately 14A, which would lead us to select a wire with a diameter between 2.1mm and 2.6mm, based on Table 5.2. This selection would depend on the number of cores from which the wire is constructed: the bigger the amount of cores, the more flexible the wire is, but also the diameter becomes larger.

Table 5.3: IRFS7530-7PPbF Absolute Maximum Rating

Continuous drain current	240A
Maximum power dissipation (25°)	375W
Linear derating factor	2.5W/°C
Drain-to-Source breakdown voltage	60V
Drain-to-Source on-resistance	1.5mΩ

5.1.3 Power MOSFET Three-Phase Inverter

The three-phase inverter used in the VESC board is based on the power MOSFET IRFS7530-7PPbF, manufactured by the semiconductor company International Rectifier. The schematic design of the inverter can be seen in Figure A.2 in Appendix A. The PMAC motor is connected to the board by soldering its phase terminals directly to the node pads in the middle of each branch of the inverter, which is located at the bottom edge of the board, as seen in Figure 5.1.

This MOSFET is based on the HEXFET Power MOSFET technology, which is a Vertical Double-diffused MOS transistor (VDMOS) with hexagonal elementary cells in parallel which maximizes the W/L ratio of the transistor, providing a low on-resistance value $R_{DS(ON)}$ (Ghioni, 2016).

It is important to note that the maximum power dissipation implies a junction temperature of 25°C, which means that the heat of the MOSFET package should be dissipated by a heat sink, which is not implemented nor considered in the VESC board. If the heat is not dissipated from the transistors, the power dissipation capacity of the transistor decreases following the linear derating factor.

5.1.3.1 Switching Times

As mentioned in 3.3.1, power MOSFETs have large parasitic capacitances that need to be charged in order to allow the activation of the transistor. This behaviour also affects the switching time, which is the time that a transistor takes to turn on and turn off completely.

The switching time of a transistor is therefore defined by the capability of the driving circuit to provide current to charge the parasitic capacitances in the gate and to draw current from them.

To determine the switching time of a MOSFET is necessary to analyse the driving circuit and the parasitic capacitances of the transistor. The information regarding the switching time of the transistor is normally available in the device datasheet.

It is important to notice also the conditions on which the electrical characteristics of the device were obtained. In this case, it is stated in the datasheet that the transistor had a gate resistance R_G of 2.7Ω,

Table 5.4: IRFS7530-7PPbF Dynamic Electrical Characteristics

Total gate charge	236 nC
Gate-to-Source charge	62 nC
Gate-to-Drain charge	73 nC
Turn-On delay time	24 ns
Rise time	102 ns
Turn-Off delay time	168 ns
Fall time	79 ns
Input capacitance	12.9 nF

a gate-source voltage V_{GS} of 10V, a V_{DC} equal to 30V and the current flowing through the device was 100A.

In the case of the IRFS7530-7PPbF, we can calculate that the minimum period of time to turn on and turn off the transistor is 373ns, which is equal to the sum of the turn-on delay time, rise time, turn-off delay time and fall time (Table 5.4). The inverse of the minimum switching period defines the maximum switching frequency of the transistor $f_{switch,max}$ which is equal to 2.68MHz. Since the time constant $\tau = L/R$ of the motor is equal to 4.75ms, which is much larger than 373ns, we can see that the switching frequency of the IRFS7530-7PPbF doesn't represent a limitation for implementing the driving methods explained previously. This switching frequency limitation should be considered instead at the moment of the implementation of the PWM signal generation.

If we look at the MOSFETs on the inverter in the VESC board, we can see that there is a 4.7Ω resistance connected between the driver and the gate, which might change the driving current of the device. We must also keep an eye on the V_{GS} value applied by the MOSFET driver not to be lower than 10V.

5.1.4 MOSFET Driver

The central component in the VESC board, around which the rest of the circuit was designed, is the IC DRV8302, a brushless motor inverter driver manufactured by TI. The complete functional block diagram can be found in Appendix B.

The DRV8302 provides three half bridge drivers capable of driving two N-channel MOSFETs each, which solves the need to implement a high-side and a low-side circuitry to turn on each one of the transistors on the inverter, as mentioned in 3.3.1. For this mean, the device provides up to 30mA at an output voltage V_{GS} between 9.5V and 11.5V to drive the transistors, using a bootstrap gate driver architecture with trickle charge circuitry to support a duty cycle of 100%.

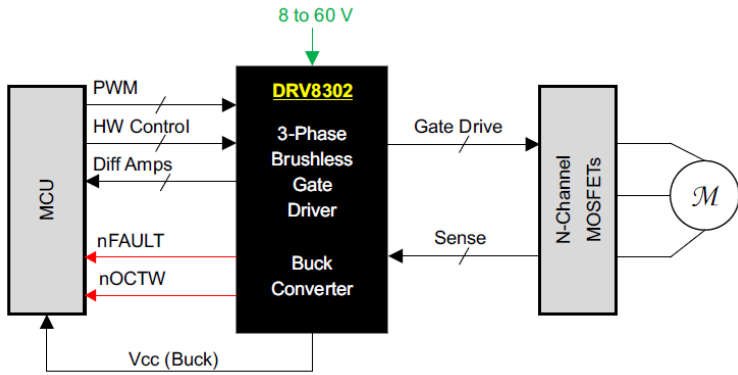


Figure 5.3: DRV8302 Simplified Schematic

5.1.4.1 Operating Range

The *DRV8302* can operate from a single power supply with a wide range from 8V to 60V. This voltage range limits both the minimum operating voltage and the maximum operating voltage of the VESC board. The minimum operating voltage shouldn't be a problem in applications like ROBI', where the power is supplied by battery packs with a voltage larger than 12V, but if V_{DC} is smaller than 8V, the driver won't operate correctly.

It is important to point out that the *DRV8302* also includes an integrated switching mode buck converter with adjustable output and switching frequency, which can provide up to 1.5A. In the case of the VESC board, the logic level voltage V_{DD} is 3.3V, which is obtained by regulating 5V with a Low Drop-Out (LDO) regulator. The 5V are obtained from the integrated buck converter of the *DRV8302*. Due to this, having a large voltage drop on the power supply, which can be caused by a big current transient, might lead to a malfunction of the motor drive system since the power supply of the microcontroller could be interrupted. This is one of the reasons why the bulk capacitance at the input of the power supply is important.

The other problem that might arise is on the other side of the voltage supply range of the device, which is 60V. As mentioned at the end of 3.1.1, it is possible that the motor behaves as a power supply if there is a speed imposed on its rotor. Also, we explained in 3.4.1 that is possible to brake the motor if we direct the current into the power supply. These behaviours lead to the possibility of a voltage increase in the motor terminals equal to the double of the voltage value of the power supply, due to the energy stored in the windings when the motor starts to brake. In the case of ROBI', this voltage might reach up to 72V, which can lead to failure of the *DRV8302*, so we must be careful of this when braking or we must install an electronic circuit which protects the device.

5.1.4.2 Switching Frequency

It is stated in the datasheet of the *DRV8302* that the maximum switching frequency that can be achieved on the MOSFET inverter by using this driver is 200kHz , which depends on a gate charge equal to 25nC . Since the gate charge of the MOSFETs used in the inverter is much larger, we need to calculate the minimum switching period in order to be sure that this value is the same for our case. The minimum switching period is obtained from the following Equations, using the data from the dynamic electrical characteristics of the transistor (Table 5.4) and the gate charge curve of the transistor (Figure 5.4) (Ghioni, 2016):

$$t_{d(ON)} = \frac{Q_{GS}}{I_G} = 2.07\mu\text{s} \quad (5.2)$$

$$t_{rise} = \frac{Q_p}{I_G} = 2.433\mu\text{s} \quad (5.3)$$

$$t_{fall} = \frac{Q_p}{I_G} = \frac{Q_p \cdot R_G}{V_{GS,p}} = 97\text{ns} \quad (5.4)$$

$$t_{d(OFF)} = R_G \cdot C_{iss(MAX)} \ln\left(\frac{V_{GS,MAX}}{V_{GS,p}}\right) = 144.3\text{ns} \quad (5.5)$$

where Q_p is the plateau charge in Figure 5.4, equal to the Gate-to-Drain charge charge, specified in Table 5.4; I_G is the current capacity of the driver, equal to $30mA$; R_G is the gate resistance of the circuit, defined by the gate resistance of the MOSFET, 2.2Ω , in series to the resistance between the driver and the gate, 4.7Ω , obtaining a total R_G equal to 6.9Ω ; V_{driver} is the driver voltage, considered as $10V$; $V_{GS,MAX}$ is equal to the maximum Gate-to-Source voltage in the gate charge curve; $V_{GS,p}$ is the gate-to-source voltage in the plateau of the gate charge curve; and the maximum gate capacitance $C_{iss(MAX)}$ can be calculated as:

$$C_{iss(MAX)} = \left. \frac{dQ}{dV} \right|_{ohmic} = 25\text{nF} \quad (5.6)$$

Since the charge mechanism is defined by the current that can be provided by the driver, the calculation of the turn on and rise time are done considering this current as the limiting parameter. For the turn off and discharge time, the current discharge depends on the voltage on the gate and on the gate resistance.

We can see that the values obtained are much larger than the ones mentioned by the datasheet under the test conditions, therefore, we

calculate a new minimum switching period equal to $4.74\mu s$, which represents a maximum switching frequency of $211kHz$, therefore, we should consider the maximum switching frequency as the one stated by the datasheet of the driver. In any case, this doesn't represent a constraint in the driving of the in-wheel motor, but it should be taken into account while implementing the PWM signal generation, as mentioned in 5.1.3.1.

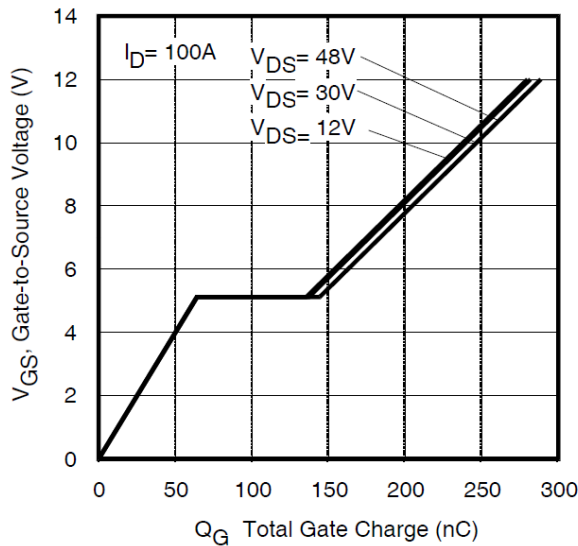


Figure 5.4: Gate Charge vs. Gate-to-Source Voltage

5.1.4.3 Driver Protection

The configuration from which the three-phase inverter is implemented has a dangerous failure condition called "shoot-through". This is a characteristic of any circuit based on a "half-bridge" configuration and it can occur when the two transistors in one branch of the inverter are enabled, which would create a low resistance path ($2R_{DS(ON)}$) for the current from V_{DC} to $0V$, which would practically be a short circuit that can be catastrophic. In order to prevent this failure condition, the DRV8302 uses an automatic hand shaking when the high side or low side MOSFET is switching, meaning that, if one of the transistors of the bridge is enabled, the other transistor can't be enabled.

The DRV8302 provides overcurrent, overtemperature, and undervoltage protection. The overcurrent protection is done by sensing the drain-to-source voltage of the transistor V_{DS} while the transistor is enabled, which is equal to the product of the current flowing through the MOSFET I_D , and the on-resistance $R_{DS(ON)}$ of the same. This voltage is compared against a trip point, which determines when there is an overcurrent. This trip point is defined by applying a voltage to the OC_{ADJ} pin in the IC using a resistive voltage divider, enabled by the pin $DVDD$. In the case of the VESC, the pin OC_{ADJ} is connected

directly to the pin *DVDD*, which disables the overcurrent protection feature of the device. Also due to this, the pin *nOCTW* which informs about an overcurrent fault is not connected to the microcontroller.

The undervoltage protection of the *DRV8302* consists on driving low the gate drive outputs of the inverter whenever the voltage of the pins *PVDD* and *GVDD* are below their undervoltage thresholds (6V and 8V respectively). *GVDD* is the voltage of the gate driver regulator and is usually 11V. The device has two *PVDD* inputs: *PVDD1* and *PVDD2*. *PVDD1* is the power supply of the gate driving circuit, while *PVDD2* is the power supply of the integrated buck converter. In the case of the VESC board, both power supplies are connected to the same node *V_SUPPLY*. An undervoltage brownout of $13\mu s$ in *PVDD1* can cause the device to become unresponsive to external inputs until the device is reseted. This behaviour was present while doing the tests of the board when the motor drive demanded a current larger than the limit of the power supply, which caused a voltage drop and the device became unresponsive, even if the buck converter was still working. An undervoltage error flag is provided by the device through the pin *nFault*.

The datasheet states that there is also an overvoltage protection, which turns off the date driver and the charge pump in case than the voltage *GVDD* reaches 16V. This voltage is generated from an internal regulator, which delivers the voltage to drive the gates of the MOSFETs of the inverter. Therefore, an overvoltage on this pin means that there is a hardware problem and the board must be inspected.

The overtemperature protection of the device works in two levels. The first level delivers an overtemperature warning through the pin *nOCTW* (which is disconnected in the VESC board). The second level of the protection shuts down the gate driver and the charge pump until the temperature on the driver decreases and the *EN_GATE* pin is reset.

The *EN_GATE* pin enables the operation of the inverter gate driver. If the *EN_GATE* pin is low, the driver won't respond to the driving signals applied on the switching signal input pins *INH_X* and *INL_X*.

One of the main features of this MOSFET inverter driver is that there is a built-in buck converter. This allows the *DRV8302* to provide a power supply for the microcontroller and other lower voltage components. The buck converter is based on the TI's *TPS54160* step-down converter, which can provide up to 1.5A. The output voltage of this converter is defined by the external components connected to the pins dedicated to this, which close the feedback loop. In the case of the VESC board, the converter is configured to provide 5V, which can be used to supply power to different low voltage devices. From this 5V power supply, a 3.3V LDO voltage regulator is connected to supply power for the microcontroller, as mentioned before.

In order to sense the current flowing through the MOSFETs of the inverter, and therefore, in the windings of the motor, the *DRV8302* includes two current shunt amplifiers. The working principle of the shunt resistance voltage drop amplifier is explained in 3.3.3. In the case of the *DRV8302*, the voltage drop is measured in two differential amplifiers from which we can select the gain. The approach of using only two shunt resistances, instead of three, in order to read the current flowing through all the phases of the motor, is based on the fact that the currents on the motor behave as in a nodal analysis, so if we apply the Kirchhoff's Current Law (KCL) in the center of the motor, we obtain that:

$$I_{phase1} + I_{phase2} + I_{phase3} = 0 \quad (5.7)$$

therefore, by measuring the current in, for example, phase 1 and phase 3, like in the case of the VESC board, we can calculate the current flowing through phase 2 as:

$$I_{phase2} = -(I_{phase1} + I_{phase3}) \quad (5.8)$$

The voltage obtained as the result of the conversion (Equation 5.9) presents an off-set in order to be able to read currents bidirectionally. This offset is set by applying the reference voltage V_{REF} in the pin *REF*. In the case of the VESC board, this pin is directly connected to the output of the LDO regulator (3.3V).

$$V_O = \frac{V_{REF}}{2} - G \cdot (SN_X - SP_X) \quad (5.9)$$

From 5.9 we can therefore calculate the phase currents I_{phase1} and I_{phase3} as:

$$I_{phase} = \frac{SN_X - SP_X}{R_{shunt}} = \frac{V_O - \frac{V_{REF}}{2}}{R_{shunt}G} \quad (5.10)$$

where $SN_X - SP_X$ is the voltage drop across the shunt resistance. In the case of the VESC board, the gain is hardwired to 10 and the value of the shunt resistance R_{shunt} is 0.001Ω .

5.1.5 Microcontroller Unit

The processor for which this board was designed is the STM32F405rg: a 64-pin IC microcontroller of the STMicroelectronics family of 32-bit devices with an ARM Cortex-M4 CPU and a core operating frequency up to 168 MHz. The Cortex-M4 core features a Floating Point Unit (FPU) single precision which supports all ARM single-precision

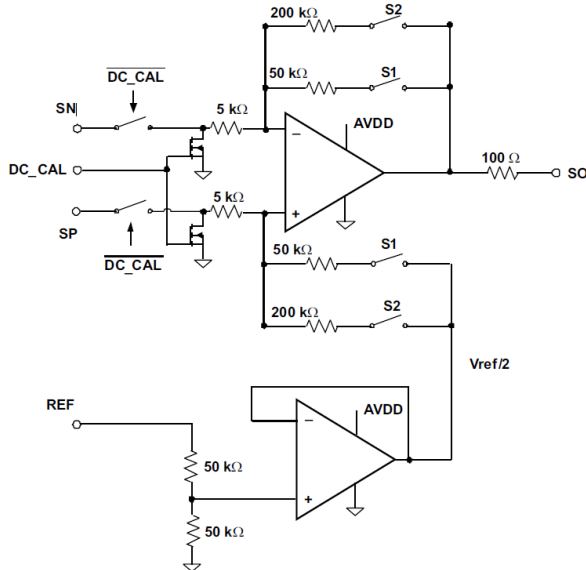


Figure 5.5: Current Shunt Amplifier Simplified Block Diagram

data-processing instructions and data types. It also implements a full set of Digital Signal Processor (DSP) instructions, which makes it ideal for the signal processing required to drive PMAC motors. This microcontroller also includes three 12-bit ADCs and supports USART, I₂C, SPI, USB and CAN communication interfaces, improving the versatility of the WMU. The memory of the microcontroller consists in 1024 kB of Flash memory and 192 kB of SRAM memory.

The microcontroller is programmed by uploading a *.hex* file into its memory by using the programming tool *ST – LinkV2*.

5.1.6 Peripherals

The VESC board has many peripheral circuits in order to improve its versatility. In the case of ROBI', these peripherals are indispensable for the implementation of the WMU.

5.1.6.1 USB

The board has a micro-Universal Serial Bus (USB) port, which is connected to the corresponding pins D+ and D- of the microcontroller. This Universal Serial Bus (USB) port can be used as a normal USB device, which requires the implementation of the USB drivers and of a compatible program developed to communicate through the port. It can also be used as a USB-Serial device, which creates a virtual serial COM port in the computer to which it is connected in order to communicate to it through a serial terminal, like PuTTY. STMicroelectronics provides drivers to implement both uses of the USB port.

The USB port was not used in this project since the implementation of a compatible USB software would require much time. Also, the USB-Serial library of STMicroelectronics was not used since it presented many problems in the development stage.

5.1.6.2 CAN

The Controller Area Network (CAN) is a communication protocol developed by the German company Robert Bosch GmbH, based on a bus topology for the transmission of messages in a distributed environment, considering a solution to the communication management between many ECUs (Lawrenz and Obermöller, 2011). This communication protocol is the most used one in automotive applications and it also can be found in many other applications with a multi-drop bus architecture. In the case of ROBI', the idea is to implement the communication between its ECUs using CAN.

The microcontroller includes hardware support for CAN communications. The physical layer is controlled by the IC CAN transceiver SN65HVD232, by acTI. The implemented circuit can be found in Figure A.4 in Appendix A.

The CAN bus drivers for this project were provided by the Skyward Experimental Rocketry project team, and its implementation is yet to be tested.

5.1.6.3 Hall Encoder

The signal of the Hall effect sensors embedded in the PMAC motor connected to the board is conditioned by the circuit that can be found in Figure A.5 in Appendix A. This circuits connects the output of the Hall effect sensors to a pull-up resistor since Hall effect sensors might have an open-collector configuration.

5.1.6.4 Communication Interfaces

Other types of communication protocols can be implemented into the board, like Universal Asynchronous Receiver-Transmitter (UART), Serial Peripheral Interface (SPI) and Inter-Integrated Circuits (I₂C), by means of connecting the respective nodes of the board through the pins available in the connector P3, which can be located in the schematic overview (Figure A.1, Appendix A).

5.1.6.5 Temperature Sensors

The board considers the use of two temperature sensors, one connected externally and one embedded on the same board.

The external temperature sensor can be selected in any technology as long as the output is inside the ranges of the ADC of the microcontroller, which will be explained later.

The internal temperature sensor is a Negative Temperature Coefficient (NTC) thermistor. A thermistor is a type of resistor whose resistance value changes with a larger dependence on temperature than normal resistors (Micro-Chip Technologies, 2010). The thermistor is used as part of a voltage divider, with the output connected to an ADC port of the microcontroller (Figure A.3, Appendix A).

The temperature of the board can be calculated based on the voltage drop on the thermistor due the change of its resistance in function of its calculated dependence on temperature:

$$R = R_0 \exp(B - (\frac{1}{T_0} - \frac{1}{T})) \quad (5.11)$$

which can be solved for the temperature as:

$$T = \frac{B}{\ln(R/r_\infty)} \quad (5.12)$$

and since the value of the other resistance in the voltage divider is equal to the rated resistance R_0 of the thermistor, we can calculate the temperature of the thermistor by measuring the output voltage of the voltage divider as:

$$T = \frac{B}{T_0} - \frac{B}{\ln(V_{temp} - 1)} \quad (5.13)$$

5.1.6.6 Indicator LEDs

There are three LED indicators that can be used to visually determine the status of the processes running in the board. Two of these LEDs can be controlled by the microcontroller. The other LED is connected directly to the 3.3V voltage supply in order to see if the power supply is connected into the board and the microcontroller is energised.

5.1.6.7 RC Servomotor Port

There is a port provided to connect an RC servomotor to the board, which is connected to a free PWM port on the microcontroller. This port can also be used for other purposes. For example, in this project, the port was used in order to visualize signals with the aid of an oscilloscope.

5.1.7 Angular Position Sensor

As mentioned in Chapter 4, the angular position sensor of the rotor is determined by the Orbis absolute rotation magnetic encoder.

Since the encoder uses the SSI interface to communicate with other devices, a signal conditioning circuit was needed because the VESC board doesn't support the physical layer of this communication protocol. In order to solve this problem, an RS422 transceiver circuit (Figure 5.6) was connected between the Orbis sensor and the board. The transceiver purpose is to manage the physical layer interconnection between the SSI interface of the Orbis encoder and the SPI interface available in the board. The clock signal, which defines the transmission frequency, was connected from the port *SCK* of the board to the *D* input of the transceiver, which converts it into a differential clock signal with output in the ports *Y* and *Z*, which is the type of signal that is read by the SSI protocol. The data input to the board was through the port *MISO*, connected to the output *R* of the transceiver, which converts the differential output signal of the encoder *A* and *B* into a CMOS logic-levels signal.

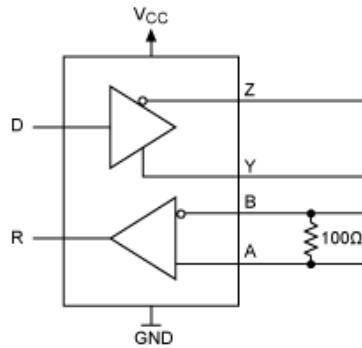


Figure 5.6: RS422 Transceiver Diagram

Another problem encountered with the encoder setup is that the pulley system previously implemented to transfer the angular position information from the in-wheel motor to the Orbis sensor (Figure 4.2) converted the absolute encoder into an incremental encoder due to the 4.6 size ratio between the gears attached to them. This aspect ratio increases the resolution of the angular position obtained but it doesn't provide an absolute value of the actual angular position of the rotor. A solution for this could be to use the Hall effect sensors embedded in the motor to define the actual angle range (6 steps of 60°) and add the difference between two angles provided by the Orbis encoder as an increment to the angle defined by the Hall effect sensors. The problem with the implementation of this solution is that it would be necessary to have the motor already rotating at a known speed to calculate the angular difference to be added to the value defined by the Hall encoder.

The solution to this problem was to change the transmission size ratio from 4.6 to 10. This would provide not the absolute position of

the rotor, but it would provide the absolute position of the electrical position of the rotor, which is explained in Chapter 3:

$$\theta_{electrical} = PP \cdot \theta_{mechanical} \quad (3.19)$$

The system was implemented as a gear transmission instead of a pulley, since the small gear size didn't allow a proper setup using the pulley. This brings the sensor closer to the ground, which was one of the things that was avoided by the pulley system, so further development on this topic should be done.

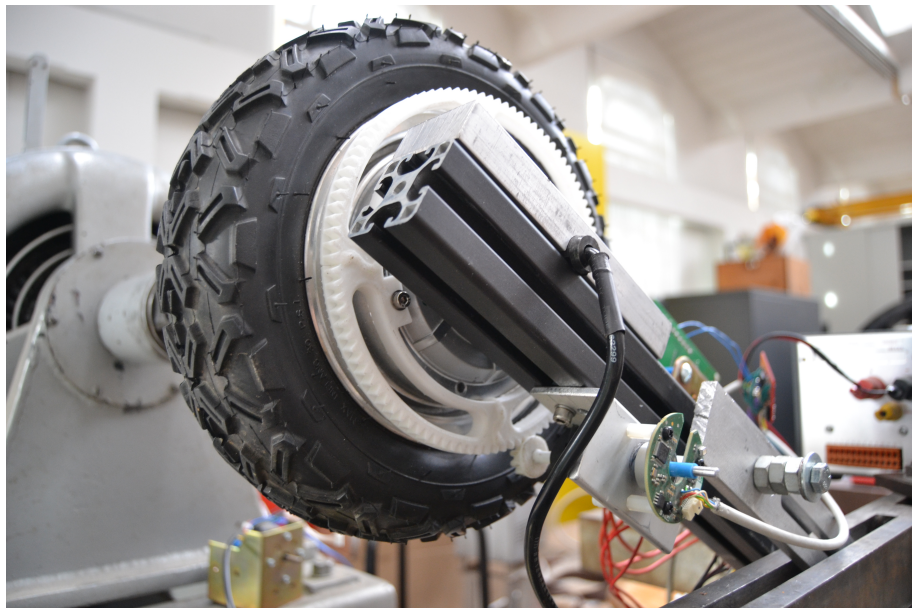


Figure 5.7: New angular position transmission system

5.2 EMBEDDED SOFTWARE

An embedded system is an electronic computing system with a dedicated function within a larger mechanical or electrical system, which might have real-time computing constraints (Heath 2003).

The term "embedded software" is applied to the computer software programmed into the embedded systems, which usually have computing power and memory constraints, like microcontrollers, in order to maintain a lower price, lower power consumption and a higher robustness than a typical computer processor. This software is designed to be programmed only once into the microcontroller, which will execute a sequence of algorithms during its lifetime, unless there is an update needed.

Normally, embedded software is implemented in low level programming languages, like Assembler, C and C++, since these languages provide a wide control over the resources usage in the device.

Embedded software implementation deals also with a topic that is not very usual in higher programming levels: the use of peripheral registers. These registers allow us to use and communicate with the different peripheral components in a microcontroller that interact with physical variables through its pins. For example, to apply a high logic signal into one of the pins of a microcontroller, we must generate a code that will access the register that controls the physical state of that pin and change its value, which would toggle the voltage of such pin from *GND* to *VDD*.

An important characteristic of embedded systems is that it's easier to implement tasks with real-time constraints. A real-time constraint is present when a task must be executed before a well defined deadline or it should start at a given time within a small tolerance range. Real-time systems normally deal with tasks that, in case that they are not executed by a defined time, the results would be physically catastrophic. Like in the case of automotive systems, where the reliability of the car depends completely on the execution time of many of the tasks in the ECUs of the car.

All the algorithms explained in 3.4 are implemented into the motor driver circuit by writing them in embedded code. The inputs to the algorithm are physical variables obtained by means of interpretation of digital signals, analog signals converted into digital signals by means of an Analog-to-Digital Converter (ADC), and communication interfaces, like CAN, SPI or UART. The outputs from the algorithm are mainly analog signals, which are implemented into the motor driver as a PWM signal, which, by applying it to the three-phase inverter which commutes the V_{DC} voltage in the windings of the motor, generates an analog signal.

For the WMU development, we decided not to keep working with the source code developed for the VESC board, since there was no

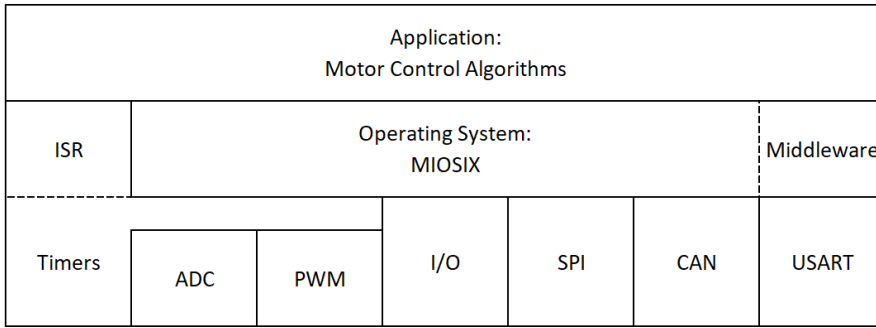


Figure 5.8: Embedded software architecture diagram implemented for the WMU

development regarding FOC, and because the implementation of the driving algorithms in ROBI' might have different considerations regarding the algorithms developed for an electric skateboard.

5.2.1 Operating System

An embedded system can run without an Operating System (OS) if the tasks that are going to be executed on it are simple. For this project we decided to use an existent embedded OS with aims to help us with the implementation of many functions that might need to run in parallel.

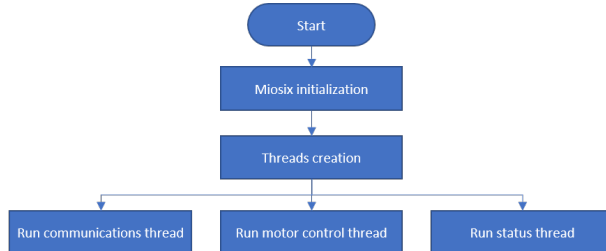


Figure 5.9: Threads Execution Flowchart

The OS chosen to be implemented in this project was Miosix. Miosix is an OS kernel designed to run on 32bit microcontrollers, in active development since 2008. Miosix supports C++, which allows the implementation of embedded software with an objects-oriented architecture. Due to the use of C++, it also supports both a single process and multiple threads application models, which simplifies the implementation of threads for this project (Terraneo, 2014). Miosix was chosen due to its support for the STM32 microcontrollers.

Three threads were implemented, using Miosix multi-thread support, with aims to simplify the implementation of the motor control algorithms, running along with the communication protocol between the WMU and a User Interface (UI). Later on, the implementation of new threads can be done to control CAN communications or other

new functionalities and algorithms. The first thread implemented in this project controls the communication through an Universal Asynchronous Receiver-Transmitter (UART) port, which can be connected to a computer with the implemented UI or to another board with aims to control the reference values of the motor control algorithms or to monitor the different variables of the system. The UART port was configured in the Miosix environment to be used as in a computer based C++ environment, by the use of the `iostream.h` library commands, `cin` and `cout`, in such way that we don't have to worry about configuring the UART related registers. Also, while the system is expecting an input value after using the `cin` command, the thread blocks itself until it receives the expected input. The second thread runs the speed control algorithm. A third thread was implemented only to toggle a LED every second in order to detect if the system is correctly running or if there is any error with the board.

5.2.2 Pulse Width Modulated Signal Generation

The microcontroller family STM32F4 has two timers that are designed to be able to control three-phase motor inverters. For this, the microcontroller is able to generate two complementary PWM signals in three different channels for each timer, intended to command the high-side and the low-side signals of a power inverter driver as the *DRV8302*. These timers are called "advanced timers", and are identified as *TIM1* and *TIM8* (STMicroelectronics NV, 2016). The board connects the PWM outputs from timer *TIM1* to the driver.

A PWM signal is defined by a frequency and a duty cycle, as seen in Chapter 3. The actual implementation of the PWM signal depends on five variables: a counting frequency, a counter, a compare value, a top value and an output signal. The counter normally starts from zero and the compare value should be smaller than the top value, both larger than zero. The output signal is a digital reference signal, which starts as set (high) when the PWM signal is enabled. This output signal is usually the PWM signal generated. When the PWM counter is enabled, the output signal is set and the counter starts increasing its value at the counting frequency until it reaches the compare value, which resets the output signal (low). After this, the counter keeps increasing until it reaches the top value. After the counter reaches the top value, it counts down or starts from zero, depending on the PWM mode.

The PWM mode is defined by the motor drive algorithm. In the case of the trapezoidal drive, since the PWM signal is only applied to one branch at a time, the counter restarts from zero after the top value is reached, switching the output signal immediately after this. This mode is called Edge-Aligned PWM (Figure 5.10).

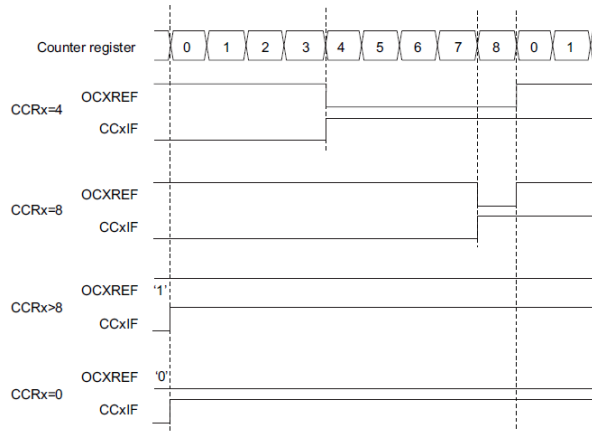


Figure 5.10: Edge-aligned PWM waveforms (ARR=8)

In the case of the sinusoidal drive, since the three branches have PWM signals driving the transistors all the time, in order to reduce the harmonic signals generation due to the commutation between 0V and V_{DC} , a normal solution is to center the PWM signals by, after counting up, counting down from the top value back to zero, resetting the output signal when the counter reaches the compare value. This way, we don't have three branches commutating from 0V to V_{DC} at the same time (Figure 6.16).

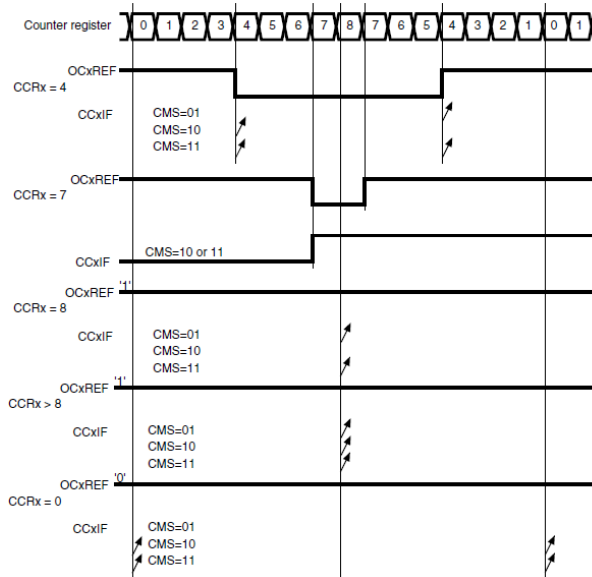


Figure 5.11: Center-aligned PWM waveforms (ARR=8)

The implementation of both motor driving techniques implied also the generation of a signal which is complementary to the reference PWM signal. This complementary signal is obtained by simply inverting to the output PWM signal by modifying one register in the microcontroller. One important aspect to consider regarding this com-

plementary signal, is that it is possible to generate a shoot-through effect in the inverter, even if the driver shouldn't allow it. This shoot-through is generated due to the non-instantaneous activation of the MOSFET gates in the inverter. For example, if the driver disables the gate on the high-side, and then enables the gate on the low side, the gate on the high-side might still be enabled since the capacitance of the gate might still be charged, which creates a shoot-through in the inverter with the duration of the difference between the charge and discharge time of the gates (Maxim Integrated, 2016).

Due to this shoot-through effect due to the gate capacitances, we must generate a dead-time between the main PWM signal and its complementary. This delay is defined as the difference between the activation and deactivation time of the MOSFET equal to $4.26\mu s$. The activation time is the sum of the on-time plus the rise time and the deactivation time is the sum of the fall time plus the off-time, obtained in 5.1.4.2. The dead-time is also configured by modifying the registers of the advanced timer *TIM1*.

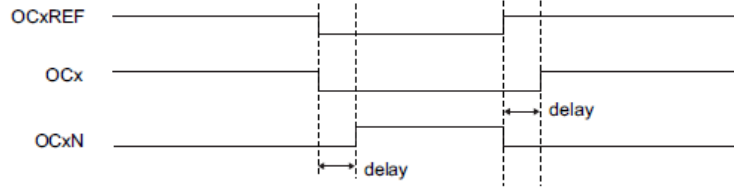


Figure 5.12: Complementary output with dead-time insertion

5.2.3 Analog to Digital Converter

STMicroelectronics' microcontrollers are famous for having one of the most complete ADC systems in the market. For this project, this is a plus, since the input of analog values is necessary to apply some of the motor drive algorithms. The ADC on the *STM32F4* microcontrollers family is 12bit successive approximation analog-to-digital converter.

The most important implementation of the ADC in this project is used for the current measurement to be applied in the current (and torque) control methods. The ADC was configured in this project to read the two available current signals and a signal proportional to V_{DC} at the same time.

In a continuous model, the current measured from the system would be continuously updated to be compared with the reference values and to be introduced into the PI controller to generate an output voltage signal, which would be applied into the inverter. Since we are dealing with digital models, the implementation differs, but we must approximate it as much as possible to the continuous model to obtain a good performance of our system.

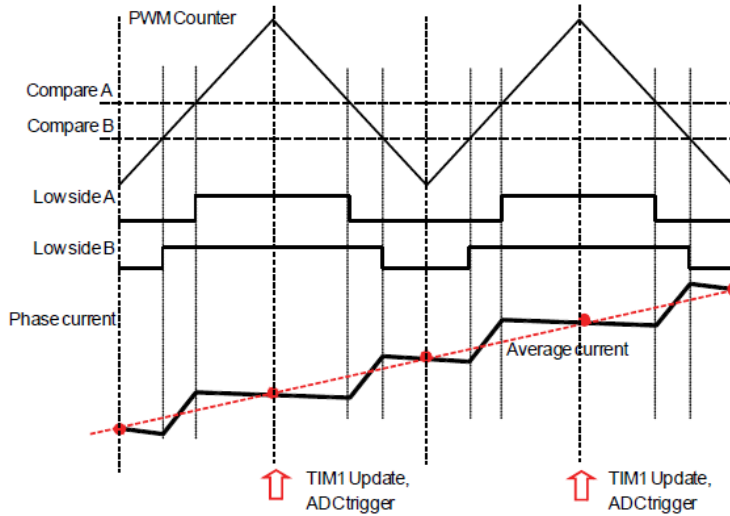


Figure 5.13: Current reading in shunt resistor (STMicroelectronics NV, 2016)

The implementation of the current measurement is explained in Figure 5.13. Based on the windings charge and discharge, which depends on the voltage applied to them, we can obtain the average value of the current flowing through the coil by measuring the current at the middle point of the PWM signal generated to drive the inverter. In order to do this, the ADC was synchronized with the fourth channel of the advanced timer *TIM1*, which doesn't have a physical output, but it generates a reference signal as well as the other three channels that drive the inverter (Figure 5.14).

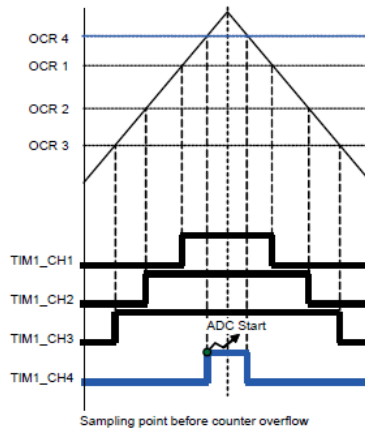


Figure 5.14: ADC and PWM Synchronization

After obtaining with the 12bit ADC the value of the voltage drop in the shunt resistor, which was amplified by the driver *DRV8302*, we

can calculate the current flowing in the branches 1 and 3 by translating the voltage value obtained into an equivalent current:

$$I_{shunt} = \left(\frac{ADC_{Vdrop} \cdot 3.3V}{2^{12}} - \frac{3.3V}{2} \right) \cdot \left(\frac{1}{G \cdot R_{shunt}} \right) \quad (5.14)$$

Another important thing to consider is the possibility of an offset at the output of the *DRV8302* amplifier. The datasheet of the driver specifies that there can be an offset of $\pm 4mV$, which would translate into a phase current of $400mA$, which is not negligible. In the case of the FOC, this current reading offset could create a DC offset in the generated voltage driving signals and this could significantly reduce the performance of the motor drive. Due to this, we need to implement a calibration algorithm in order to suppress this offset. This calibration is implemented to be done every time that the board is initialized, but it might be necessary to be done every time that the board stops driving the motors.

To do the offset calibration of the current measurement, the *DRV8302* provides a pin that disconnects the input of the amplifiers in order to obtain the DC offset value. The algorithm implemented creates an average of ten thousand samples of the offset voltage and then defines a current offset value I_{offset} that should be subtracted everytime that we calculate a current value.

$$I_{shunt} = \left(\frac{ADC_{Vdrop} \cdot 3.3V}{2^{12}} - \frac{3.3V}{2} \right) \cdot \left(\frac{1}{G \cdot R_{shunt}} \right) - I_{offset} \quad (5.15)$$

5.2.4 Algorithms Implementation

The driving algorithms implemented in this thesis for the WMU are two. The first algorithm is the trapezoidal drive, which can be used in an open loop and in a speed control loop. The second one is the sinusoidal drive, which can be used in an open loop, in FOC only controlling the current and in FOC with a speed control loop. These algorithms depend on other algorithms, like the speed calculation and the PI controller.

The trapezoidal and FOC driving algorithms are executed by a call of an Interrupt Service Routine (ISR) of one of the timers at a specific frequency that will be explained later.

The speed loop controllers are PI controllers executed in a thread of the OS every millisecond.

5.2.4.1 Speed Calculation

The speed calculation was made by means of reading the rate of change of the Hall effect sensors value. One clockwise electrical revolution is obtained every time that the Hall effect sensor goes from po-

sition 6 to position 1, while a counter-clockwise electrical revolution is obtained when the Hall effect sensor goes from 1 to 6. Following Equation 3.19 we can calculate the mechanical speed of the in-wheel motor, and with this we can estimate the displacement speed of the whole robot. The speed calculation function is called every time that a driving algorithm is called in order to update the driving speed and the Hall effect sensor values.

5.2.4.2 Continuous Angular Position Definition

As mentioned before, the Orbis angular position encoder is connected to the microcontroller through an RS422 transceiver that manages the interaction between their different physical layers. The SSI interface is practically an SPI interface, with the difference that the SSI implemented in the Orbis sensor uses 24bit messages, while the SPI protocol uses 8bit or 16bit messages.

The message of the encoder is structured as follows: bit23 to bit10 contain the encoder position data; bit9 and bit8 provide the general status of the encoder (data valid or invalid); bit7 to bit0 provide a detailed status about the previous two bits.

The SPI is configured as receive-only master mode, which sends the clock signal to the encoder, expecting a response signal at the same transmission rate. Since the largest message length that the SPI protocol of the microcontroller supports is 16bit, we send only a 16 pulses clock signal, obtaining only the 16 Most Significative Bit (MSB) of the message from the encoder.

To obtain the angular position, we do a bit-wise operation in order to read only the 14 MSB of the message, which contain the angular position. This binary value is translated into radians, to which an angular slip is added (explained in 3.3.2) to define the absolute electrical angular position of the encoder due to the rotor angular position transmission adopted (5.1.7).

It is stated in the datasheet of the encoder that the maximum clock frequency is 500kHz, unless a "Delay First Clock" function is implemented, which would increase the frequency to 2.5MHz, but such function is not explained.

If we consider a clock frequency equal to 500kHz for a 24bit message, the message has a duration of $48\mu s$. After every message we must wait a transfer timeout t_M equal to $16\mu s$ and a pause time t_p equal to $20\mu s$ in order to get a new message from the encoder. These delays add up to the message duration to give a total transmission duration of $84\mu s$, which defines the maximum transmission frequency of the encoder, which is equal to 11.9kHz.

Listing 5.1: Code snippet of the basic PI controller implemented for the project

```

1   error = reference_value - measured_value;
2   output = (error * kp) + integral_error;
3   if (output > MAX_VALUE)
4       output = MAX_VALUE;
5   else if (u < MIN_VALUE)
6       output = MIN_VALUE;
7   else
8       integral_error = integral_error + ((ki * error) * dt);

```

5.2.5 Proportional-Integral Controller

The PI controller algorithm was based on a pseudo-code algorithm proposed by Magnani, Ferretti, and Rocco, 2007. The idea was to prove the ease of implementation of a simple code with a real functionality in a system that can look complex due to all the peripheral configuration and management.

The PI controller implemented compares a measured value with an input value (which can be input through the UI or by another control loop) to generate an error signal and then follows the loop explained in 3.5.1. The difference between this controller and a theoretical one is that, in real cases, the integral part might become very large, and due to this, try to apply a very large control signal, which can damage the system.

For example, in the FOC loop, the PI controller outputs a driving signal depending on a current calculation and its directly applied to the windings. If, by any reason, the in-wheel system gets stuck, the integral part of the system, which increments its value proportionally to the time that has passed and to the error signal, would command the driver to implement an every-time larger driving signal to the coils, which might damage the drive system. To avoid this, the PI algorithm implemented has a saturation condition. If the output of the controller is larger than a `MAX_VALUE`, then the output becomes `MAX_VALUE` and the same happens in with the opposite case using `MIN_VALUE`.

In the speed loop implementation for the trapezoidal drive, the saturation values are 0 and 1, since the duty cycle must be always a number between 0 and 1. In the FOC implementation, the saturation value is a percentage of the bus voltage V_{DC} in order not to generate a large output current. In the speed loop which uses FOC, since the output of the controller is a current which becomes an input to the FOC loop, the saturation value is a maximum current, which applies as a maximum value and as a minimum value by changing its sign. These maximum driving voltage and current in the FOC related al-

gorithms can be implemented as a safety measure in order to avoid drawing too much current from the power source, which might lead to malfunction of the system.

5.2.5.1 Trapezoidal Drive

The trapezoidal drive was implemented by following the six-step sequence with a PWM signal in the high-side transistor, a complementary PWM signal on the low-side transistor of the same branch (positive branch), and enabling a low-side transistor in another branch (negative branch), as explained in 3.4.1.

The algorithm was implemented in a function that is called by the ISC! (ISC!) at a frequency that can be specified by the user. Also the PWM signal is driven at a frequency that can be modified depending on the motor characteristic time τ .

One of the first steps of the algorithm is to compare the current status of the Hall effect sensors with the previous one, in order to avoid modifying registers if it is not needed and to reduce the usage of the microcontroller resources. This condition applies only when the speed is larger than 5rad/s , because, if the motor hasn't started moving, the hall-effect sensors won't change and the algorithm wouldn't be executed.

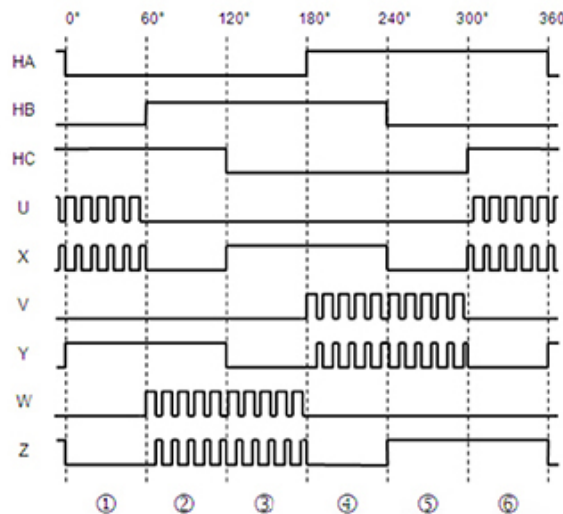


Figure 5.15: Trapezoidal drive signals with complementary PWM in leading branch

5.2.5.2 Field Oriented Control Implementation

The FOC algorithm was implemented following the explanation from 3.5.3, which is a straight sequence. The maximum frequency at which the FOC loop can be called is determined by the maximum frequency of the Orbis encoder, since the angular position of the rotor must be

detected every time that the loop is executed. Due to this, the ISR calls the FOC loop every $100\mu s$.

One important thing to be considered in the case of ROBI' for the implementation of the FOC, is that the system

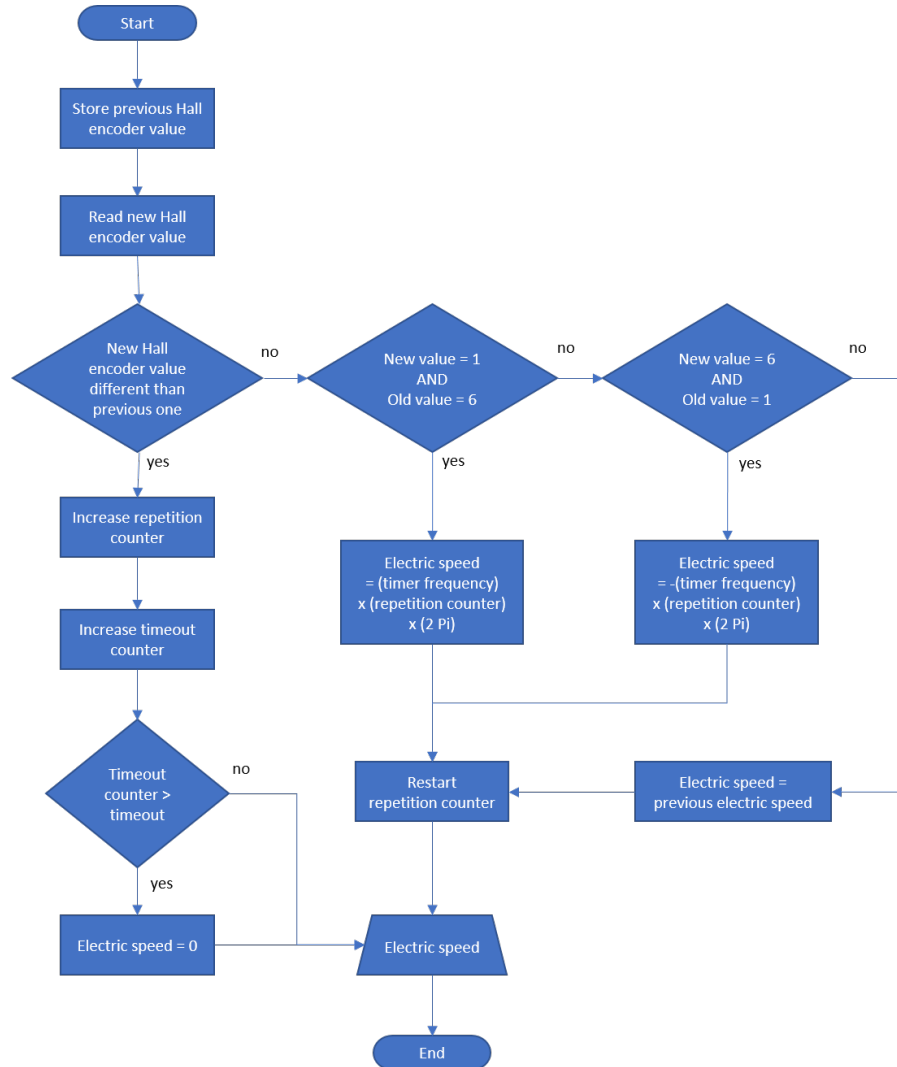


Figure 5.16: Speed Calculation Flowchart

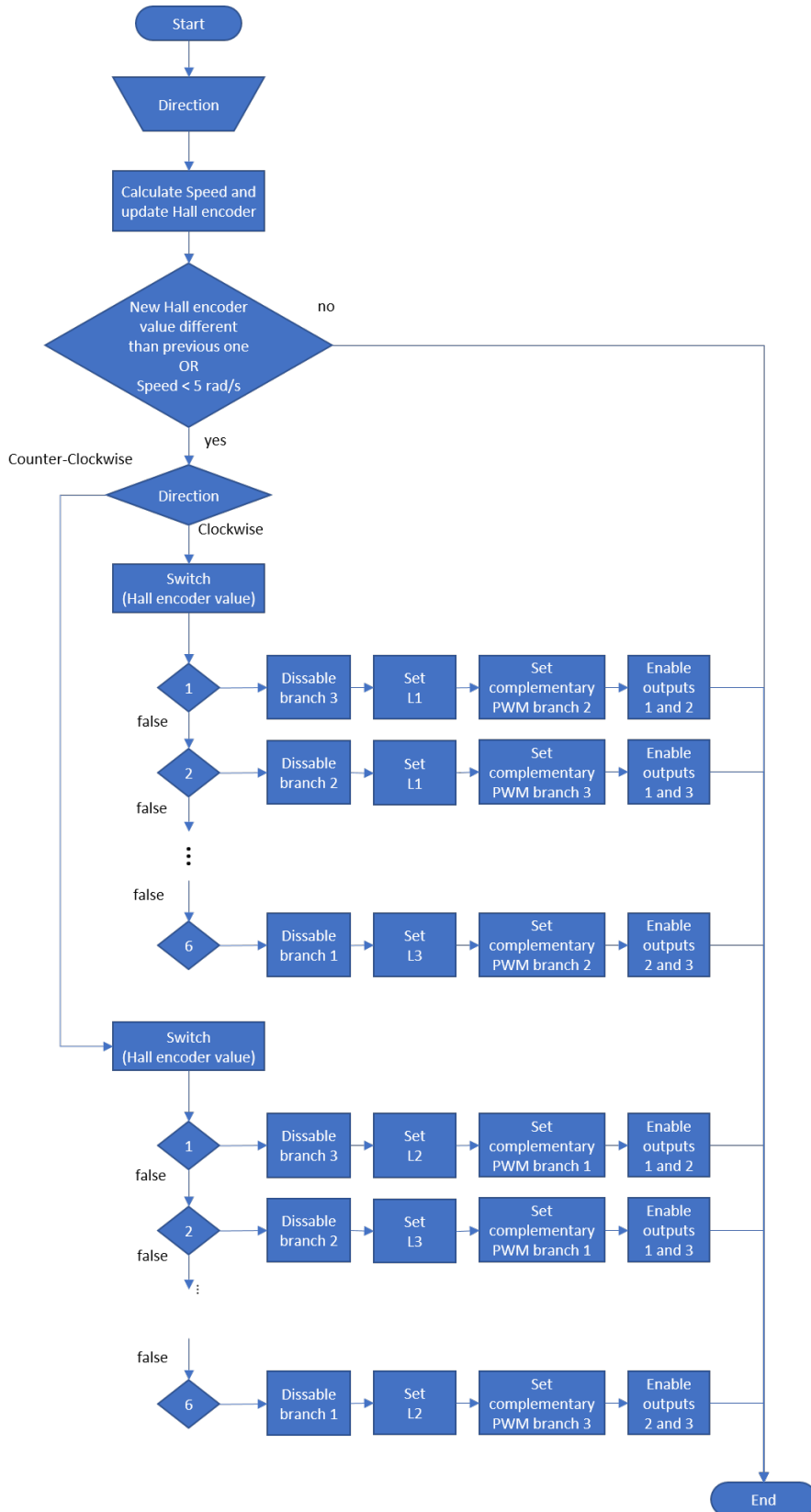


Figure 5.17: Trapezoidal Drive Flowchart

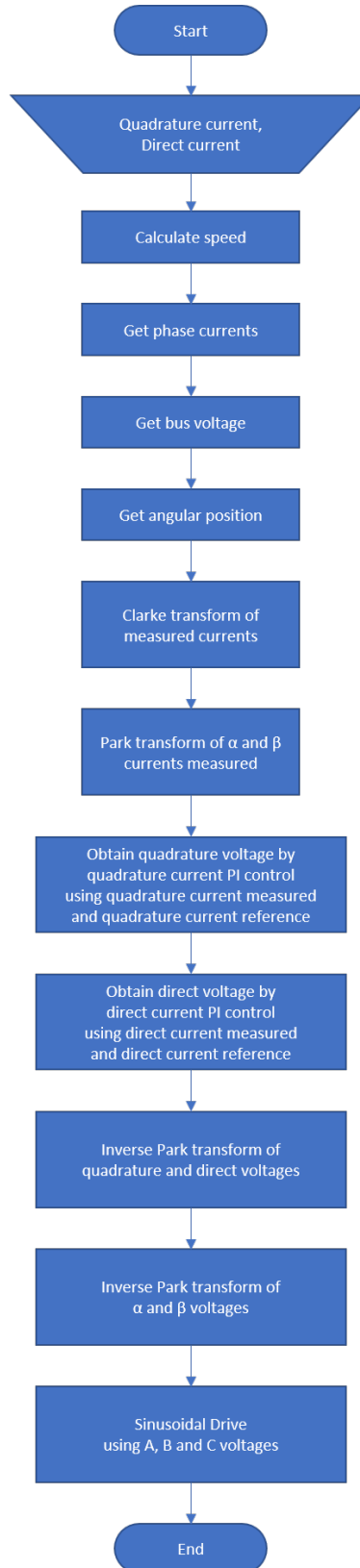


Figure 5.18: Field Oriented Control Flowchart

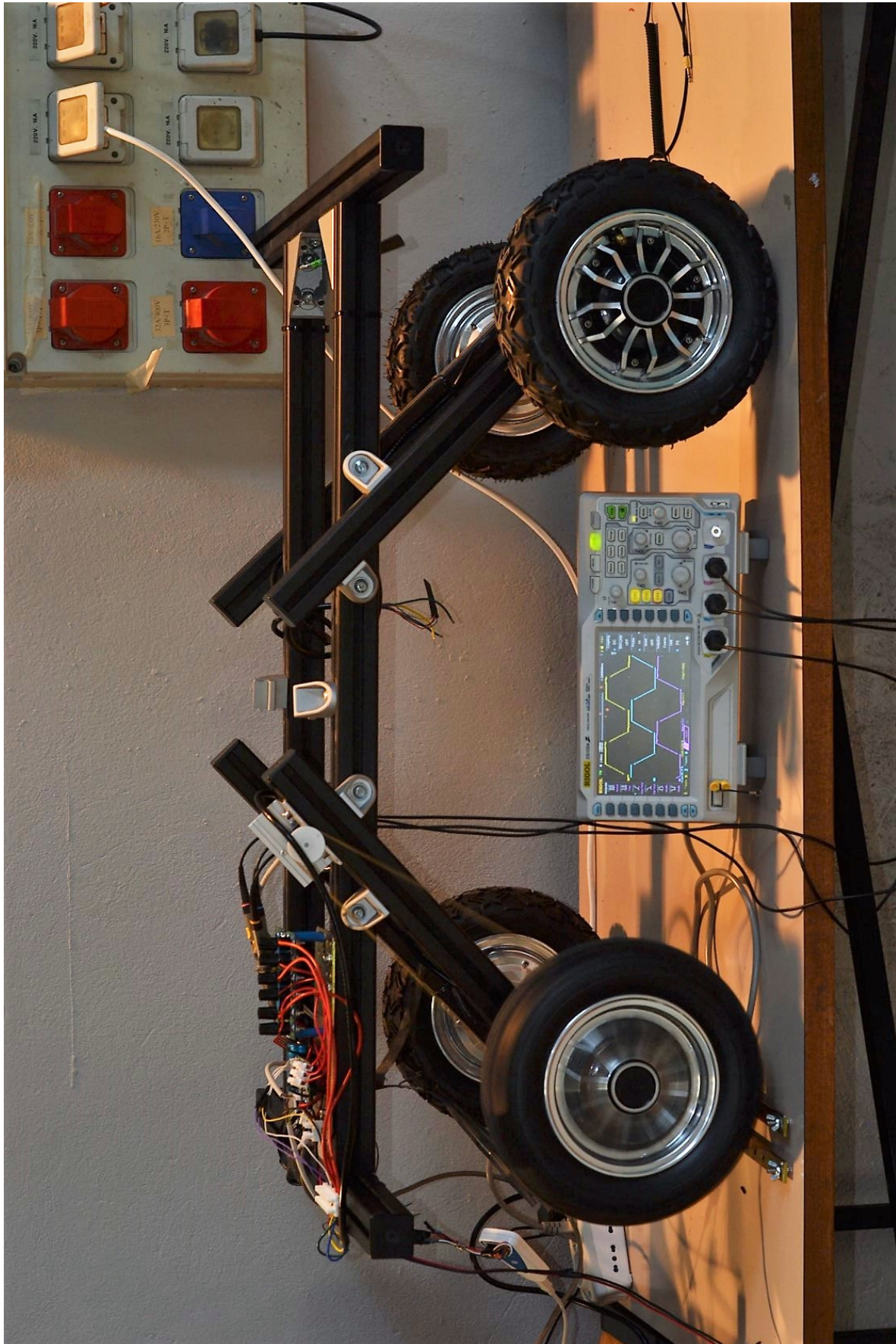


Figure 5.19: Trapezoidal drive implemented on in-wheel motor mounted on ROBI'

5.3 TEST SETUP

This section explains the implementation of the test bench developed to measure the driving capabilities of the WMU. It is also a preamble to the next chapter, which shows the results of the implementation of the different driving methods under different test conditions.

5.3.1 *Measurement Board*

In order to be able to obtain the voltage and current waveforms of the motor, it was necessary to condition those signals to be measured by an oscilloscope or by any other device. With this aim, a measurement board was developed. The schematic files of this measurement board can be found in Appendix C.

The board was designed to acquire data by means of connecting an oscilloscope to the circuit through test points or by setting up an embedded system to acquire the information, transform it and transfer it to a UI by USB or any other digital communication protocol available. The embedded system can be setup by soldering an Atmel microcontroller directly to the board or by connecting an Arduino-like device. Since the Arduino doesn't have a sampling frequency fast enough to read the analog signals of this project, we used the approach of connecting an oscilloscope directly to the board through the test points.

For future reference, it is possible to use other more powerful devices instead of the Arduino to acquire the signals, like a Nucleo board, by STMicroelectronics, which has the same pinout of an Arduino board.

The operating voltage levels of the board can be selected depending on the available power supply and the operating logic levels of the embedded system.

In order to obtain the information of the motor, its terminals must connected to the board by means of three large "banana" connectors. The current of the motor flows through wide copper pads, which are connected to voltage test points, passing through the current transducers and connected to other three banana terminals, which are connected to the WMU.

5.3.1.1 *Voltage Measurement*

The voltage of the motor windings was measured from the motor terminals with reference to ground. This voltage can be acquired by connecting an oscilloscope to the test points available for this, or it can be measured by an embedded system.

In order to condition the signal to be read by the embedded system, it was necessary to implement a circuit with operational amplifiers to reduce the measured voltage levels of the motor to logic levels. The

gain of the amplifiers can be set by modifying the dip-switches in the board.

5.3.1.2 Current Measurement

The current of the motor was measured between the driver and the motor terminals. It was obtained by means of the LEM current transducer HXS 20-NP, which is a Hall effect sensor that can be configured to measure up to 60A, changing the sensitivity of the transducer by modifying its pinout interconnection, which changes the current distribution inside the sensor, increasing or reducing its effect over the Hall effect sensor.

As in the case of the voltage measurements, the signal can be also obtained by the embedded system and its conditioned by operational amplifier circuits with an adjustable gain.

5.3.2 User Interface

The board was connected to a UI by means of a USB-Serial transceiver, which was connected to the available UART port.

The UI was developed in LabView because of the ease of implementation of automatic serial communication algorithms which allow us to control different variables of the WMU, like the reference input values ($I_{q,ref}$, $I_{d,ref}$, ω_{ref}) and the parameters of the controllers implemented (K_P and K_I). It is also possible to obtain and plot different values measured and calculated by the microcontroller, like the angular position and speed of the rotor and the values of the measured currents and voltages.

This UI allowed us to run the tests of the capabilities of the WMU.

5.3.3 ROBI' Setup

The WMU and the measurement board were mounted into ROBI' with the objective of having a mechanically stable arrangement of the components.

In order to test the torque development of the in-wheel motors, ROBI' was mounted in a torque test bench, which consists on a DC current generator with a resistance connected to its output. The DC current generator was manufactured by Ercole Marelli & CSA – Milano.

One of the in-wheel motors mounted on ROBI' was attached to the shaft of the generator by means of a custom-designed coupler, which was 3D printed in PLA plastic. This coupler was attached to the rim of the in-wheel motor by replacing three of the M3 screws that attach the rim to the wheel for larger ones in order to be able to attach it.

Table 5.5: Marelli DC current generator characteristics in function on its rotation speed

Power	10/40kW
Voltage	110/440V
Current	91A
Speed	750/3000RPM
Excitation voltage	220V
Excitation current	1.5A

The generator is mounted into a large base, holding it by its rotor (with the use of bearings) and not by its stator. This configuration allows the measurement of the torque generated by means of a load cell, which measures a compression or a tension force applied to it, proportional to the torque applied to the generator, which depends on the power that is being generated to energise the load connected to its terminals. The power generation depends on the field excitement of the generator, therefore, we were able to define a constant torque at a given speed by changing its excitation voltage.

The load cell information was obtained by means of an instrumentation amplifier, model HX711, which has a digital interface. The amplifier output was connected to an Arduino, which translated the information of the sensor into an applied torque, equal to the force measured multiplied by the distance from the center of the generator to the load cell, whose direction is practically tangential to the generator circumference. Before each test was realized, the torque measurement was calibrated, following a procedure like the one applied for the current offset calibration (5.2.3).

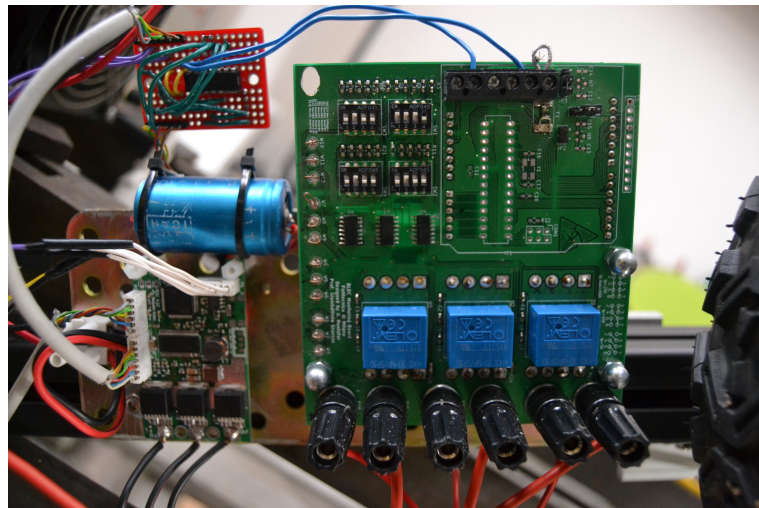


Figure 5.20: WMU connected to measurement board, mounted in ROBI's structure



Figure 5.21: In-wheel motor attached to Marelli DC generator

6

RESULTS

This chapter contains waveforms and plots referent to the tests realized to determine the driving ability of the WMU and their explanations. The tests were realized on the in-wheel motor by applying two types of driving methods: trapezoidal and sinusoidal, both at open loop and closed loop. These driving methods were tested under two conditions: loaded and unloaded.

The power was supplied by an Elind KL Series power supply with a current limit of 15 A. The analog signals were obtained by a Rigol oscilloscope, model DS1054. The speed readings were obtained through the implemented LabView UI. All the plots and waveforms were processed in Matlab for their analysis.

6.1 TRAPEZOIDAL DRIVE – OPEN LOOP

The trapezoidal open loop driving was executed by setting a duty cycle directly into the six-step sequence PWM. The algorithm was executed at 50kHz and the PWM signal has a frequency of 15kHz.

Figure 6.1 shows the different speeds achievable by applying different duty cycles with different torque loads. The curves on the plot start on different duty cycles since the torque load couldn't reach a steady value until a certain speed was established. For example, for the measurement with a load equal to 3Nm, the curve starts at a duty cycle equal to 30%, since at a duty cycle lower than this or a speed lower than 10rad/s, the load can't be generated by the test bench, which would apply around 2Nm, therefore those measurements were not considered for the plot. On the other hand, the curves that don't show large duty cycle values (5 and 6Nm), is because the power supply couldn't feed enough current to the driver to reach such torque.

Figures 6.2, 6.3, 6.4 and 6.5 show the voltage waveforms measured on the terminals of the motor. The trapezoidal BEMF generated on its coils due to the six-step sequence algorithm can be identified as the ramp-up and ramp-down signals between rectangular drives, mainly when the duty cycle is 100%. From these figures we can also identify that when the load increases, the speed of the motor decreases since there is no speed control loop.

Figures 6.6, 6.7, 6.8 and 6.9 show the current waveforms. We can see from its shape, mainly when the duty cycle is 100%, that the BEMF of the motor is sinusoidal, even if the trapezoidal drive is applied. As the load increases, along with the reduction of the speed, the current consumption increases. It can also be appreciated that the current

waveforms present a larger ripple as the duty cycle and the load increase, which represents a torque ripple that reduces the performance of the motor.

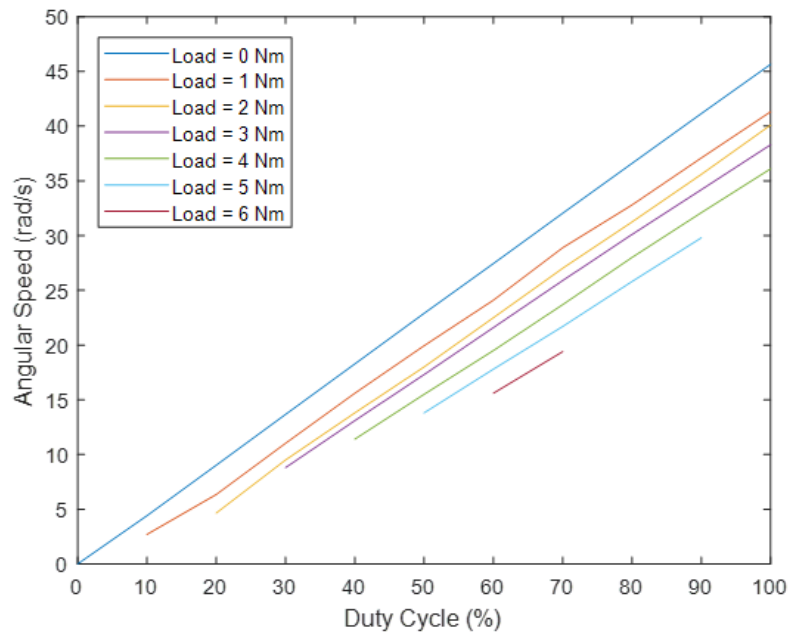


Figure 6.1: Plot of the different speeds achieved applying a known duty cycle using an open loop trapezoidal drive with different loads

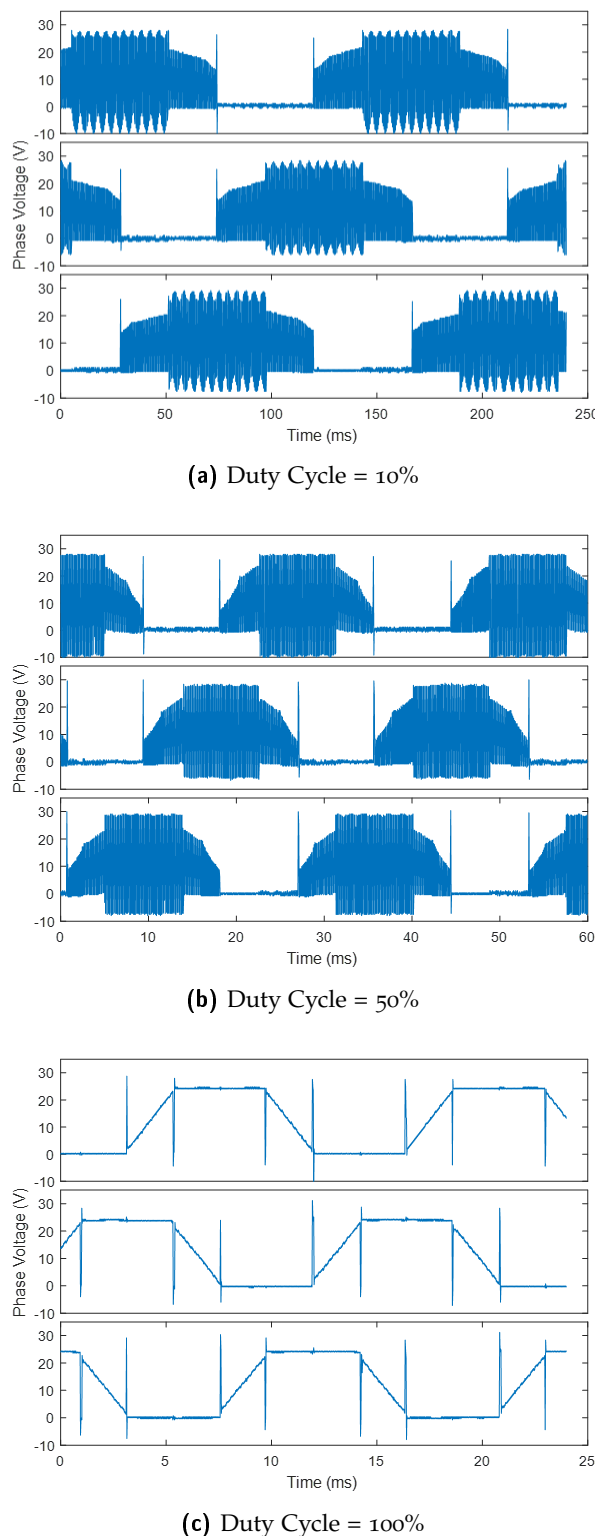
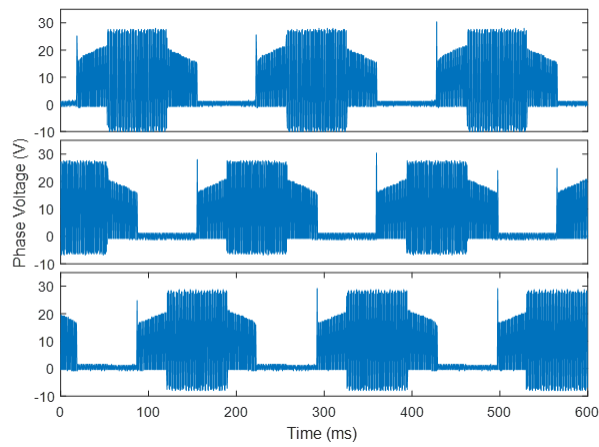
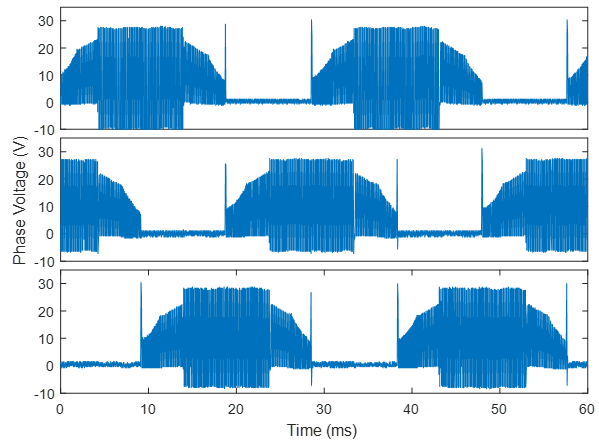


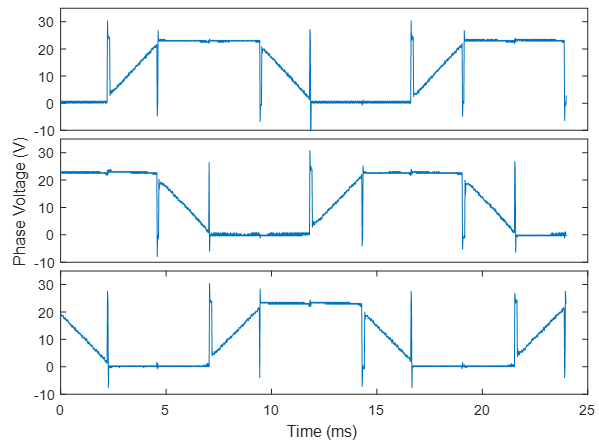
Figure 6.2: Trapezoidal drive voltage waveforms without load applied



(a) Duty Cycle = 10%



(b) Duty Cycle = 50%



(c) Duty Cycle = 100%

Figure 6.3: Trapezoidal drive voltage waveforms with load = 1 Nm

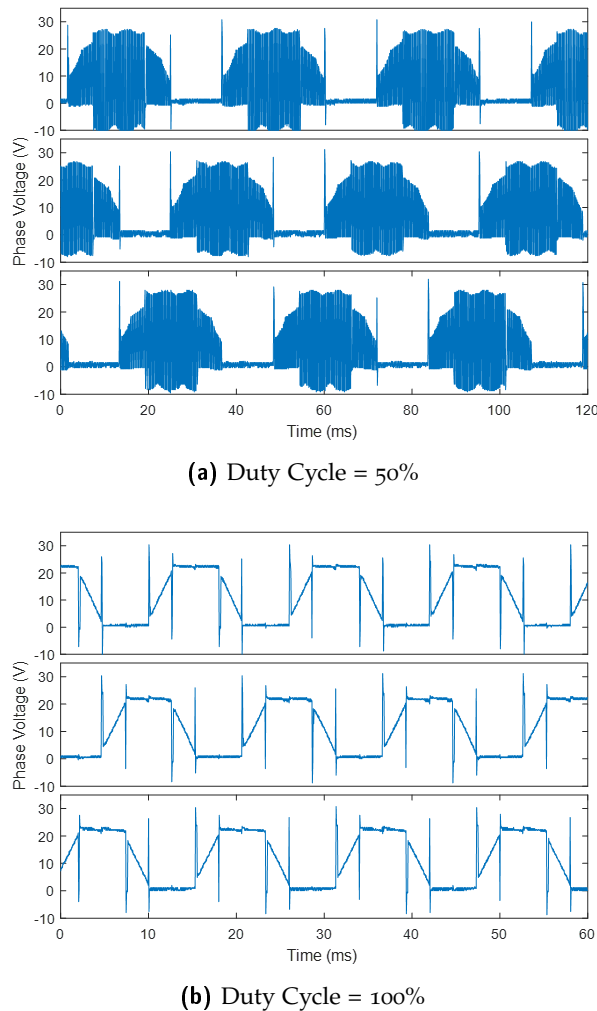


Figure 6.4: Trapezoidal drive voltage waveforms with load = 3 Nm

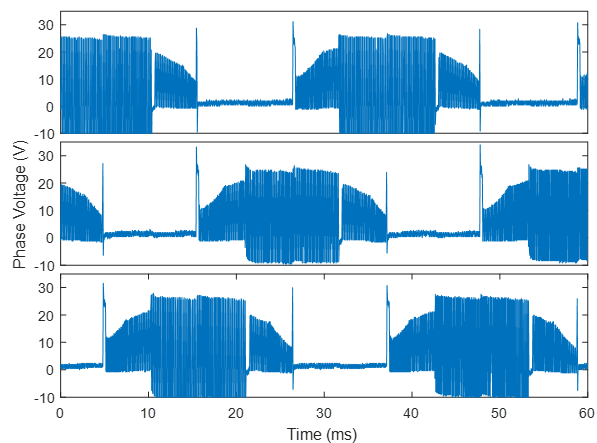


Figure 6.5: Trapezoidal voltage waveforms drive Duty Cycle = 70% and load = 6 Nm

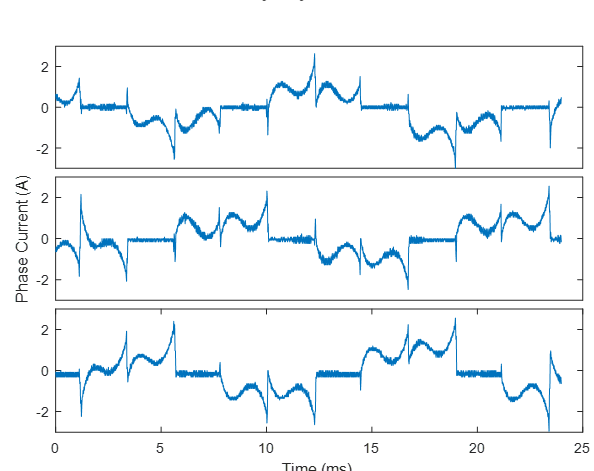
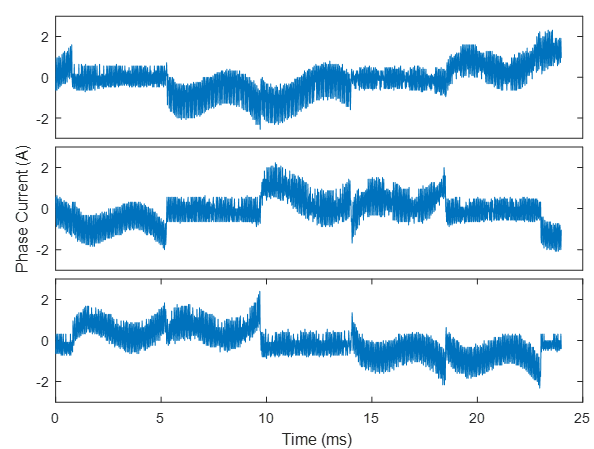
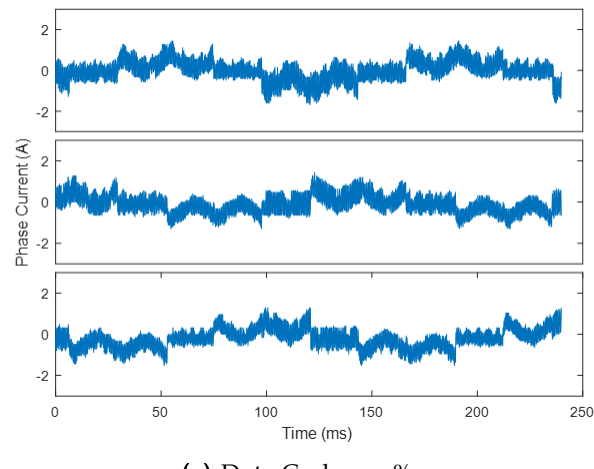


Figure 6.6: Trapezoidal drive current waveforms without load applied

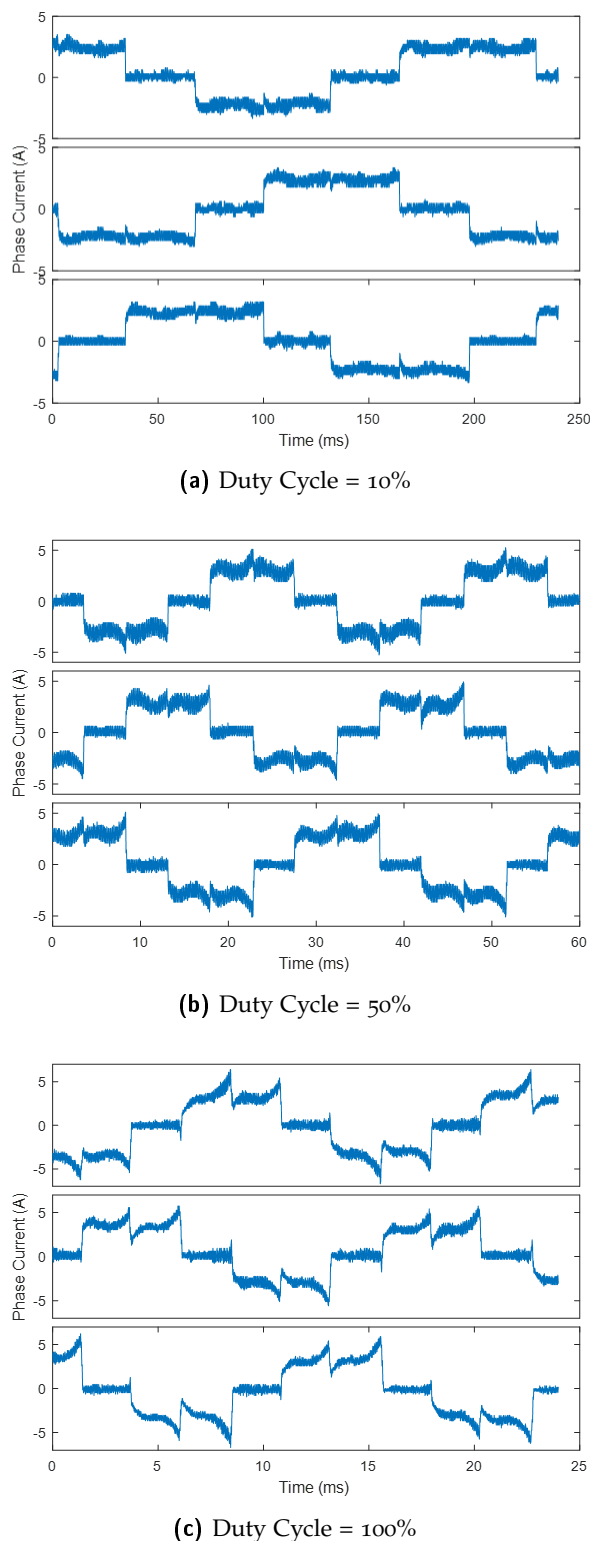


Figure 6.7: Trapezoidal drive current waveforms with load = 1 Nm

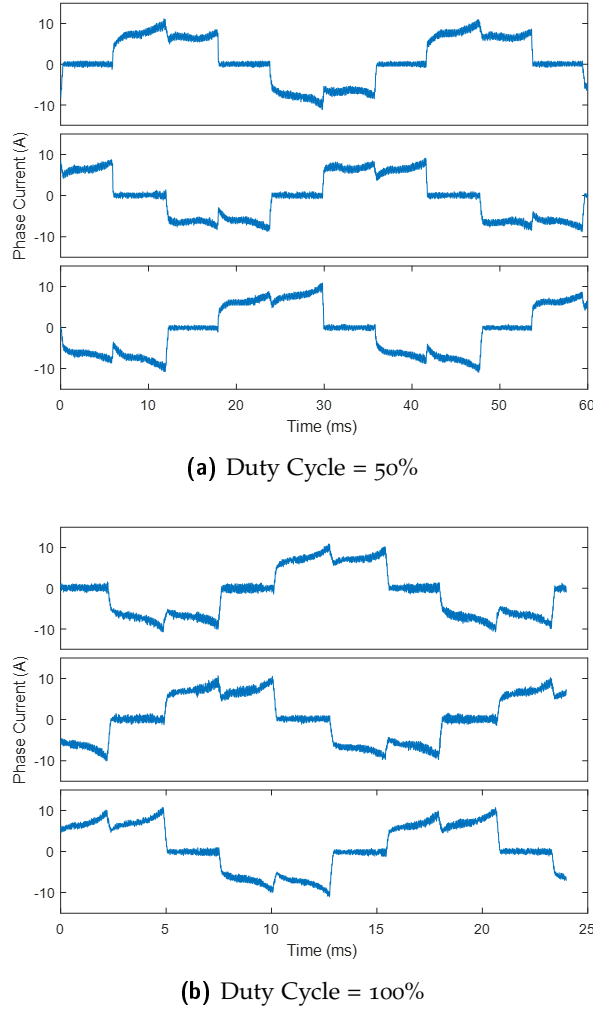


Figure 6.8: Trapezoidal drive current waveforms with load = 3 Nm

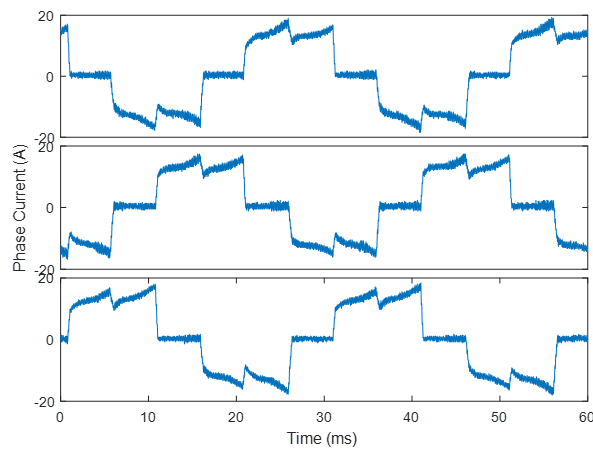


Figure 6.9: Trapezoidal drive current waveform with duty cycle = 70% and load = 6 Nm

6.2 SPEED CONTROL WITH TRAPEZOIDAL DRIVE

To see the behaviour of the speed control, different step signals were applied with different loads and different controller parameters.

The torque loads were setup first at a steady speed to know the correct excitation voltage of the field, then the motor was stopped and step signal was applied.

Figures 6.10, 6.11 and 6.12 show the different step responses between the same step signal applied and the same load but with different control parameters K_p and K_i . It can be identified that, by changing the value of K_i we obtain different damping behaviours on the motor.

In Figure 6.13 we compare two signals with different K_i values, but in this case, in the test to obtain the signal with $K_i = 0.03$ the current was limited by the power supply. This shows that, even if K_i is larger, the slew rate of the speed depends on the current limit of the power supply.

It is possible to see also the speed behaviour of the system compared with the duty cycle applied by the control algorithm on Figures 6.14 and 6.15.

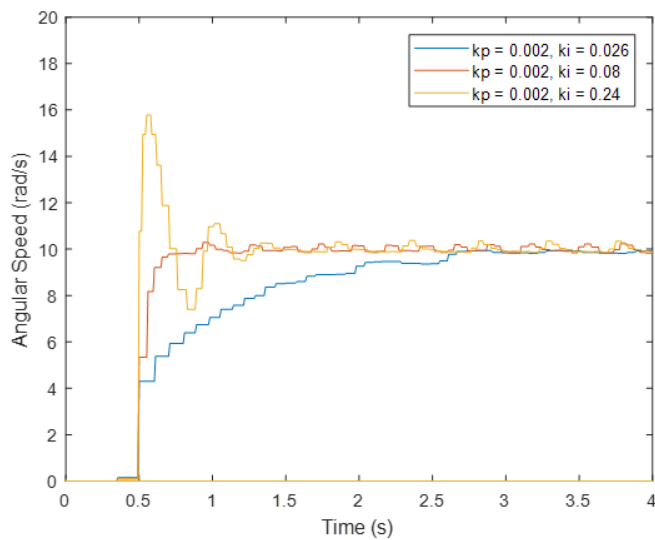


Figure 6.10: Step response to a 10 rad/s signal without load applied

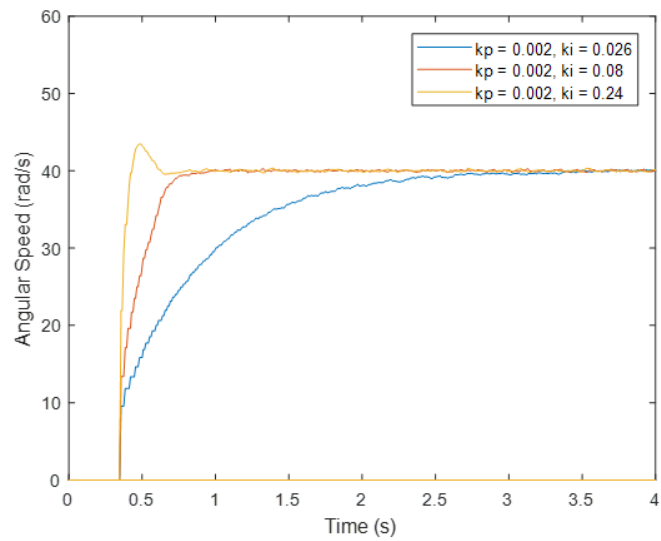


Figure 6.11: Step response to a 40 rad/s signal without load applied

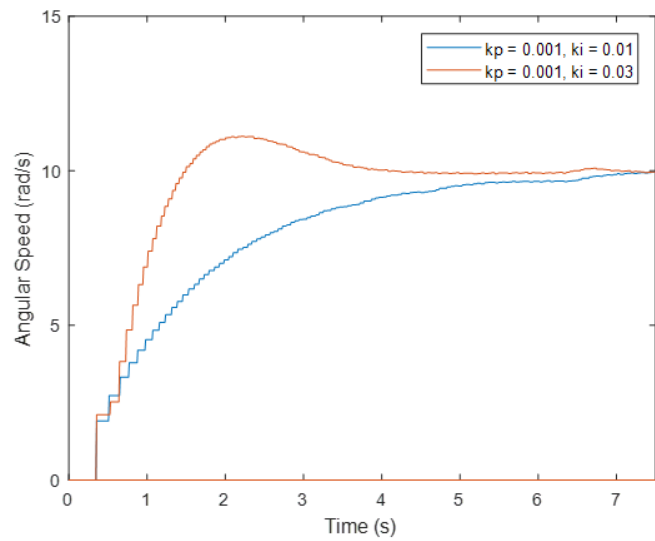


Figure 6.12: Step response to a 10 rad/s signal with a 3 Nm load

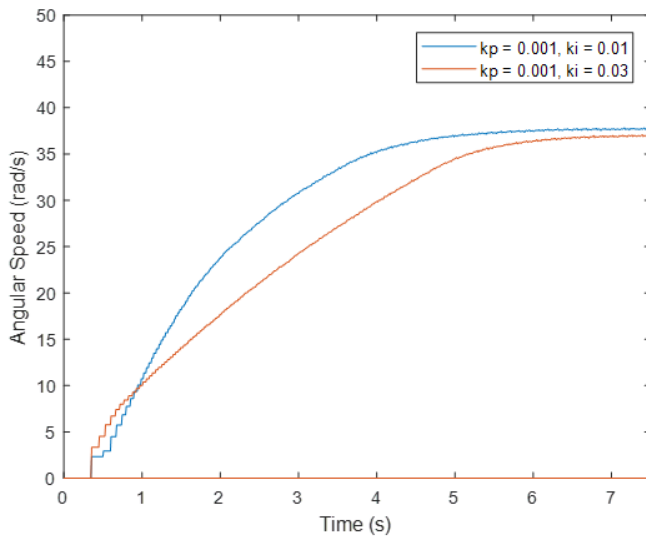


Figure 6.13: Step response to a 40 rad/s signal with a 3 Nm load

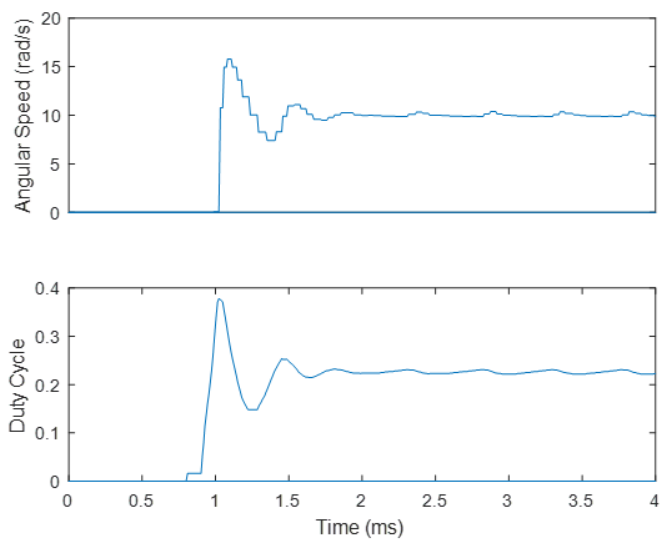


Figure 6.14: Step response to a 10 rad/s signal without load, compared to its driving duty cycle signal

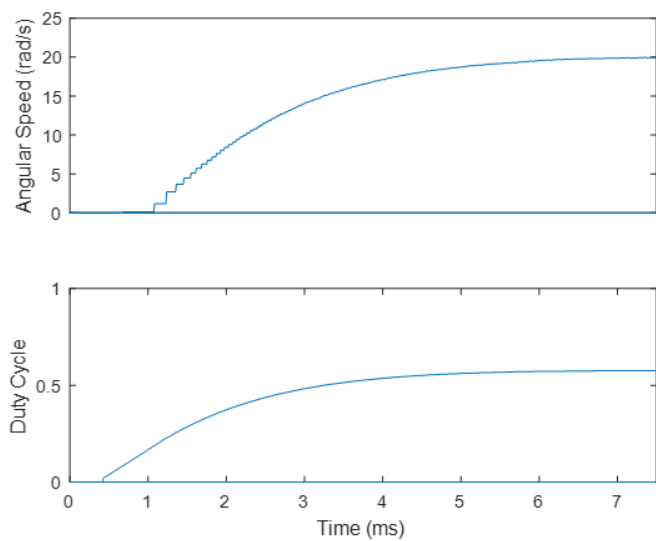


Figure 6.15: Step response to a 20 rad/s signal with a 3 Nm load, compared to its driving duty cycle signal

6.3 SINUSOIDAL DRIVE – OPEN LOOP

This test was applied at the beginning of the development of the Field Oriented Control to test the generation of a sinusoidal waveform depending on the angular position of the rotor. The signals were generated by applying a constant amplitude value as a quadrature voltage without any load attached to the motor.

Figure 6.16 shows the center-aligned PWM signal generated by the inverter in the motor terminals. We can identify the ringing effect on the rising and falling edges but it has a small duration, therefore it can be neglected.

It can be appreciated in Figure 6.17c that the current in the highest and lowest side of the signal are limited by the LEM current sensor of the measurement board at 20A. While doing these tests, one wire of the measurement board started melting since it didn't have the required diameter for this amount of current. Also the LEM transducers became hot, since they were configured to measure signals of $\pm 5A$ to provide a better resolution.

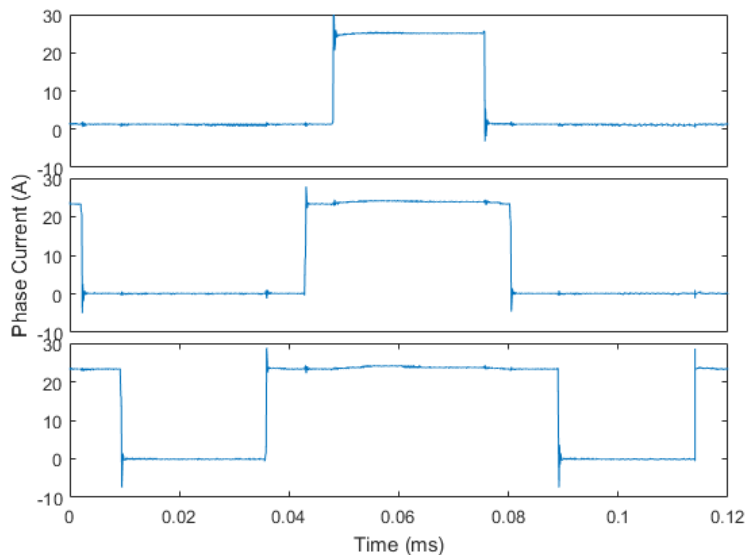
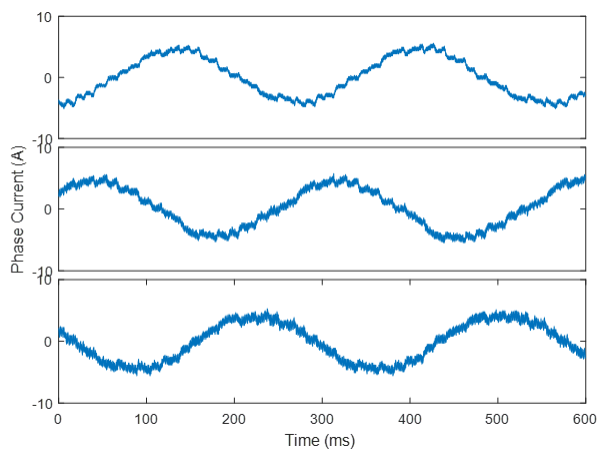
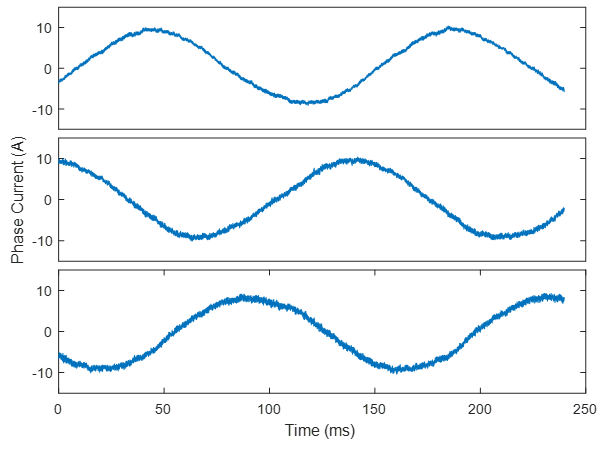


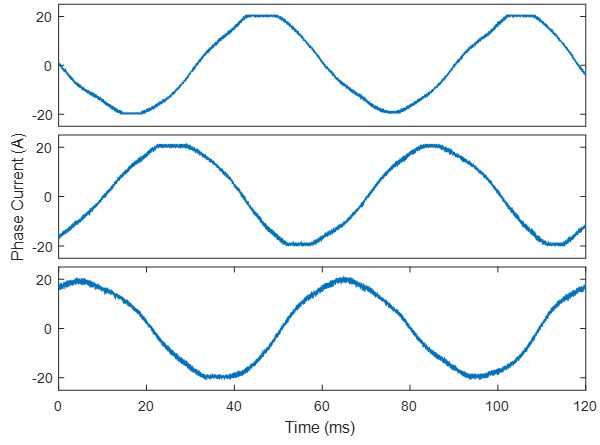
Figure 6.16: Center-aligned PWM voltage waveform



(a) Quadrature voltage = 1V



(b) Quadrature voltage = 2V



(c) Quadrature voltage = 5V

Figure 6.17: Sinusoidal drive current waveforms without load applied

6.4 FIELD ORIENTED CONTROL

These tests were applied by exciting the field of the DC generator to the maximum available ($30V$), so by setting up a reference quadrature current on the controller, the motor would reach a steady state speed when the torque applied by the load is equal to the torque applied by the motor.

The FOC loop is executed at $10kHz$ due to the limitation imposed by the Orbis encoder.

From these tests we can compare the torque measured with the torque applied by multiplying the amplitude of the current waveform by the torque constant of the motor K_T equal to $0.4506Nm/A$. By doing this, we see that there is a loss of about 30% of the torque on the tests with 1 and $3Nm$ loads, which can be due to mechanical losses and to measurement errors on the load torque. In the case when the load is $5Nm$ the torque loss is around 50%. We can identify that this current presents a distortion on its sinusoidal waveform and an offset of almost $1A$, which can be the reason of such power loss.

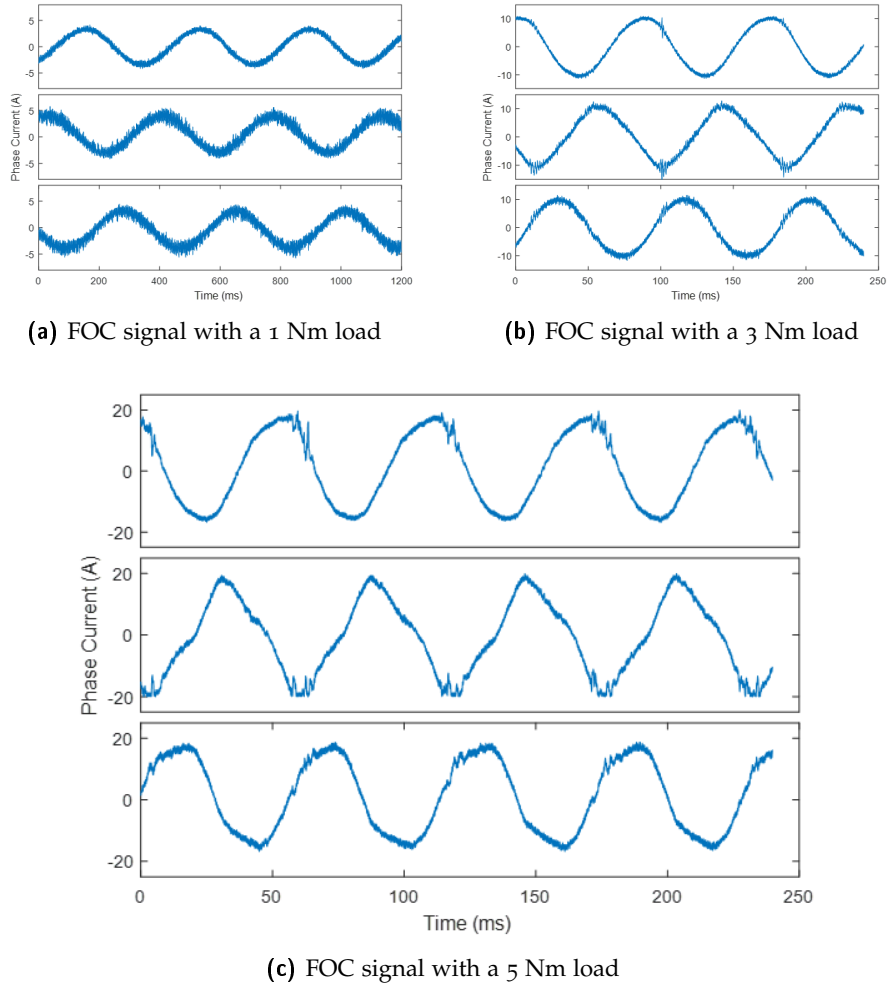


Figure 6.18: FOC with different loads

6.5 SPEED CONTROL WITH FIELD ORIENTED CONTROL

The behaviour of the driver with different reference speeds and load values can be appreciated from the remaining figures of this chapter.

By analysing the frequency of the waveform in Figure 6.19a we can see the ability of the controller to move the motor at a low speed with a load applied.

It can be appreciated in Figures 6.19c, 6.20c and 6.20d that the signal gets distorted when the speed reaches approximately 20rad/s . This is due to the maximum frequency achievable by the Orbis encoder. Currently it represents a trade-off between choosing the trapezoidal driven speed control, which works fine at high speeds since the angular position feedback is given by the hall effect sensors, and the FOC driven speed control, which works fine at low speeds but at high speeds becomes unpredictable.

In order to have an idea of the linear speed achievable by the in-wheel motor, 20rad/s is equivalent to 9.1km/h , which is approximately the human walking speed.

In Figure 6.22 we can see the comparison of the behaviour of the controller with the same step signal (0 to 10rad/s) but with different load. When the load is 3Nm , the slope of the signal becomes limited by the controller parameter I_{MAX} , which defines the saturation of the integral part of the controller to avoid current peaks. This parameter can be modified accordingly to the capacities of the system, but caution must be taken since this can provoke malfunctioning of the circuit.

In figure 6.24 we can appreciate the three phase currents settling into steady state after a step signal is commanded to the controller.

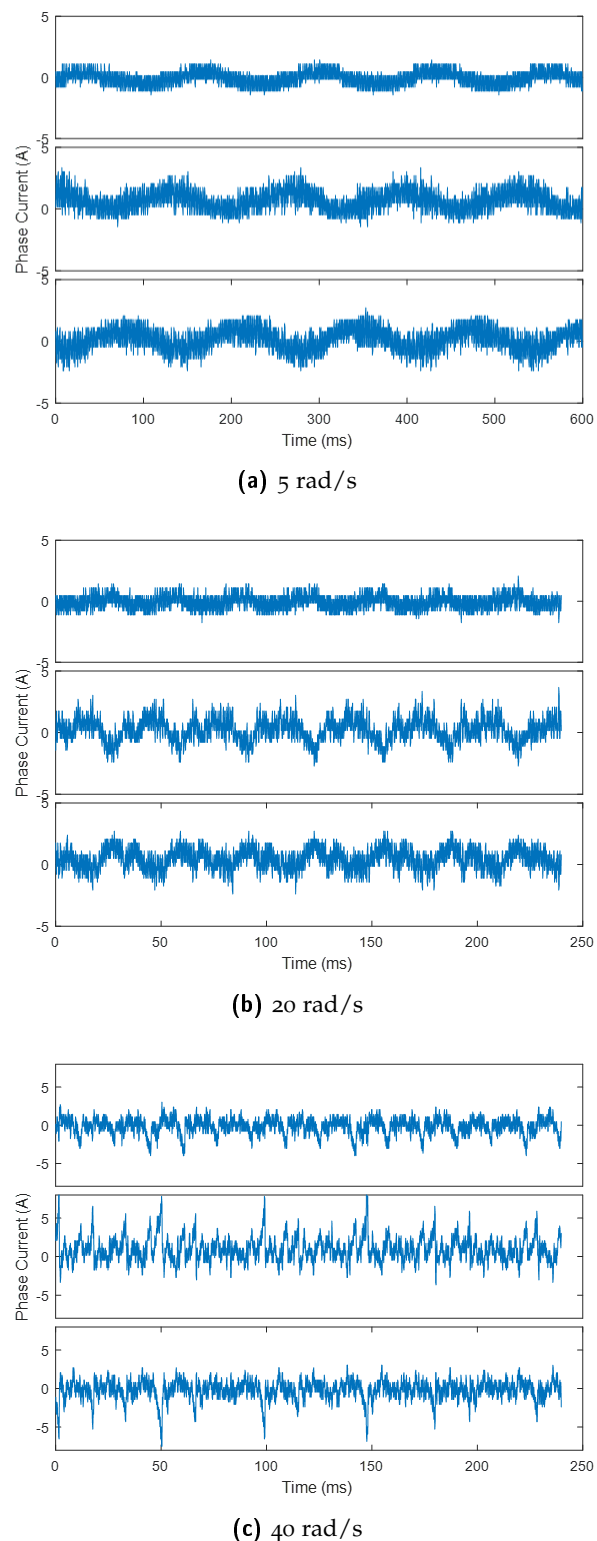


Figure 6.19: FOC speed control loop without load applied

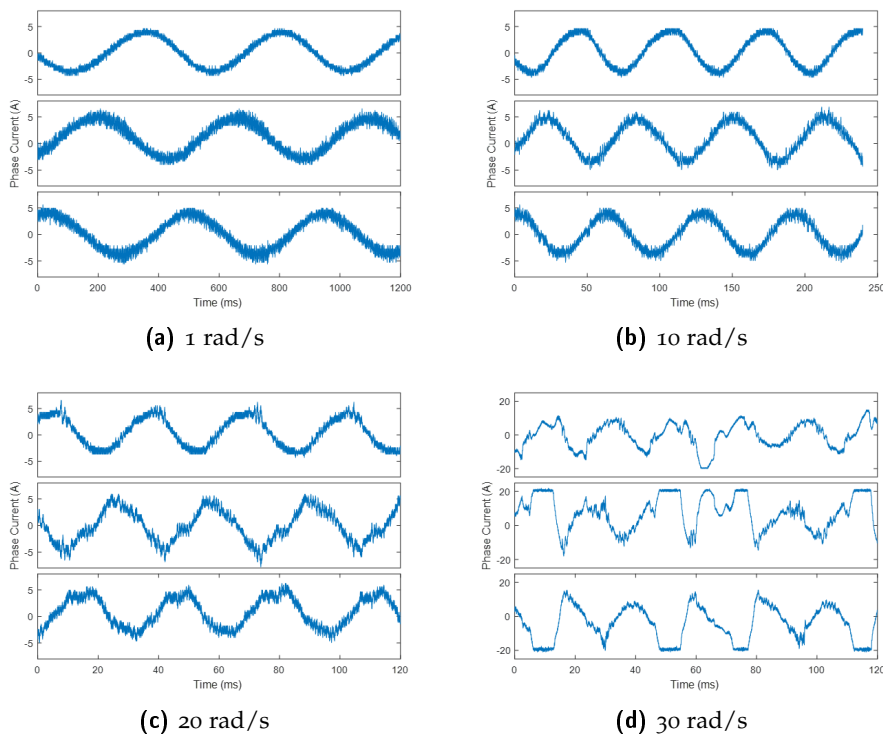
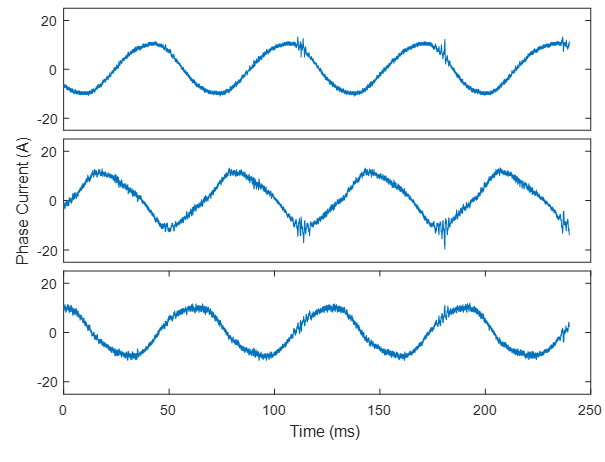
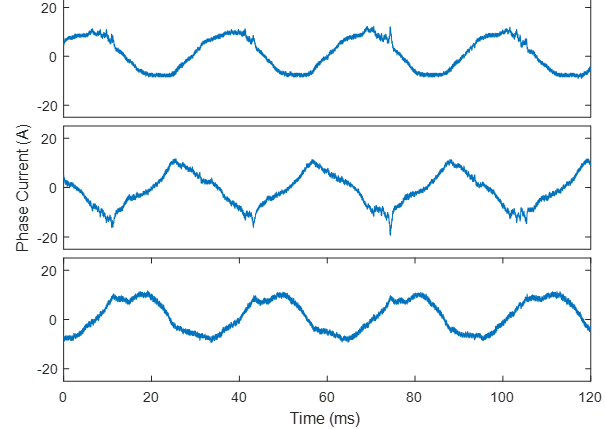


Figure 6.20: FOC speed control loop with 1 Nm load



(a) 10 rad/s



(b) 20 rad/s

Figure 6.21: FOC speed control loop with 3 Nm load

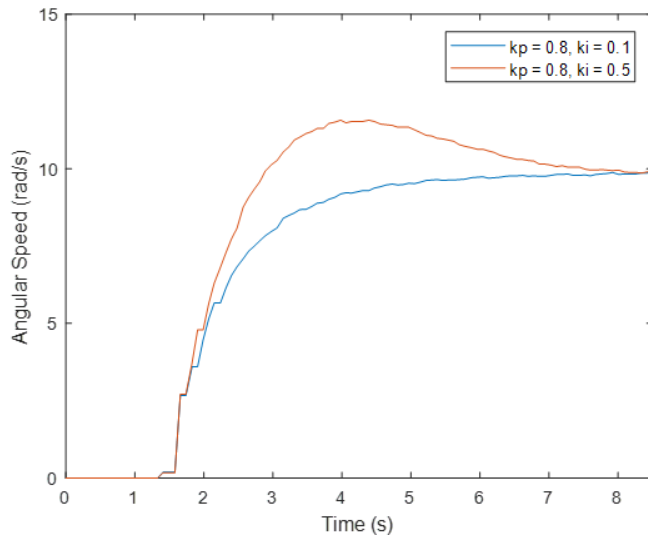


Figure 6.22: Step response to a 10 rad/s signal and a load of 1 Nm with different controller parameters

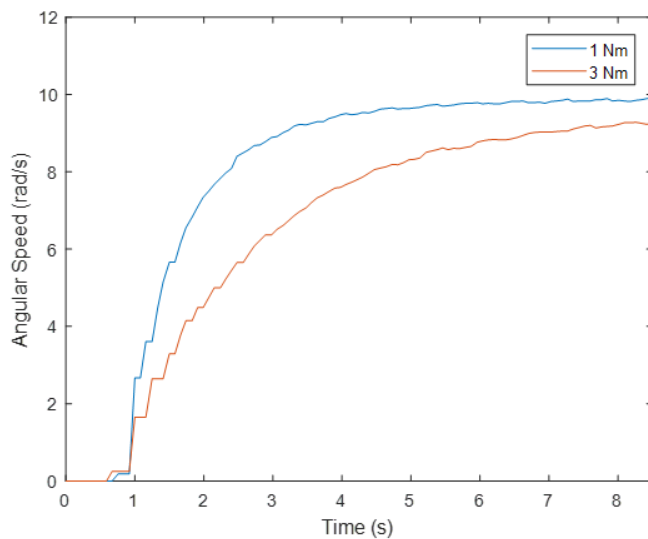


Figure 6.23: Step response to a 10 rad/s signal with different loads

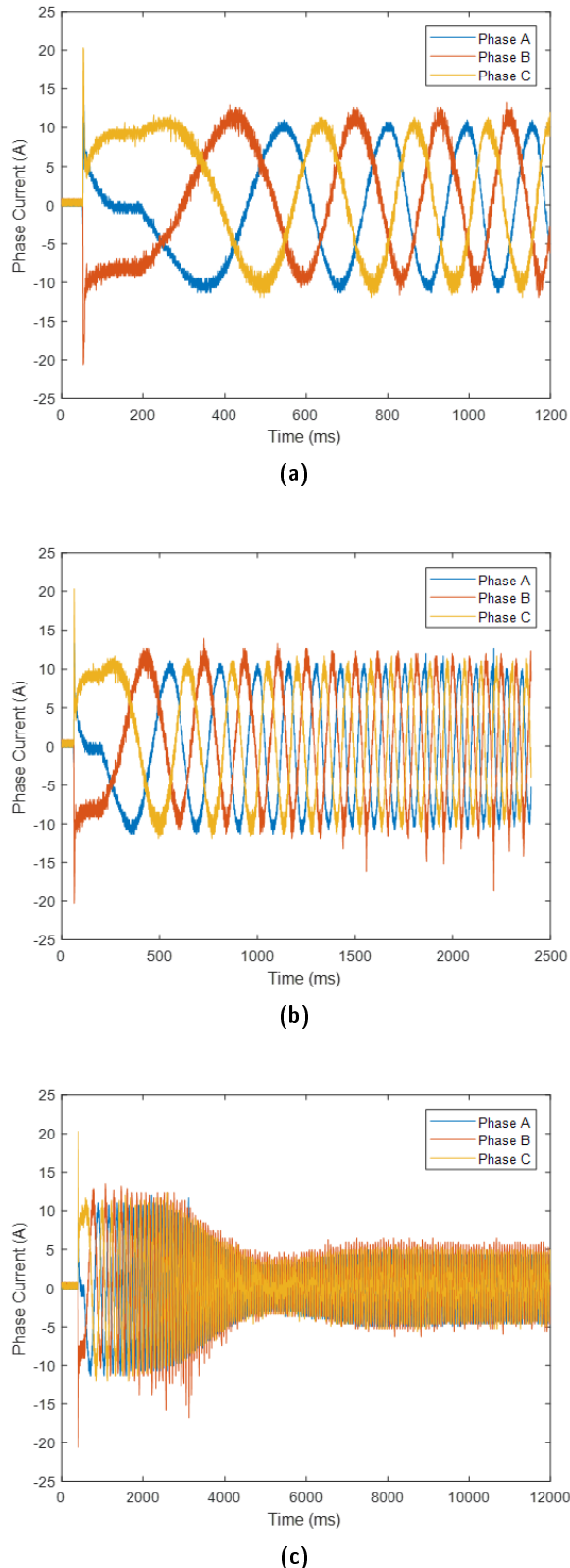


Figure 6.24: FOC three-phase current waveform in a step response to a 10 rad/s signal with a load of 1 Nm

7

CONCLUSION

Since we were able to drive the in-wheel PMSM motor, we can conclude that the implementation of the driving algorithms on the WMU based on the hardware design of the VESC board was successful. But, after analizing the implementation procedure and the test results, we can also conclude that the architecture proposed is not optimal for such motor drive system.

The main positive aspects of the architecture implemented are the following:

- The driver *DRV8302* is a useful tool mainly due to three reasons: it solves all the issues related to MOSFET driving and the current provided to charge the gate is enough to have a good driving frequency; it protects the board from overcurrent and undervoltage conditions; it provides a voltage regulator, which reduces the area and the components on the board.
- The microcontroller capacity was not a limitation for the implementation of the algorithms required to drive the motor. Also, the implementation of Miosix as the operating system for the WMU simplified the development of those algorithms.

The main issues with the implementation following this topology are the following:

- The driver *DRV8302* provides only two shunt current amplifiers, which was one of the reasons of the generation of an offset in the driving signals in the implementation of the FOC, which reduces the efficiency of the motor.
- The VESC board doesn't consider any heat dissipation strategy for the power MOSFETs, which reduces their power dissipation capacity and it might lead to a failure in the system.
- The model selected of the Orbis sensor becomes a limiting factor for the implementation of the FOC due to its maximum transmission frequency.

7.1 CHANGES PROPOSAL

Based on the previous analysis of the development of the WMU, we can propose the following changes for a future development:

- Since the only problem with the *DRV8302* driver was that there are only two shunt current amplifiers, it can be replaced by a

more recent version, the *DRV8320*, which includes the same functionalities but it considers three shunt current amplifiers.

- Due to the large currents flowing through the board, we need to use wires with a larger diameter than the one used in the developed system to avoid melting them. The problem with using wider wires is that it becomes mechanically unsafe to have them soldered directly to the board, so it is important to consider the use of connectors for the power supply and for the motor terminals.
- The last proposal is to change the model of the Orbis encoder to one with a higher transmission frequency to avoid the frequency limitation in the FOC algorithm.

7.2 FUTURE WORK

The implementation of some of the requirements for the WMU is still pending.

One of those requirements is the communication between ECUs through the CAN communication protocol. As mentioned before, the drivers for this were provided by the Skyward Experimental Rocketry team, therefore, its implementation should be simple.

Another important point to work on, is the implementation of strategies to improve the efficiency of the motor, like the reduction of current offsets by using mean value control techniques, and the reduction of harmonic signals by the implementation of other driving methods, like the space vector modulation.

BIBLIOGRAPHY

- Arrigo, Jason (2006). *Input and Output Capacitor Selection*. Texas Instruments (cit. on p. 46).
- Bascetta, Luca, Marco Baur, and Giambattista Gruosso (2017a). "Electrical Unmanned Vehicle Architecture for precision farming applications." In: (cit. on p. 39).
- (2017b). "ROBI': A Prototype Mobile Manipulator for Agricultural Applications." In: *MDPI Electronics* (cit. on pp. 2, 6, 39).
- BASIL Networks, PLLC (2003). *Permanent Magnet Brushless Motor*. URL: <https://www.basilnetworks.com/article/motors/brushlessmotors.html> (cit. on p. 18).
- Bose, B. K., T. M. Jahns, R. D. Lorenz, G. Pfaff, P. Pillay, M. H. Rashid, T. Sebastian, and G. R. Slemon (1989). *Performance and Design of Permanent Magnet AC Motor Drives*. IEEE (cit. on p. 9).
- Doppelbauer, Martin (2012). *The Invention of the Electric Motor*. URL: <https://www.eti.kit.edu/english/1376.php> (visited on 02/28/2012) (cit. on p. 1).
- Electrical Motors Basic Components (2012). URL: <http://www.electrical-knowhow.com/2012/05/electrical-motors-basic-components.html> (visited on 05/01/2012) (cit. on p. 10).
- Ghioni, Massimo (2016a). *Introduction to Electrical Drives*. URL: <ftp://ftp.elet.polimi.it/users/Massimo.Ghioni/Power%20Electronics%20/Motor%20control/motor%20control%20overview/INTRODUCTION%20TO%20ELECTRICAL%20DRIVES.pdf> (cit. on p. 20).
- (2016b). *Lecture notes in Power Electronics* (cit. on pp. 9, 48, 51).
- Heath, Steve (2003). *Embedded Systems Design*. Newnes (cit. on p. 60).
- Jordan, Edward (1968). *Electromagnetic Waves and Radiating Systems*. Prentice-Hall (cit. on p. 12).
- Lawrenz, W. and N. Obermöller (2011). *CAN: Controller Area Network: Grundlagen, Design, Anwendungen, Testtechnik*. VDE Verlag (cit. on p. 56).
- Magnani, GianAntonio, Gianni Ferretti, and Paolo Rocco (2007). *Tecnologie dei sistemi di controllo*. McGraw-Hill (cit. on pp. 9, 11, 13, 68).
- Maxim Integrated (2016). *Shoot-Through Current*. URL: <https://www.maximintegrated.com/en/glossary/definitions.mvp/term/Shoot-Through%20Current/gpk/1040> (cit. on p. 64).
- Micro-Chip Technologies (2010). *NTC Thermistors*. URL: http://www.microchiptechno.com/ntc_thermistors.php (cit. on p. 57).
- RS Components Ltd. (2012). *PCB Connectors Overview*. URL: <https://uk.rs-online.com/web/generalDisplay.html?id=solutions%2Fpcb-connectors> (cit. on p. 47).

- Seymour Papert (1991). *Constructionism*. Ablex Publishing Corporation (cit. on p. xix).
- STMicroelectronics NV (2016a). *RM0090 Reference Manual* (cit. on p. 62).
- (2016b). *STM32F PMSM single/dual FOC* (cit. on p. 65).
- Terraneo, Federico (2014). *Miosix*. URL: <https://miosix.org/> (cit. on p. 61).
- Tesla, Nikola (1897). *On Electricity*. Electrical Review (cit. on p. 1).
- The Engineering ToolBox (2015). *Wire Gauges - Current Ratings*. URL: https://www.engineeringtoolbox.com/wire-gauges-d_419.html (cit. on p. 47).
- Vedder, Benjamin (2015). *VESC – Open Source ESC*. URL: <http://vedder.se/2015/01/vesc-open-source-esc/> (cit. on pp. 43, 44).
- Yedamale, Padmaraja (2003). *Brushless DC (BLDC) Motor Fundamentals*. Microchip Technology Inc. (cit. on pp. 17, 30, 31).

A

APPENDIX A: VESC BOARD SCHEMATIC FILES

BLDC motor controller

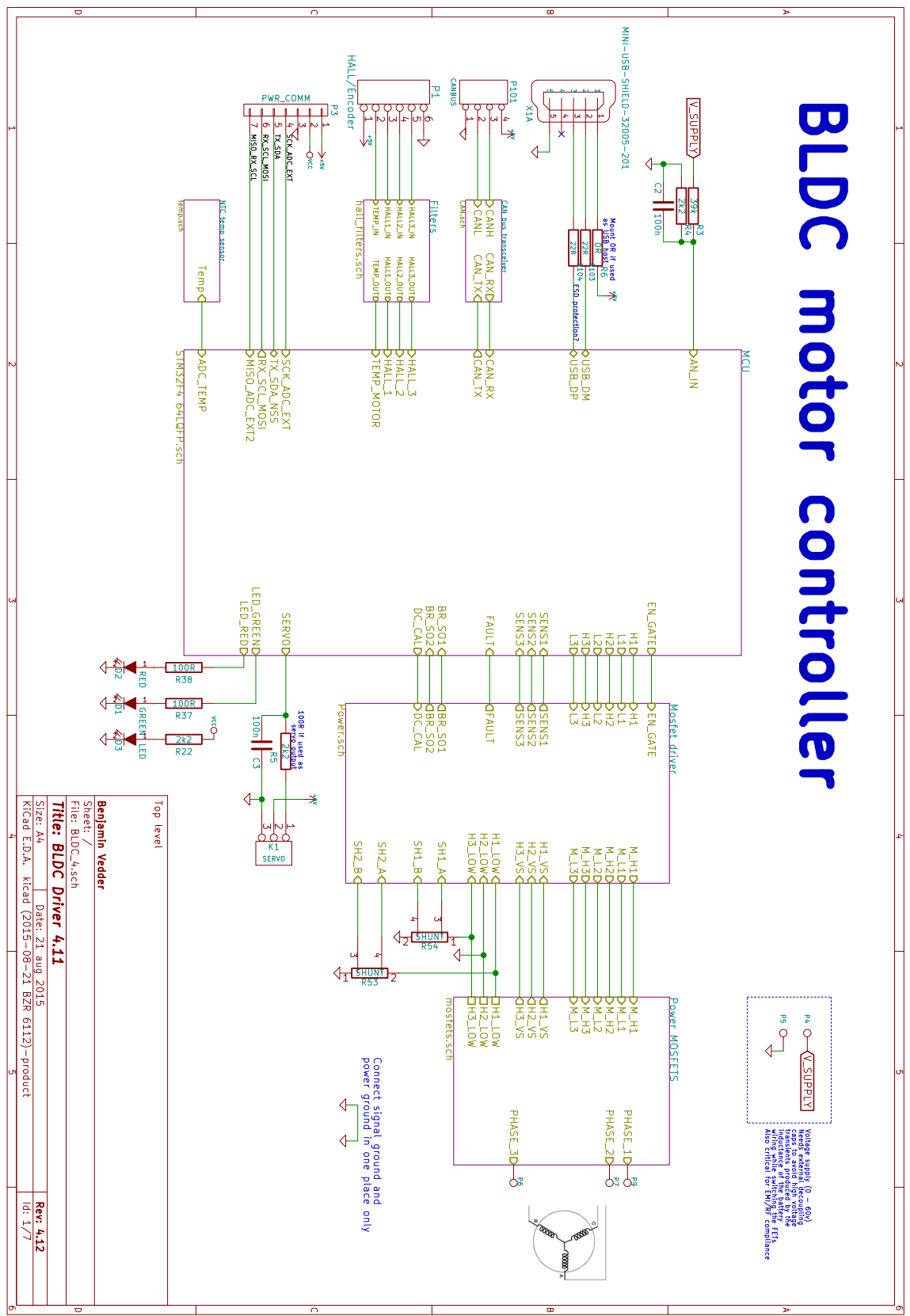


Figure A.1: Schematic Overview

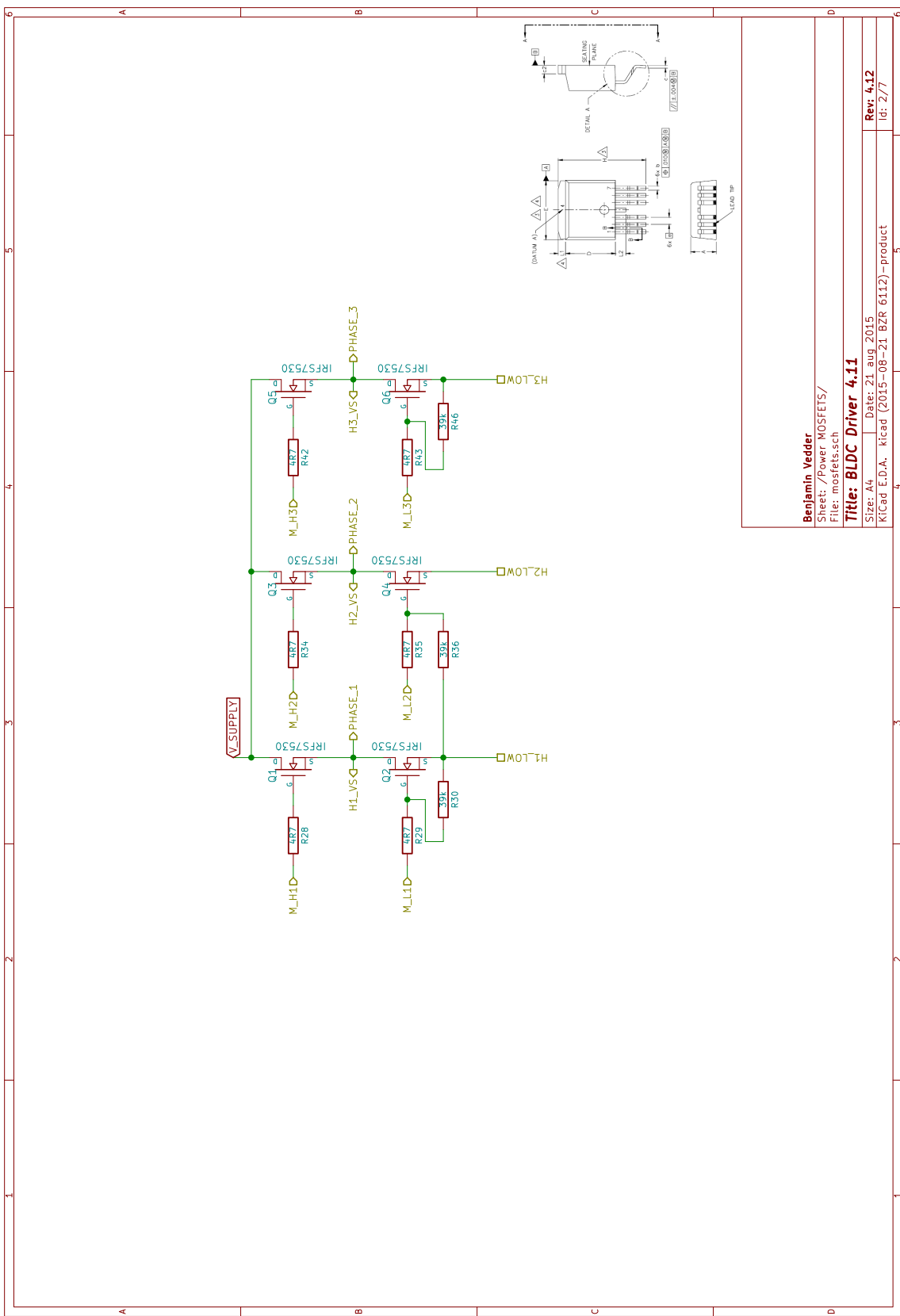


Figure A.2: Three-Phase MOSFET Inverter

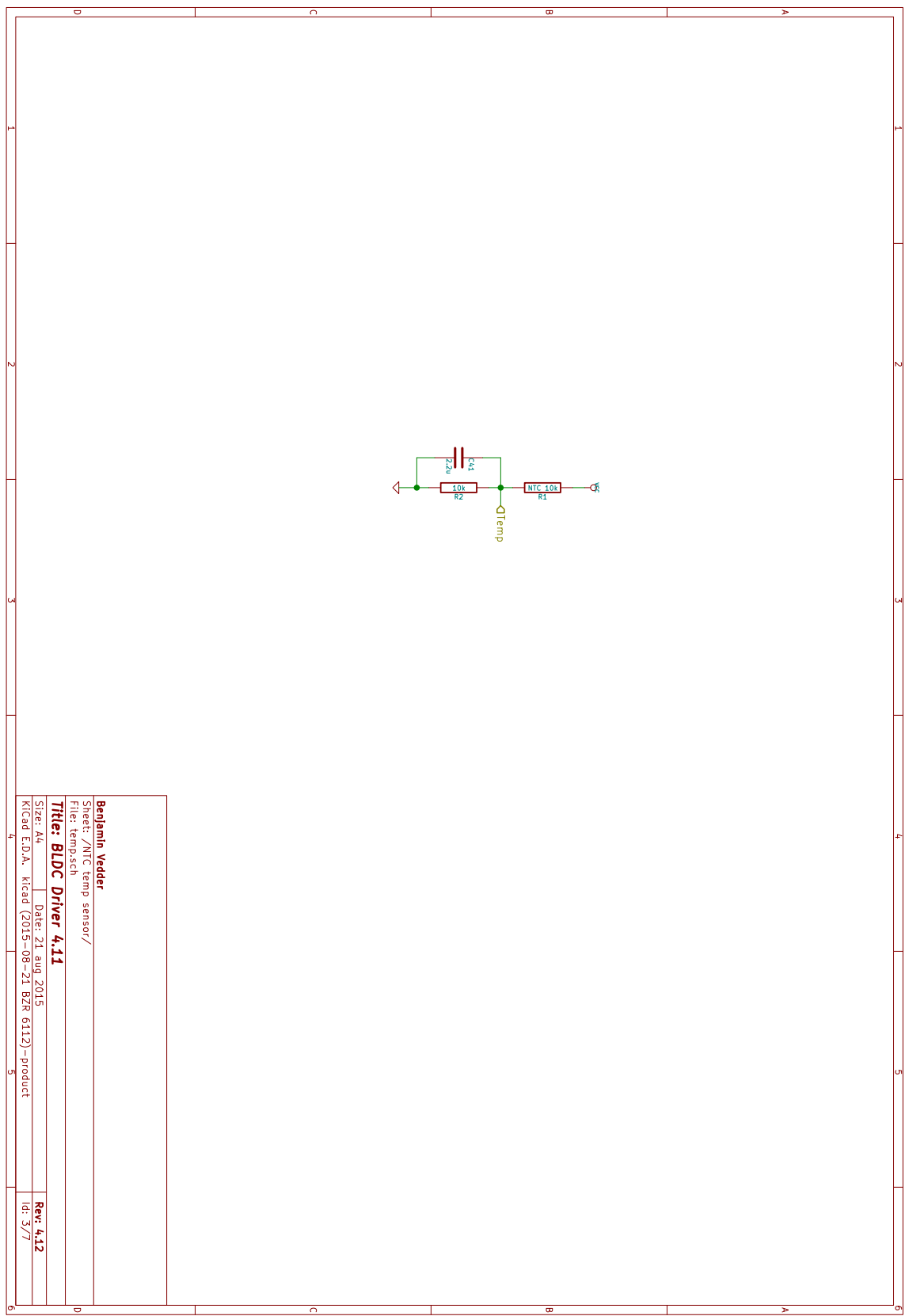


Figure A.3: In-Board Temperature Sensor

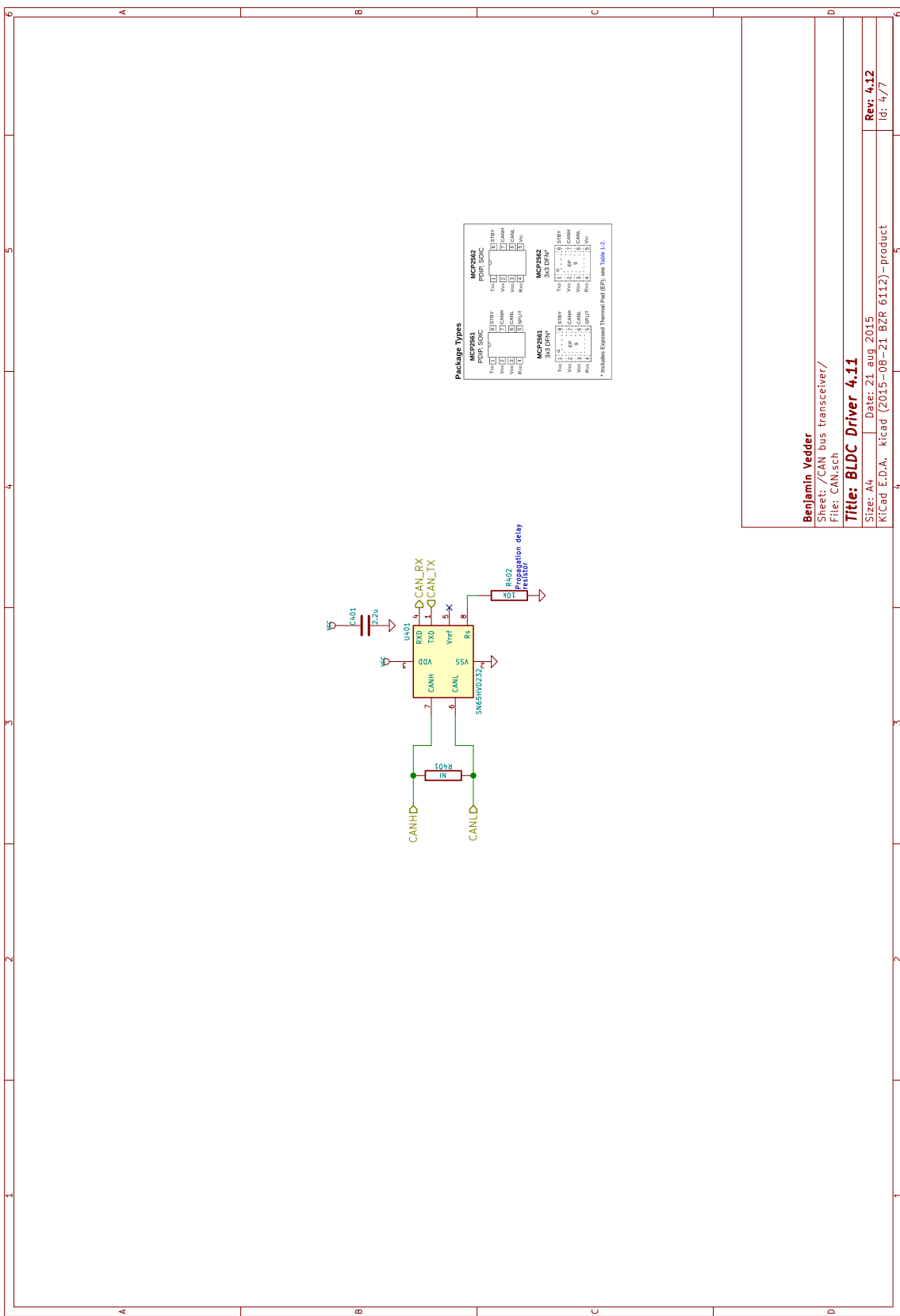


Figure A.4: CAN Bus Transceiver

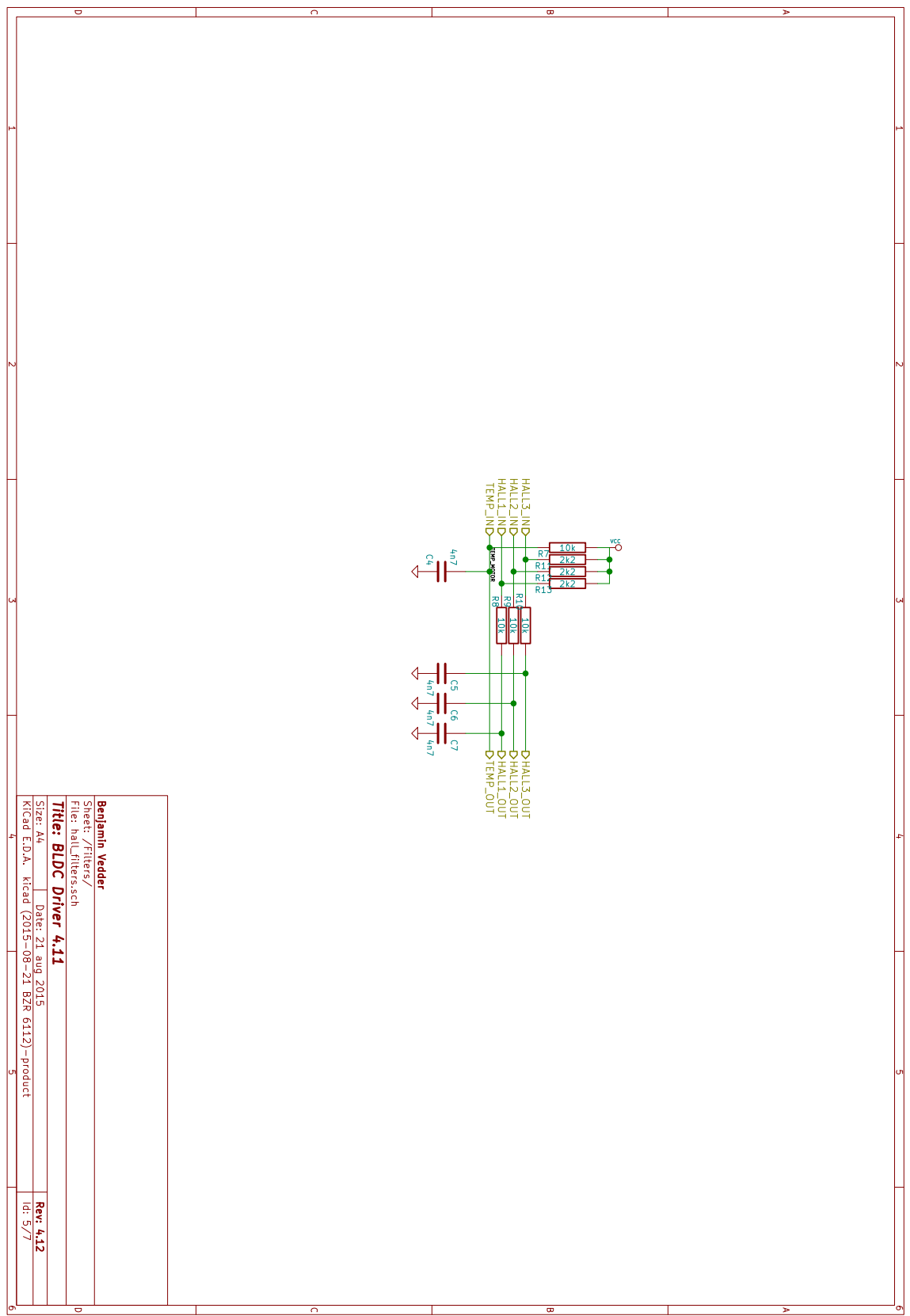


Figure A.5: Hall Effect Sensors Signal Conditioning

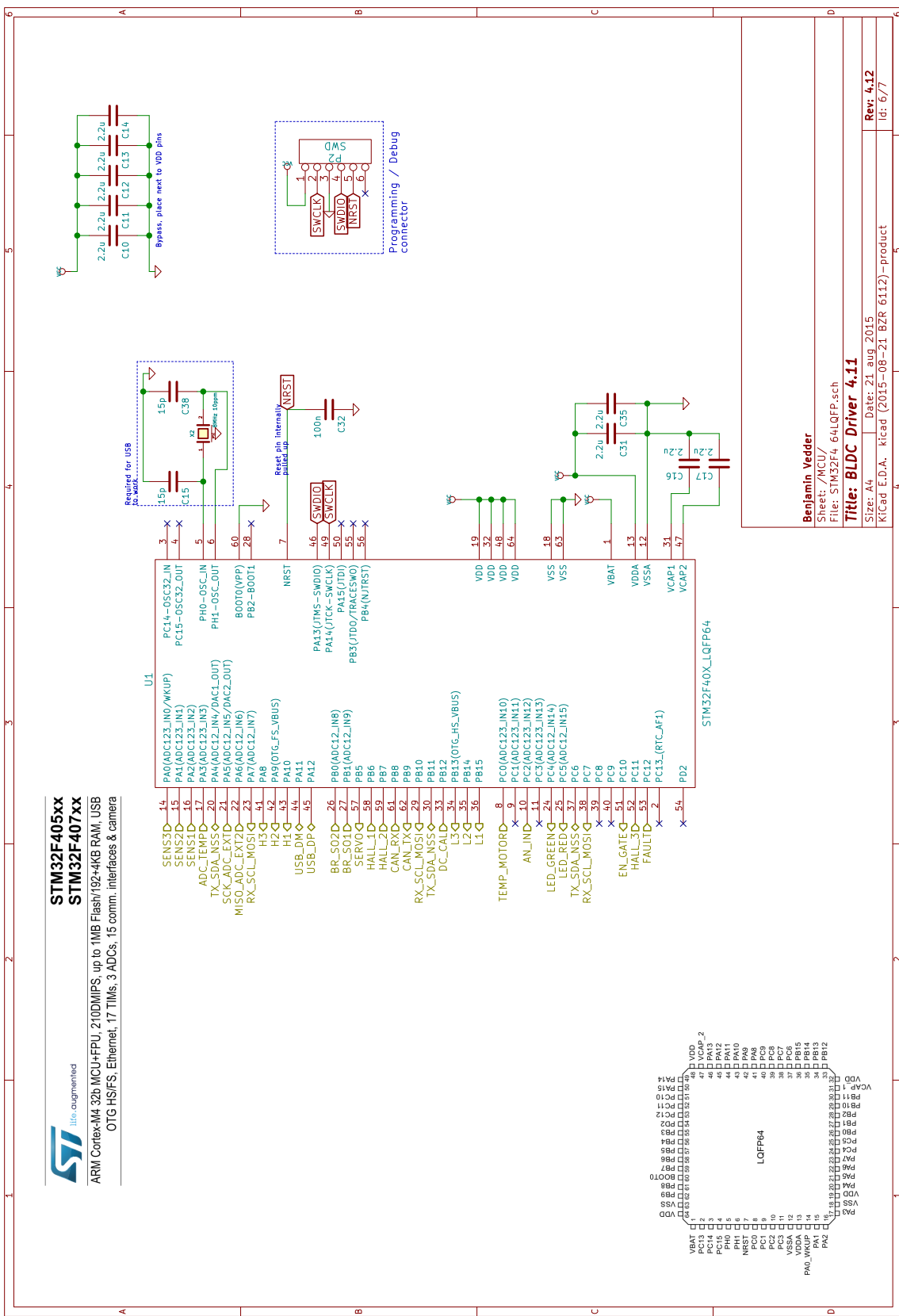


Figure A.6: STM32F405 Hardware Setup

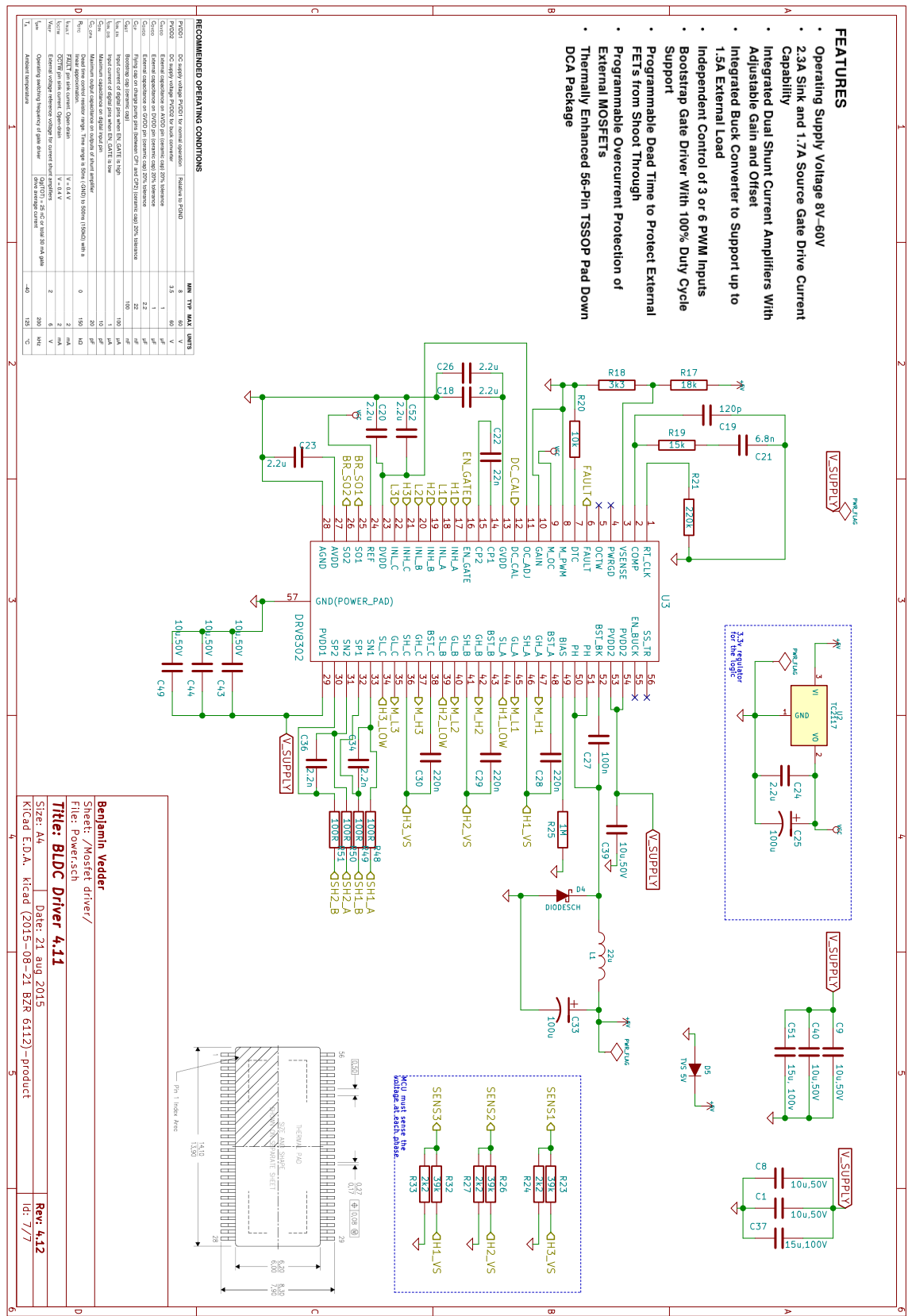


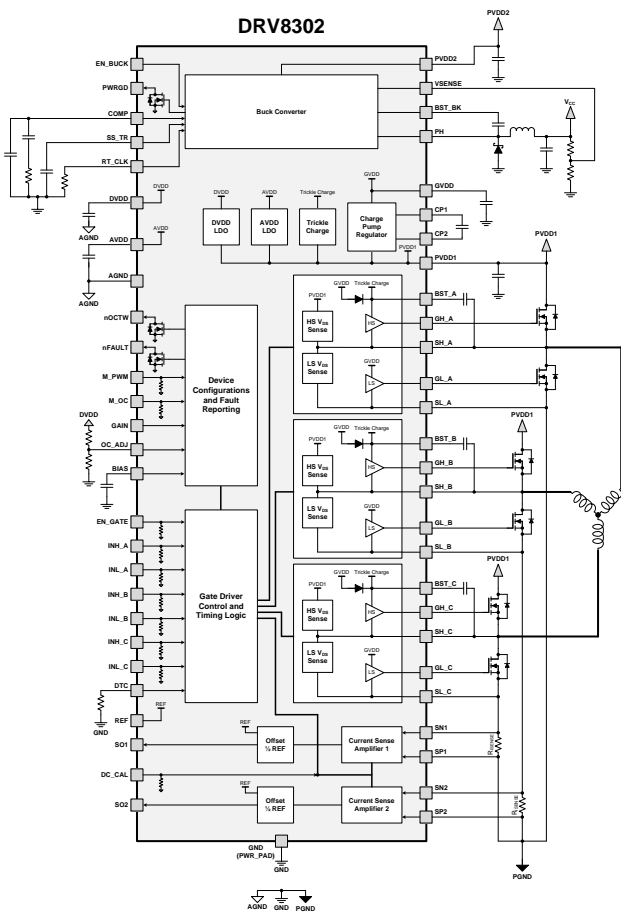
Figure A.7: DRV8302 MOSFET Driver

B

APPENDIX B: DRV8302 FUNCTION BLOCK DIAGRAM

DRV8302
SLES267C – AUGUST 2011–REVISED MARCH 2016
www.ti.com

7.2 Function Block Diagram



12 [Submit Documentation Feedback](#) Copyright © 2011–2016, Texas Instruments Incorporated
Product Folder Links: [DRV8302](#)

Figure B.1: DRV8302 Function Block Diagram

C

APPENDIX C: MOTOR SIGNALS MEASUREMENT BOARD SCHEMATICS

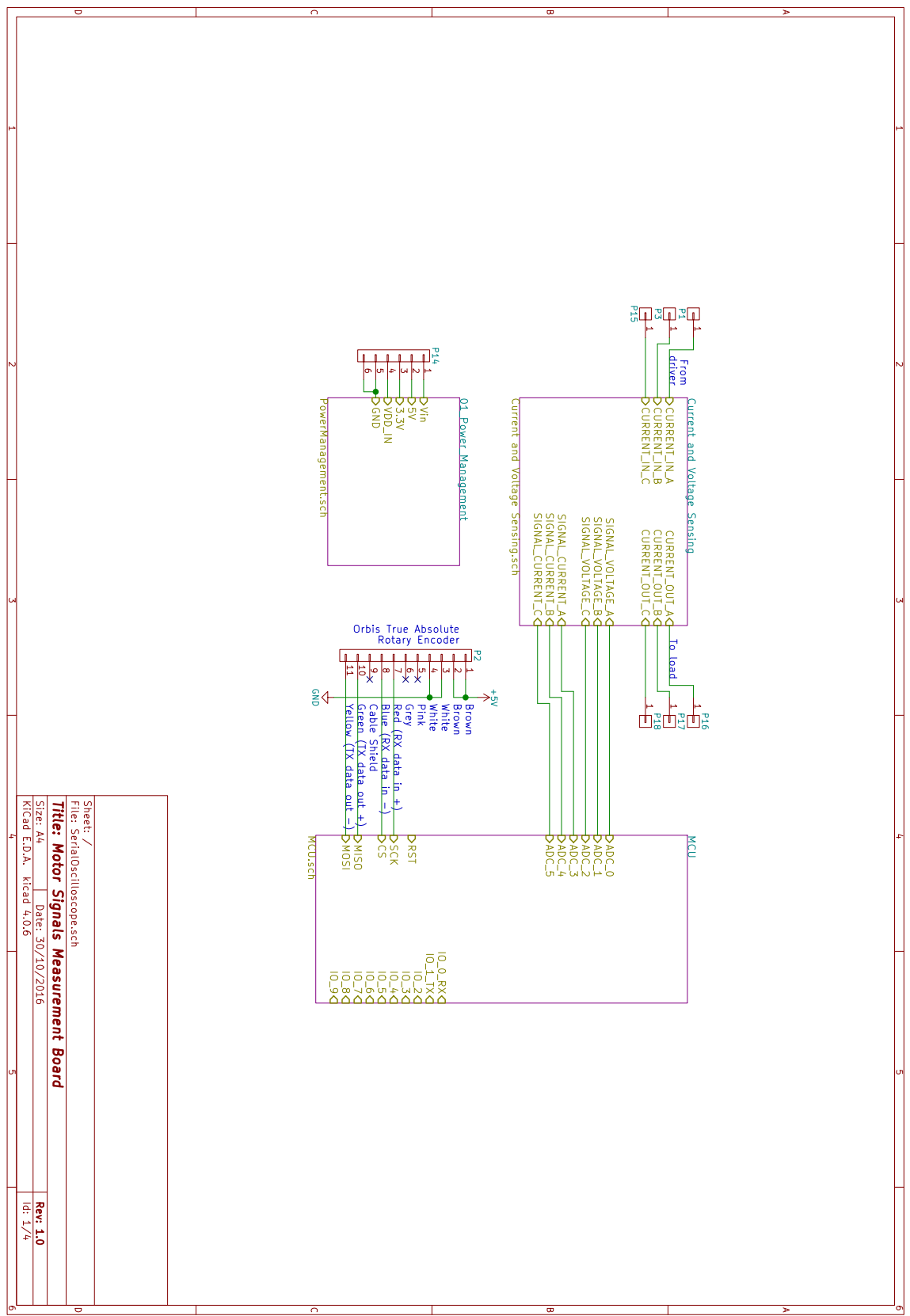


Figure C.1: Schematic Overview

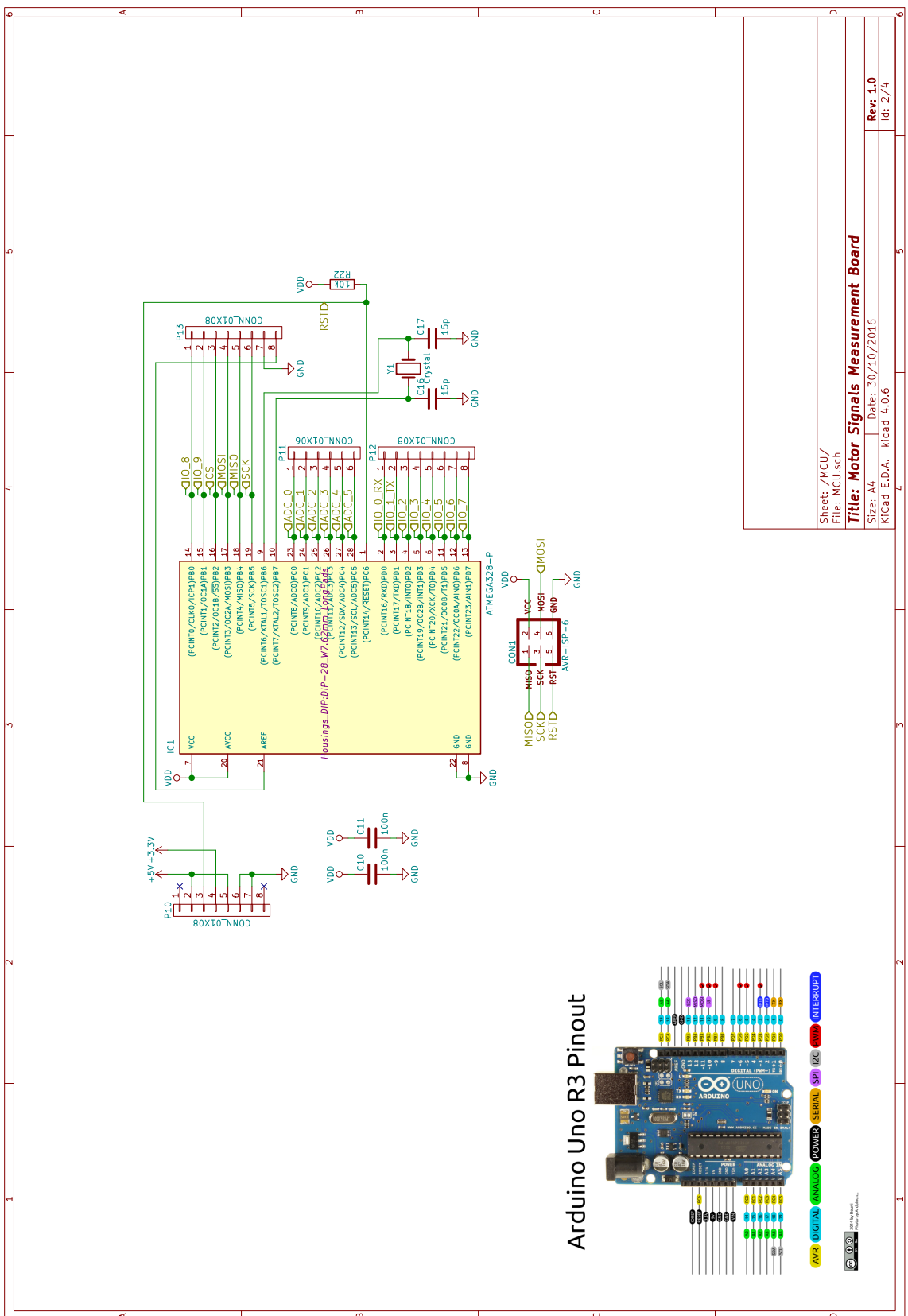


Figure C.2: Embedded system attachment pinout

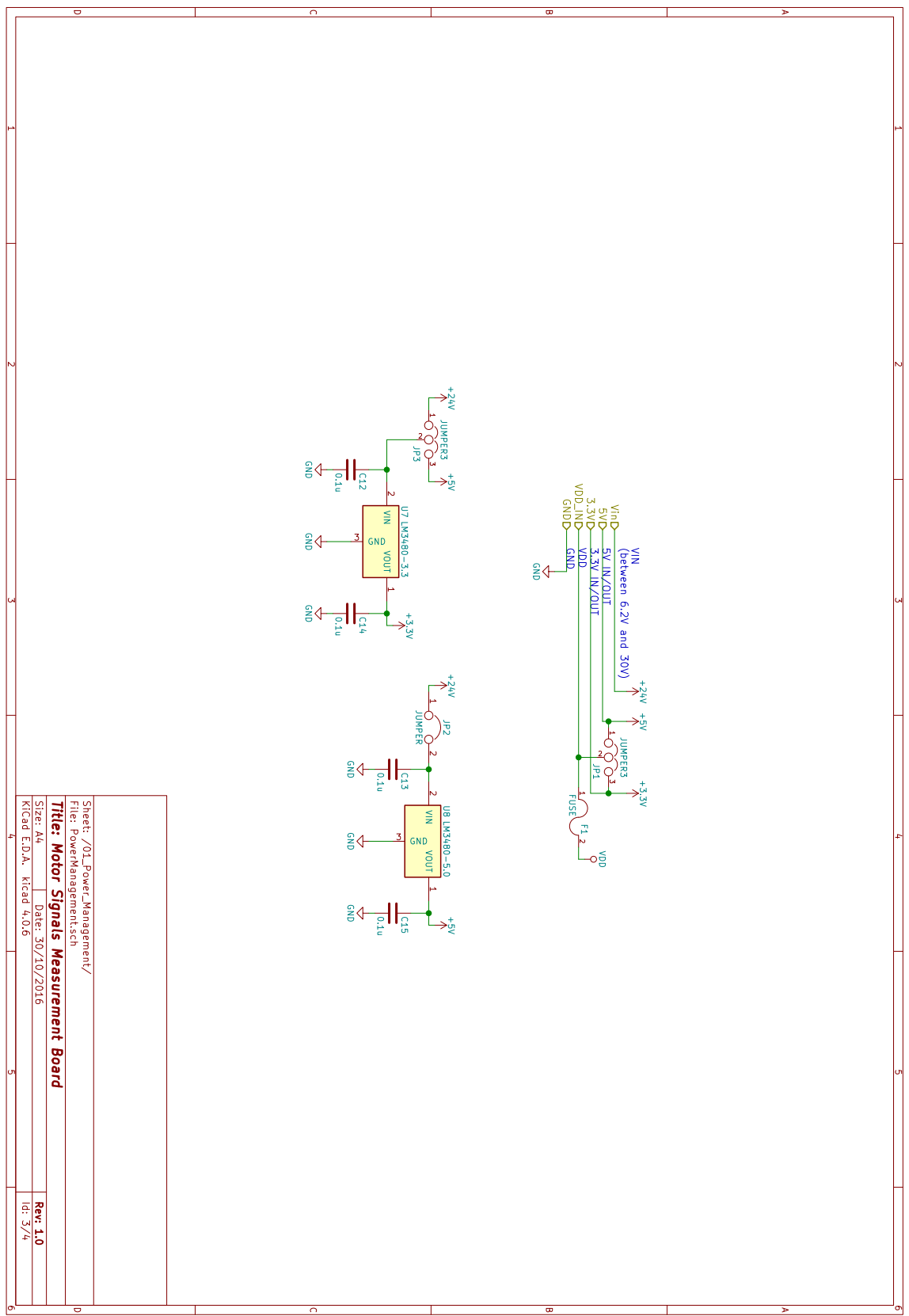


Figure C.3: Power management of the board

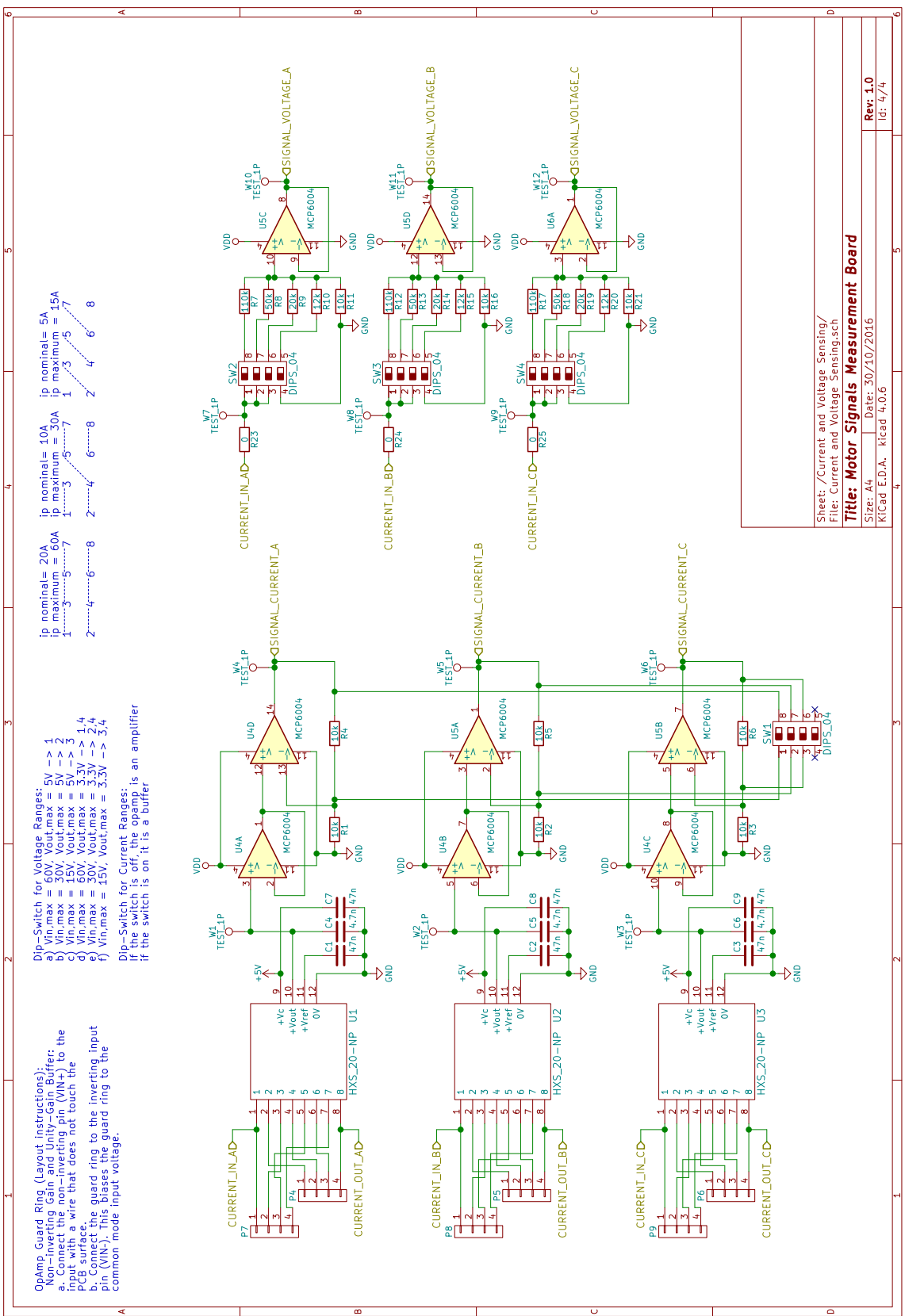


Figure C.4: Voltage and current signal conditioning circuits